Cátia Andreia Vieira Rocha

(Para)magnetic solid lipid nanocarriers for early detection and treatment of solid tumours

October 2019

Universidade do Minho
Escola de Ciências

Cátia Andreia Vieira Rocha

(Para)magnetic solid lipid nanocarriers for early detection and treatment of solid

Master Thesis
Master in Biophysics and Bionanosystems

Work developed under the supervision of
Doctor Juan Gallo Páramo
and
Professor Doctor Paulo José Gomes Coutinho

October 2019

ACKNOWLEDGEMENTS

During the development of this thesis all the challenges and objectives would not have been overcome without the unconditional support of everyone involved.

I'd like to express my utmost appreciation to my main supervisor, Dr. Juan Gallo Páramo, for its patient guidance, support, availability and constructive suggestions throughout the whole process of developing this dissertation. I'd like to express my gratitude to Dr. Manuel Bañobre for his warm welcome into the AmTheNa group, his confidence, patience and willingness to teach me more in every step of the way. I'd like to thank Dr. Paulo Coutinho for his teachings and his guidance along the journey that led me to finish this thesis.

I express my profound gratitude to my parents, because without them none of my academic accomplishments would be possible. For all their support, patience, confidence and continuous motivation throughout the six years of studies that led me here. I'd like to thank my brother Fábio for always helping me to relax and take my mind off stress.

I'd like to express my gratitude to my boyfriend, Tadeu, for always being there for me, proportionating fun moments, listening, calming me and helping me throughout every step of this journey. I'd also like to thank my high school friends and my cousin for always being present and supporting me.

I have to thank my master colleagues and most recent friends for their help, animated talks and friendship. I also show my appreciation to my dear friends from my bachelor, for comforting me even at long distances. I'd like to express my gratitude to Dr. Milene, Dr. Lorena, Dr, Stefania, Dr. Marta, Nuria and all the AmTheNa members for the sharing of ideas, good conversations and always being available to help me whenever I had difficulties.

I'd also like to acknowledge everyone that was involved throughout this whole process, including the institution that accepted me, namely the group of Nanomedicine of INL, that provided all the possible resources needed to conclude this dissertation.

STATEMENT OF INTEGRITY

I hereby declare having conducted this academic work with integrity. I confirm that I have not used plagiarism or any form of undue use of information or falsification of results along the process leading to its elaboration.

I further declare that I have fully acknowledged the Code of Ethical Conduct of the University of Minho.

Título: Nanopartículas (para)magnéticas para deteção precoce e tratamento de tumores sólidos.

RESUMO

Estratégias promissoras de entrega fármacos são cada vez mais relevantes para o tratamento de uma ampla variedade de doenças, como tumores sólidos. A entrega de fármacos é vista como uma solução inovadora para superar desafios atuais na medicina, como encontrar o equilíbrio perfeito entre ganho terapêutico e efeitos adversos induzidos pela terapia. Nanocompósitos híbridos (orgânicos/inorgânicos) têm vindo a ser explorados, de modo a combinar sinergicamente diagnóstico e terapia em formulações clinicamente eficazes. Neste trabalho foi desenvolvido um veículo de entrega de fármacos externamente controlado, com atividade anti-tumoral aprimorada.

Nanotransportadores lipídicos sólidos biocompatíveis combinados com nanopartículas magnéticas, responsivas ou não responsivas, e doxorrubicina foram sintetizados e caracterizados físico-química e funcionalmente. A eficiência de encapsulação da doxorrubicina foi de quase 100 %. As nanopartículas obtidas são esféricas e seu tamanho varia entre 150 e 200 nm, sendo ideal para administração. O nanocompósito apresentou um comportamento misto, superparamagnético e paramagnético, ideal para obter contraste duplo no diagnóstico por ressonância magnética. A inclusão de magnetita no veículo de entrega faz com que este seja adequado para tratamentos termorregulados, devido ao seu grande potencial de aquecimento quando exposto a um campo magnético alternado. Portanto, a libertação de doxorrubicina foi maior quando a formulação foi exposta a hipertermia magnética. Os efeitos das nanopartículas lipídicas em células de cancro da mama triplo negativo (Hs578T) foram avaliados *in vitro*. Ensaios de toxicidade confirmaram a biocompatibilidade do veículo e das nanopartículas magnéticas encapsuladas, para concentrações clinicamente relevantes de iões de ferro e manganês. Células tratadas com nanotransportadores lipídicos sólidos e expostas a hipertermia (quimioterapia/hipertermia), mostraram um maior efeito anti-tumoral, confirmando o potencial das partículas comparado a tratamentos tradicionais.

Os sistemas de entrega desenvolvidos representam avanços no teranóstico personalizado. Os resultados obtidos são promissores para o uso destes nanocompósitos no diagnóstico precoce, monitorização de doenças e tratamento sinergético de tumores sólidos, atingindo os objetivos de toxicidade sistémica reduzida, agente de contraste duplo, eficácia anti-tumoral aprimorada e efeitos adversos diminuídos na terapia do cancro.

Palavras-chave: Hipertermia magnética, Nanopartículas magnéticas, Nanotransportadores lipídicos sólidos, Ressonância magnética, Teranóstico.

Title: (Para)magnetic nanoparticles for early detection and treatment of solid tumours.

ABSTRACT

Nowadays, promising nano drug delivery strategies are becoming increasingly relevant to treat a wide range of diseases, such as solid malignant tumours. Drug delivery is sought as an innovative solution to overcome medical difficulties, as finding the perfect equilibrium between therapeutic gain and therapy induced adverse effects. Hybrid organic/inorganic nanocomposites are being explored to synergistically combine diagnostic and therapeutic capabilities into clinically effective formulations. Herein, an externally controlled theranostic drug delivery vehicle with enhanced anti-tumoral activity is developed.

Biocompatible solid lipid nanocarriers combined with responsive or non-responsive magnetic nanoparticles and doxorubicin were synthetised and physico-chemically and functionally characterised. The nanoparticles are spherical, and their size ranged from 150 to 200 nm, ideal for administration. Doxorubicin presented an encapsulation efficiency of almost 100 %. The nanocomposite showed mixed superparamagnetic and paramagnetic behaviour, ideal to achieve a dual contrast in magnetic resonance imaging diagnosis. Moreover, the inclusion of magnetite into the delivery vehicle makes it suitable for thermo-regulated treatments, due to its great heating potential when exposed to an alternating magnetic field. Thus, doxorubicin release was more pronounced when exposed to hyperthermia treatment. An *in vitro* evaluation of the lipid nanoparticles effects was performed in triple negative breast cancer cells (Hs578T). Toxicity assays confirmed the biocompatibility of the vehicle and the encapsulated magnetic nanoparticles at clinically relevant concentrations of iron and manganese ions. By combining solid lipid nanocarriers loaded with doxorubicin and magnetic field exposure (chemotherapy/hyperthermia) *in vitro*, a better anti-tumoral effect was achieved demonstrating the potential of these particles to enhance the effect of traditional treatments.

The designed delivery systems represent a step forward towards the final goal of personalised theranostics. The results attained are promising for the use of the presented nanocomposites in early diagnosis, disease monitoring and synergetic treatment of solid tumours. This may realize long sought after goals of reduced systemic toxicity, dual contrast agent efficiency, enhanced anti-tumoral efficacy and diminished adverse effects in cancer therapy.

Keywords: Magnetic hyperthermia, Magnetic nanoparticles, Magnetic resonance imaging, Solid lipid nanocarriers, Theranostic.

MOTIVATION

The global cancer burden is estimated to have risen to 18.1 million new cases and 9,6 million deaths in 2018. In this same year, more than 58000 people were diagnosed with cancer in Portugal, being that half of those cases have led to death [1]. The vast majority of these cancers appear as solid tumours. Current treatment protocols (surgery, chemo-, radio- and immuno-therapy) have proved their utility in the clinic, but they are still far from being the solution to this problem. In this project an innovative tool against solid tumours through a combination of early diagnosis and treatment (theranosis) will be developed.

The International Iberian Nanotechnology Laboratory (INL) has recently developed a multifunctional nanocomposite including magnetic nanoparticles dispersed in a lipid matrix [2]. Both the magnetic and lipid components of this system combine their properties in a synergic manner to provide a powerful weapon in the fight against cancer. The lipid part of the system can be used to encapsulate chemotherapeutic agents. This encapsulation has a double effect on the outcome of the treatment, on one hand increases the local concentration of the drug in the cells, and on the other protects healthy tissues from the deleterious effect of the drug, reducing then side effects. The magnetic part brings also interesting capabilities to the system. Magnetic nanoparticles (MNPs) have been used in the clinic since the late 1990's as magnetic resonance imaging (MRI) contrast agents (CAs) and thus can be used for the non-invasive detection of tumours [3]. MNPs can as well be used to generate heat under alternating magnetic fields in a process called magnetic hyperthermia (MHT). This heat can be used for the direct ablation of tumours through hyperthermia, and/or as a stimulus for the controlled delivery of drugs [4]. Paramagnetic nanostructures have also been developed at INL and can be used as MRI CAs and at the same time as O_2 generators to remediate tumour hypoxia and improve current treatments [5], [6].

Overall, this study will consist in the creation of a new nanocomposite, followed by its physico-chemical and functional characterisation, focusing on its performance as a MRI contrast agent, magnetic hyperthermia effector and controlled drug delivery system. This can be an important tool in nanomedicine to help in the fight against cancer.

TABLE OF CONTENTS

LIST OF FIGURES

LIST OF TABLES

LIST OF ABBREVIATIONS AND ACRONYMS

2D – Two dimensional;

3D – Tri dimensional;

ADF – Annular dark-field;

AMF - Alternating magnetic field;

ATR - Attenuated total reflectance;

BBB – Blood Brain Barrier;

BF – Bright field;

BOLD – Blood oxygen level dependency;

BSE - Back-scattered electrons;

CA – Contrast agent;

CCD- Charge couple device;

DAPI - 4',6'-diamino-2-fenil-indol;

DDS – Drug delivery system;

DHA – Docosahexaenoic acid;

DiO - 3,3'-Dioctadecyloxacarbocyanine Perchlorate;

DLS – Dynamic light scattering;

DMEM - Dulbecco's modified Eagle's medium;

DMEM – Dulbecco's modified eagle's medium;

DNA - Deoxyribonucleic acid;

dox – Doxorubicin;

DSC - Differential scanning calorimetry;

EDX - Energy dispersive X-ray spectroscopy;

EE – Encapsulation efficiency;

ELS - Electrophoretic Light Scattering;

EMA - European Medicines Agency;

EPR – Enhanced permeability and retention;

FBS - Fetal bovine serum;

FC – Field cooling;

FDA – Food and Drug Administration;

FIR - Far infrared;

fMRI – Functional magnetic resonance imaging;

FOV- Field of view;

FT-IR – Fourier Transform Infrared spectroscopy;

Glc – glucose;

H_c – Coercivity;

HPLC - High performance liquid chromatography;

Hs578T - Triple negative breast carcinoma cell line;

ICP- AES – Inductively coupled plasma - atomic emission spectroscopy;

INL - International Iberian Nanotechnology Laboratory;

IR – Infrared or Inversion recovery;

LDL - Low-density lipoprotein;

LED – light-emitting diode;

logD - Distribution coefficient;

logP - Partition coefficient;

M – Magnetization;

MCT - Mercury-Cadmium-Telluride;

MDR – Multi-drug resistance;

MEMS - multi-echo multi-slice;

MHT – Magnetic hyperthermia;

MIR - middle infrared;

MNP - Magnetic nanoparticle;

MPRAGE - Magnetization prepared rapid gradient echo;

M_r – Remanent magnetization;

MRI – Magnetic resonance imaging;

M_s– Saturation magnetization;

mSLNs - magnetic solid lipid nanocarriers;

NA – Numerical aperture;

NC – Nanocarrier;

NLC – Nanostructured Lipid Carrier;

NMR - Nuclear magnetic resonance;

NP - Nanoparticle;

OA – Oleic acid;

PBS - Phospate-buffered saline;

PD – Proton density;

PEG - Poly(ethylene) glycol;

PI - Polydispersity Index;

QD – Quantum Dot;

R_1 - Longitudinal relaxation rate;

r_1 - Longitudinal relaxivity;

R_2 - Transverse relaxation rate;

r_2 - Transverse relaxivity;

RF - Radiofrequency;

ROS – Reactive Oxygen Species;

rpm – rotations per minute;

SAR – Specific absorption rate;

SE – Spin echo;

SEM – Scanning electron microscopy or Standard error of the mean;

SLN – Solid Lipid Nanocarrier;

SPION - Superparamagnetic iron oxide nanoparticle;

SQUID - Superconducting quantum interference device;

STEM - Scanning transmission electron microscopy;

T_1 - Longitudinal relaxation time;

T_2 - Transverse relaxation time;

T_B – Blocking temperature;

TE – Echo time;

TEM –Transmission electron microscopy;

TGA – Thermogravimetric analysis;

TI – Inversion time;

TR – Repetition time;

UV-Vis – Ultraviolet visible;

VEGF - Vascular endothelial growth factor;

VSM - Vibrating-sample magnetometer or vibrating sample measurement;

WHO - World Health Organization;

XRD – X-ray diffraction;

ZFC – Zero field cooling;

ζ- potential - Zeta potential

CHAPTER 1 - INTRODUCTION

1.1. The issue of cancer

1.1.1. Etiology and incidence

Cancer is a disease that is part of our current reality and has been a challenge to researchers and medical teams to find new strategies to overcome it. This is a problem with no prospects of having a long-term resolution, being therefore a disease of the present and the future. This disease is characterised by a rapid and uncontrolled division of abnormal cells, which can grow beyond their usual boundaries and spread to other parts of the body (metastasis) [7].

Cancer is caused by genetic changes, and in some cases they may be hereditary. There are several other etiologic factors that may lead to cancer, such as age, smoking, alcohol, diet, exposure to chemical agents and radiation, hormones and infections by viruses and bacteria [8]. Hence, the prevention of this disease can be possible to a certain extent through changes in diet and lifestyle, regular screening, chemoprevention and risk-reducing surgery [9].

Cancer is the second leading cause of death worldwide and its incidence has been increasing annually, along with the average age of the affected population. In 2018, there were an estimated 18.1 million new cases of cancer in the world [1]. Figure 1 shows the estimated age-standardized incidence rates worldwide, for all cancers in both sexes in 2018 [10].

ASR (World) per 100 000

≥ 253.9
183.8–253.9
138.3–183.8
106.5–138.3
< 106.5

Not applicable
No data

Data source: GLOBOCAN 2018
Graph production: IARC
(http://gco.iarc.fr/today)
World Health Organization

World Health Organization
© International Agency for
Research on Cancer 2018
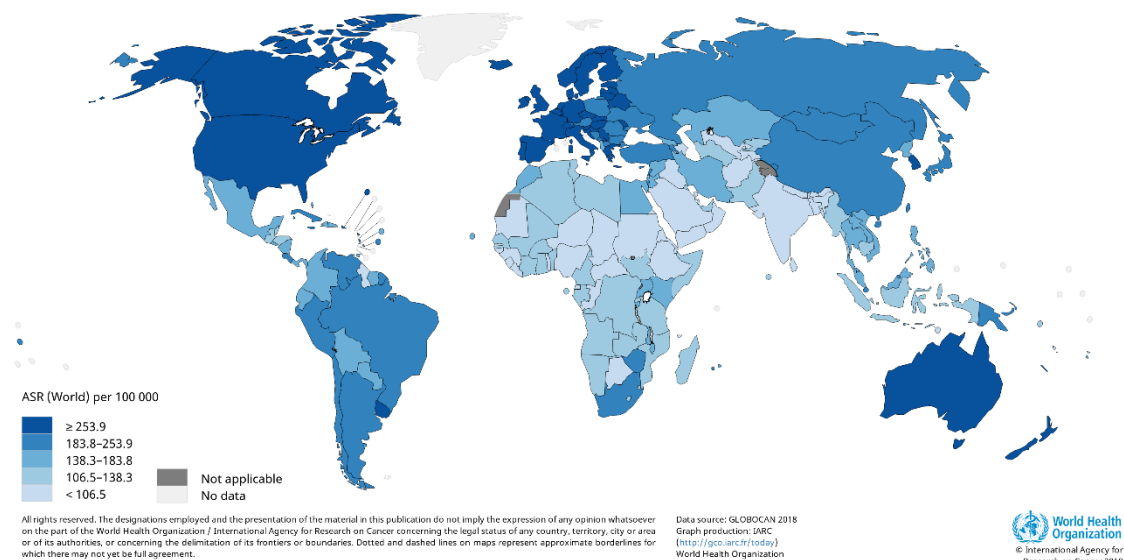
Figure 1- Global age-standardized incidence of all cancers in both sexes in 2018 [10].

In 2018, the World Health Organization (WHO) reported 9,6 million deaths due to cancer. In this same year, more than 58000 people were diagnosed with cancer in Portugal, being that half of those

cases have led to death [1]. The vast majority of these cancers appear as solid tumours such as lung, breast, prostate and colorectal tumours [11]. With the introduction of screening and the increased flow of information on cancer, it was possible to observe a gradual decrease in early and standardized mortality rates in Portugal. However, we continue to see an increase in the gross mortality rate, especially in males [12].

1.1.2. Tumour biology

Cancer is a process with several steps, by which cells go through metabolic and structural changes. These alterations have a great impact on the mechanisms that control cell proliferation, as the same time as they increase the resistance of cancer cells to the host's immune system. The changes occur at the DNA (deoxyribonucleic acid) level, which contains the genetic information responsible for the synthesis of proteins. DNA molecules are modified at the level of their nucleotidic sequence (mutations) and at their chromatin structural organization. Modifications in the nucleotidic sequence lead to a defective gene reading by transcriptional mechanisms, resulting in the synthesis of proteins in disproportionate amounts or with a wrong amino acid structure. Alterations in the chromatin conformation result in difficulties in the process of DNA packaging in the nucleus, leading to malfunctions in DNA transcription, translation, replication and repair mechanisms [13].

The process of carcinogenesis can be defined in at least 3 steps: initiation, promotion and progression (figure 2) [14]. In the initiation phase the mutagenic agent, endogenous or exogenous, will interact with the DNA and induce physical, chemical or biological changes in the genes. These changes result in a deregulation of cell signalling mechanisms and in their survival and differentiation. At the end of this phase the cancer is not yet clinically detectable and may be reversible. However, lesions caused in proto-oncogenes and tumour suppressor genes will contribute to the development and evolution of the disease. During the promotion, mutations in tumour suppressor genes, which control replication through self-destruction programs such as RB1 (retinoblastoma gene) and TP53 (produces p53 protein, responsible for cell cycle blockade, DNA repair and apoptosis), will lead to its inactivation and consequently to a blockade of apoptosis and uncontrolled proliferation of pre-neoplastic cells. Progression is the last stage of neoplastic transformation, characterised by genetic and phenotypic changes and accelerated tumour growth [15]. The presence of a solid tumour induces an angiogenic response by the organism's blood vessels. Angiogenesis is, in part, responsible for the transition from a minimally invasive and poorly vascularized tumour to a highly aggressive and vascularized one. At this stage the clinical prognosis is not favourable, representing in most cases host death [16].
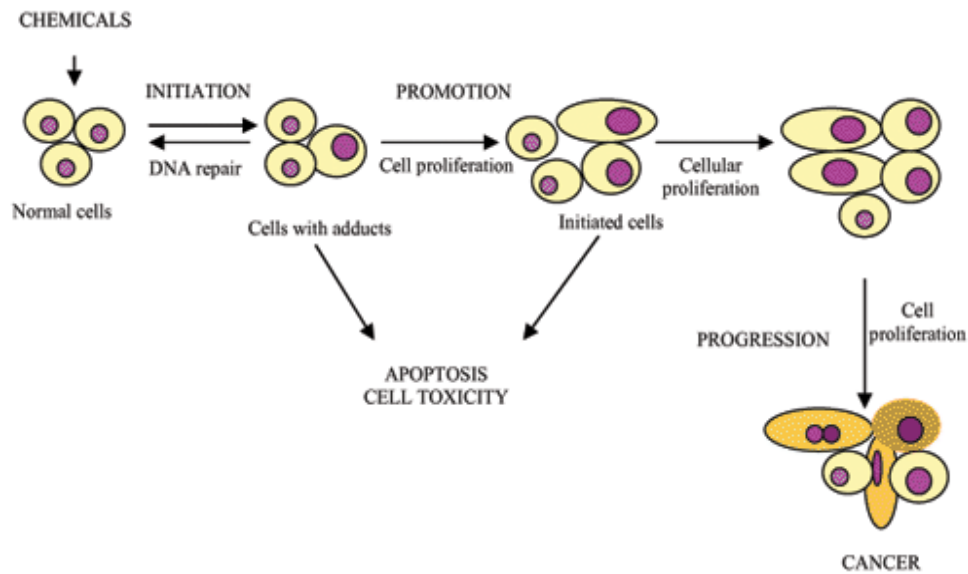
Figure 2 - Carcinogenesis phases (initiation, promotion and progression) and events involved in each phase [14].

1.1.3. Classic and emerging therapies

Nowadays, we are faced with several challenges in medicine, with cancer being one of the greatest and most problematic. Most classic therapies are proving to be insufficient, existing a growing need to develop new forms of treatment that are less invasive, more specific, and at the same time capable of eradicating the disease.

Cancer therapies can be used for curative or palliative purposes, since there are several types of cancer for which there is no available cure. The treatments can be systemic or localised, with the most common being chemotherapy, radiotherapy, surgery and immunotherapy [17]. These can be used alone or combined, however they are quite invasive and can be cytotoxic, which may lead to the appearance of side effects.

Chemotherapeutic drugs inhibit cell division, eventually leading to cellular death, especially in cancer cells. Nonetheless, a problem with chemotherapy is that it also damages healthy host cells, being particularly cytotoxic to the immune system, thus downregulating its response to the tumour [18]. Due to many chemotherapeutic agents being delivered to the tumour through the circulatory system, poorly vascularized tumours will be more inaccessible to the drug. The blood-brain barrier also represents an obstacle for chemotherapy, leading to drug delivery issues [19].

The principle of radiotherapy is to destroy cancer cells using ionizing radiation, while sparing the surrounding normal tissues. The efficiency of the treatment relies on the irreversible damage caused to the DNA directly, or indirectly through the formation of reactive oxygen species (ROS), which leads to cell death. However, despite all the technologic advances made in this field, the radiation can still affect

3

normal surrounding tissues, leading to adverse side effects [4]. Therefore, the importance of controlling the tumour at a cellular level arises.

In spite of all the advances made in classic cancer therapies, their efficacy seems to have reached a *plateau* for most solid tumours. However, new emerging therapies have a high probability of building onto the classical ones and reducing their flaws and limitations. These forefront ideas include examples such as genic therapy, photodynamic therapy, hyperthermia and targeted drug delivery. In this work we focus on the last two, particularly in magnetic hyperthermia (MHT) [4], [20]–[22]. On one hand, MHT is already being tested as a complementary treatment to radiotherapy, showing great results in clinical trials [23]–[26]. On the other hand, controlled drug delivery can increase significantly the accuracy and precision of the administration of chemotherapeutic drugs [27]. Moreover, both these techniques can be enhanced through nanotechnology, the first using MNPs (which can also be useful in diagnosis), the latter using organic and inorganic nanoparticles (NPs).

1.2.   Nanomedicine in cancer

The term nanotechnology was introduced in 1959 by the physicist Richard Feynman, in a talk entitled "There's Plenty of Room at the Bottom" and has since been a highly explored subject and in constant growth [28]. Nanotechnology is the manipulation of matter at an atomic and molecular scale, which allows the exploration of nanomaterials with diameters between 1 and 100 nm [29]. Materials at the nanoscale often exhibit completely different behaviours from the same materials in bulk form, in this size scale the quantum effects rule the behaviour and properties of the particles. While on bulk materials the physical properties are constant independently of their size, in the nanoworld the size of the NPs can dictate their chemical and physical properties like fluorescence, melting point, electrical conductivity, magnetic properties and chemical reactivity [30]. Therefore, the properties of the materials change as their size approaches the nanoscale and as the percentage of atoms on the surface of the material becomes significant.

Cancer nanotechnology, in particular, is evolving as a new interdisciplinary research to resolve cancer-related medical and pharmaceutical complications. Since the first proposal (1970s) of a targeted drug delivery system (DDS), the treatment and diagnosis of numerous diseases using nanotechnology has improved tremendously [31], [32]. The application of nanotechnology in medicine is an emerging field known as nanomedicine, and it can range from a biological application of nanomaterials to nanoelectronic biosensors (figure 3). Thus, nanomedicine can be defined as the use of nanostructured materials in medicine that according to their structure have unique medical effects [33]. Nowadays, a

significant number of companies is already pursuing nanomedicine activities, with the leading one being controlled drug delivery. Nanoscale DDSs for the treatment of cancers like breast, leukemia and Kaposi sarcoma, are already on the market and the number continues to grow [33], [34]. Despite recent advances in this field, the development of delivery systems with specific targeting abilities that can diminish the side effects caused by other therapies is still one of the challenges to nanomedicine. Hence, it's very important to continue to investigate different nanomaterials and their capabilities, with the focus on achieving effective DDSs.
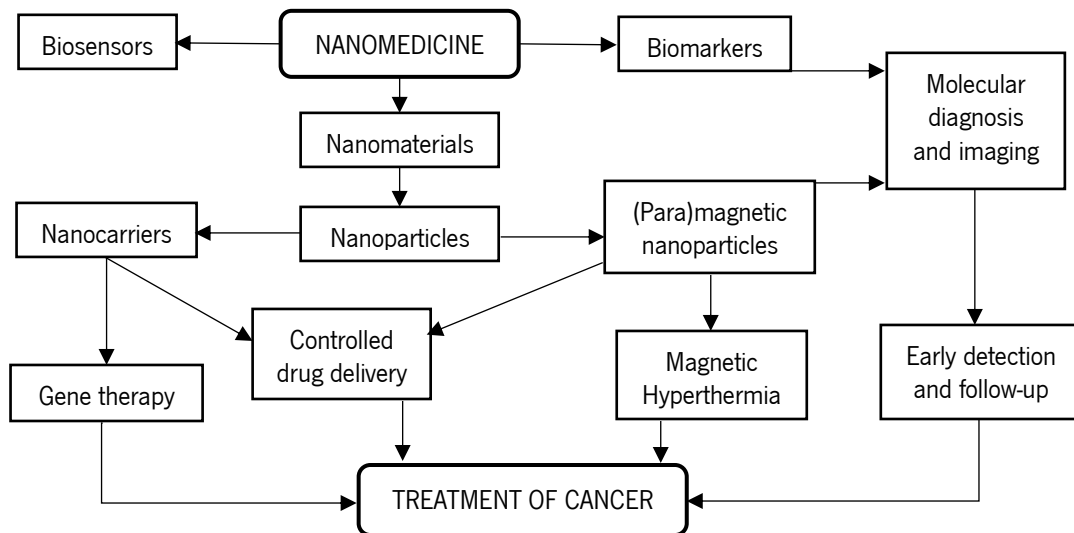
Figure 3 - The role of nanomedicine in cancer treatment.

Nanomaterials can be applied in many areas, but have a particular importance in nanomedicine, and they can be organic or inorganic. Lipid NPs, dendrimers, hydrogels and synthetic polymers are examples of organic nanomaterials. Examples of inorganic nanomaterials comprise mesoporous silica NPs, quantum dots (QDs), metallic, magnetic, paramagnetic and superparamagnetic iron oxide NPs (SPIONs), among others [27], [35]. Figure 4 illustrates a few examples of organic and inorganic NPs [35]. Certain nanomaterials allow efficient encapsulation and/or transport of drugs, proteins and nucleic acids, and can be conjugated with different ligands, such as peptides, antibodies or aptamers, increasing the binding affinity of the NPs to their targets [36].
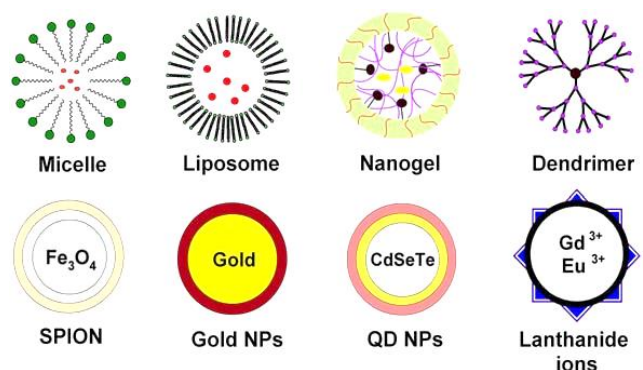
Figure 4 - Illustration of organic (top) and inorganic (bottom) NPs [35].

Nanoscale DDS using organic and inorganic NPs are emerging technologies in nanomedicine for cancer theranosis (therapy *plus* diagnosis). A better understanding of tumour biology and the increased availability of versatile materials (hydrogels, polymers, lipids), have led to the development of

bionanosystems that can transport nanoparticles and drugs to tumour sites. Drug encapsulation in these systems offers numerous advantages, such as: protection from degradation in the blood-stream; targeted drug delivery to increase the drug concentration at desired sites of action, reducing at the same time its toxicity in healthy tissues; controlled/modified drug release rate; increased drug solubility, to facilitate parenteral administration; improved drug stability; improved drug action; and better pharmacokinetic and pharmacodynamic properties [27], [37], [38].

One of the most interesting developments in this field is the potential of certain nanocarriers (NCs) to combat the increasing problem of multidrug resistance (MDR) acquired by cancers, reducing chemotherapeutic effects. A commercially available formulation of poly(ethylene) glycol (PEG) liposomal doxorubicin (Doxil®), showed anti-tumour activity in doxorubicin-resistant and non-doxorubicin-resistant colon cancer cells [39]. This comes as a motivation to further research on overcoming MDR. Using NCs loaded with pre-existing drugs offers effective treatment, without the need for the costly discovery of new chemotherapeutic drugs.

Overall, nanomedicine is a very promising field for cancer theranostics and allied to already existing products and treatments, it represents a cost-effective and efficient step forward in the fight against cancer.

1.3.　　　(Para)magnetic nanoparticles

Magnetic materials are materials that show a response to an applied magnetic field. There are three main sources of a magnetic moment: the electron spin, the angular moment of the orbital movement of electrons, and the alteration of this moment induced by an applied field (precession). According to a material response to a magnetic field, the magnetic materials can be classified in three main types: diamagnetic materials (e.g. Au, Ag and Cu); paramagnetic materials (e.g. Li, Al, Gd and Mn); and ferromagnetic materials (e.g. Fe, Co, Ni and their oxides) [40]. Diamagnetic materials have no unpaired electrons resulting in zero net magnetic moment, thus they display a very weak response against applied fields that only reveals when the total angular moment of the atoms is zero [40]. Paramagnetic materials have a net magnetic moment due to unpaired electrons, which align in the direction of an applied magnetic field forming a weak net magnetization, that is not retained after the field is removed [6], [40]. Ferromagnetic materials are formed by domains (Weiss domains) containing large numbers of atoms with their electronic spins parallelly aligned. These domains are separated by Bloch walls giving a more complex structure to ferromagnetic materials. This structure is maintained due to microscopic energy exchange interactions, anisotropy energy and magnetostatic energy [40]. The behaviour of ferromagnetic

materials can be represented by a hysteresis loop (figure 5). When these materials are submitted to an external magnetic field, the magnetic moments of the domains align in its direction and the domain walls disappear occurring a saturation magnetization (M_S) [40], [41]. When the field is removed, these materials keep a memory of the field, presenting remanent magnetization (M_r) that can be controlled by a coercive force that reduces this magnetization to zero to close the loop (coercivity, H_c) [41].
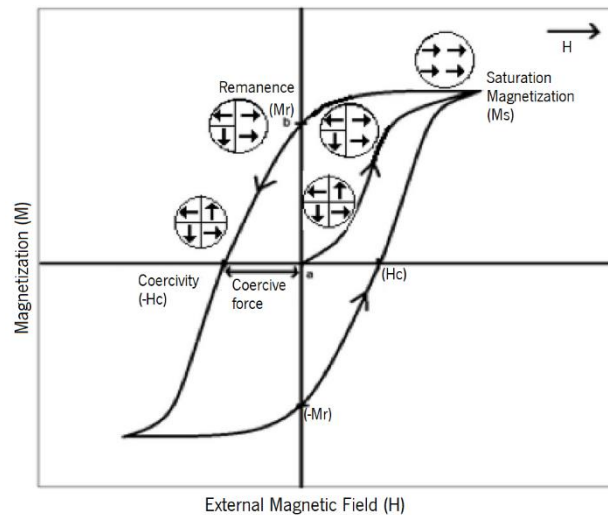
Figure 5 - General representation of a ferromagnetic material hysteresis loop, where the circles represent the behaviour of multi-domain particles induced by an external magnetic field. Adapted from [41].

During the past decades, nanotechnology has made possible to produce, characterise and tailor inorganic NPs for several biomedical applications. These have been intensively investigated for therapeutic and imaging capabilities, due to their numerous advantages, such as large surface area, improved bioavailability, lower toxic side effects, controlled drug release and their tolerance towards most organic solvents [27]. In this context NPs based on magnetic materials arise. Magnetic nanoparticles (MNPs) are those that respond to an applied magnetic field. MNPs, in the form of superparamagnetic iron oxide have been used in the clinic since the late 1990's as contrast agents (CAs) in magnetic resonance imaging (MRI) and thus can be used for the non-invasive detection of tumours [3]. MNPs can also be used to generate heat under alternating magnetic fields (AMF). This heat can be used for the direct ablation of tumours through hyperthermia, and/or for the controlled delivery of drugs [4]. Interestingly, some paramagnetic NPs are also of great interest due to their responsiveness to biologically relevant pH and redox states. They can too be used as MRI CAs and at the same time as O_2 generators to remediate tumour hypoxia and improve current treatments [5], [6].

1.3.1. Iron oxide nanoparticles

Iron constitutes one of the most important elements present in the human body, both through dietary intake and through its inherent role in a wide array of biochemical processes. One of its most crucial roles is its presence in Haemoglobin, the metalloprotein that makes up the structure and function of

erythrocytes, which is responsible for the transport of oxygen from the lungs to the various tissues [42]. Additionally, iron is also a core constituent of myoglobin, a protein that is responsible for aiding in oxygen diffusion in muscle tissue, increasing its efficiency. Moreover, the role of iron in electron transfer reactions should also be noted, since the successive oxidation and reduction of iron atoms present in cytochromes allows these reactions to take place [43]. Iron also plays an important role in DNA synthesis and repair, given that it works as a cofactor for many of the enzymes responsible for said processes such as helicases, glycosylases, demethylases and nucleases [44].

Given the utmost importance of iron in the normal functions of most cellular tissues, a deficiency in this element can lead to serious health problems, namely anaemia [45]. Anaemia occurs when lower than usual levels of iron in blood tissue, lead to a lower amount of haemoglobin and consequently ineffective transport of oxygen to tissues, what can lead to a higher chance of mortality and cognitive loss [43] . On the other hand, high levels of iron in the human body can lead to the formation of iron radicals which have an oxidizing effect, potentially becoming toxic by leading to cellular tissue damage [43]. Overall, although iron is safe for administration, attention need to be kept in order to avoid exposure to this element in high concentrations.

Iron oxide NPs have been widely explored for biomedical applications, with the most common ones being magnetite (Fe_3O_4) and maghemite (γ-Fe_3O_4) NPs [46]. In the most envisaged applications, the particles perform best below a critical diameter (d_c) (<15 nm) [47]. At this size it's not energetically favourable to maintain the Bloch walls, thereby the NPs become a single magnetic domain, presenting superparamagnetic behaviour when a magnetic field is applied and the temperature is above a blocking temperature (T_B), being called superparamagnetic iron oxide nanoparticles (SPIONs) [40], [48]. The blocking temperature refers to the temperature at which the thermal energy becomes smaller and the magnetic moments of the particles become blocked [49]. Above this temperature, monodomain particles display a fast response to changes in the magnetic field, exhibiting very strong magnetic properties. Hence, superparamagnetic particles present uniform magnetization (M) at any field, large magnetic susceptibility (χ), high saturation magnetization (M_S) values, no coercivity or hysteresis, and a rapid removal through extravasations and renal clearance [40], [41], [50]. In this kind of NPs, the phenomenon of ferromagnetism is no longer observed being that the particles rotate freely and present no remanent magnetization (M_r) in the absence of an external magnetic field, hence reducing the risk of agglomeration and guaranteeing colloidal stability [40], [48]. However, over long-time periods the particles can become unstable, and tend to form clusters to reduce the energy associated with high surface area to volume ratio. Therefore, surface functionalization is critical for specific biomedical applications, since it increases

biocompatibility and decreases the surface area to volume ratio, consequently reducing aggregation [47], [51].

Magnetite and maghemite are the main iron oxides that fall under the category of SPIONs [52]. Usually, these NPs consist of cores of iron oxides that can be targeted to the required area through external magnetic fields. They typically have two structural configurations: core-shell configuration, with an inner magnetic core, usually Fe_3O_4 or γ-Fe_3O_4, coated with a hydrophilic polymer, such as PEG; or a porous biocompatible polymer in which SPIONs are precipitated inside the pores. Figure 6 shows two possible configurations for iron oxide NPs [53],[54]. They can also be functionalized with ligands in order to increase the targeting yield, useful for therapeutic ends.
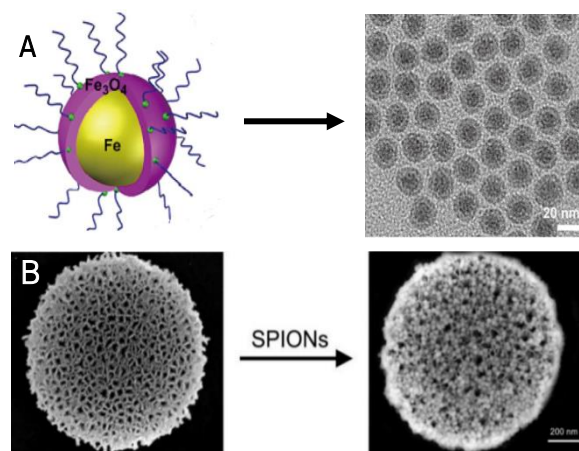
Figure 6- A: schematic illustration of a pegylated core/shell Fe@Fe$_3$O$_4$ NP (left) and transmission electron microscopy (TEM) images of pegylated Fe@Fe$_3$O$_4$ particles (right); B: scanning electron microscopy (SEM) images of discoidal porous silicon particles, unloaded (left) and loaded with SPIONs (right). Adapted from [53] and [54].

SPIONs are useful for theranosis purposes, since they can be incorporated into lipid DDS, like SLNs which are NPs with a solid lipid matrix stabilized by a surfactant, that can solubilize lipophilic molecules [27]. Due to their biocompatibility and non-toxic degradation into iron ions, SPIONs have already been approved for human use by the Food and Drug Administration (FDA) of the United States, European Medicines Agency (EMA) and other agencies (e.g. Feridex®, Resovist®). They have been extensively utilized preclinically in several biomedical applications, such as isolation and separation of cells, sample preparation, immunological assays, delivery of drugs and genetic material to cells and tissues, tissue engineering, hyperthermia and as CAs in MRI diagnosis [23], [55]–[58]. In this work the focus will be on the last two applications.

1.3.2. Manganese nanoparticles

Manganese is an essential trace element that is present in all diets in controlled quantities, where the adequate dietary intake of manganese for adults is 2-5 mg/day [59]. It is found in a variety of biological tissues and its required for normal protein, amino acid, lipid and carbohydrate metabolism, being also

essential for many enzyme families (transferases, lyases, isomerases...) [60]–[62]. Therefore, the presence of Mn in the body is crucial to maintain normal immune system functioning, bone growth, digestion, cellular homeostasis and other body functions [61], [63]. Manganese can also intervene in antioxidant activity and tumour defences, being possible that its levels are increased or decreased in cancer cells [64]. Nonetheless, its sequestration by mitochondria can interfere with proper respiration, leading to an overproduction of ROS [61].

The right amount of Mn is vital for the development of the body, being that a deregulation of its levels can be associated with diseased states. Mn deficiency can lead to reproductive and neurological problems, obesity and skeletal abnormalities. Since it is easily concentrated in the brain, Mn in excess can induce neurotoxicity, being able to cause dystonia and other abnormalities associated with Parkinson's disease [65]. Although Mn is a proven mutagen, it does not present significant carcinogenic activities [64]. Overall, this element is safe for administration, as long as the Mn homeostasis in the body is maintained through controlled intake and renal clearance [63].

Manganese NPs present a strong paramagnetic character that depends on the Mn ions oxidation state, hence, these particles do not retain any magnetization in the absence of an external magnetic field [6]. Nanoparticles made up of paramagnetic elements, such as manganese, are being investigated as T_1-MRI contrast enhancers, showing promising results. One of the most interesting stoichiometry for this element is the MnO, since it has a stable composition as the Mn ion presents a +2 valence state with 5 unpaired electrons, which results in higher effective magnetic moments [66]–[68]. The magnitude of the magnetic moment is of great importance in MRI, since the longitudinal relaxivity (r_1) is influenced by a spin-lattice interaction between the water molecules and the paramagnetic core. Therefore, the higher paramagnetic character of the particles, the more efficient the water protons relaxation time reduction and consequently the higher T_1 MRI contrast signal enhancement is observed [63].

Small molecule probes based on Mn have been developed to respond to changes in pH and redox state [5], [69], [70]. The interaction of the probe with species of interest *in vivo* will induce a chemical change in the probe, that translates into a difference in MR performance [5]. Manganese dioxide (MnO_2) NPs have earned the focus from scientific community due to their responsive behaviour [5]. MnO_2 NPs are very sensitive to environmental conditions, such as pH, which allows the detection of tumour acidic environment. Under the ideal conditions MnO_2 can be reduced to Mn^{2+} salts, which increases its paramagnetic character and consequently its MRI signal is greatly enhanced [5]. MnO_2 NPs are also capable to generate oxygen in the body, being this way able to fight tumour hypoxia and enhance the effect of other therapies [71]. Recent studies showed that the functionalization of manganese oxides NPs

with PEG and RGD peptides, allows the targeting of tumours overexpressing $\alpha_v\beta_3$ integrin, using T_1-weighted MRI [68].

As mentioned above, manganese NPs can be used in cancer treatment of solid tumours to enhance the effect of other therapies. MnO_2 NPs are capable to generate O_2 due to its high reactivity toward endogenous hydrogen peroxide (H_2O_2) and H^+ ions, both of which are abundant in tumours [71]. This reaction will raise the pH and help to overcome tumour hypoxia, thus enhancing the effect of other therapies like photodynamic therapy and radiation therapy [72], [73]. Recently, the use of MnO_2 NPs for sustained and localised generation of oxygen in solid tumours to modulate hypoxia and enhance radiation efficacy was studied. The injection of an albumin-MnO_2 complex followed by a single dose of 10 Gy irradiation, resulted in an enhanced tumour cell killing and growth delay compared to radiation alone [74].

1.3.3. Synthesis Methods

The physical and chemical properties of MNPs largely depend on the synthesis method and chemical structure. In the last decades, many publications have described effective synthetic routes to size/shape-controlled, highly stable and monodisperse MNPs. Biological, physical and chemical routes are the three main stated routes for the production of MNPs, with the chemical route being, by far, the most reported [52]. For the production of high quality MNPs for medical applications, several chemical methods can be utilized such as: microemulsions, sol-gel syntheses, electrospray syntheses, thermal decomposition of organometallic precursors, hydrothermal reactions, coprecipitation and sonochemical reactions [75]–[78]. In this project we'll use the last three techniques for the NPs synthesis.

Coprecipitation is a simple, economic and efficient way to synthesize iron oxides from aqueous Fe^{2+}/Fe^{3+} salt solutions (usually in a 2:1 molar ratio), by adding basic solutions under an inert atmosphere, either at room temperature or at elevated temperatures. The shape, size and composition of the MNPs produced by coprecipitation depend on the type of salts been used, the Fe^{2+}/Fe^{3+} ratio, temperature, ionic strength of the media and pH values [48], [79]. In particular the formation of magnetite occurs according to following chemical reaction:

$$Fe^{2+} + 2Fe^{3+} + 8OH^- \rightarrow Fe_3O_4 + 4H_2O$$
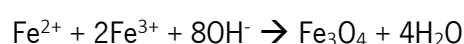
With this method a large amount of NPs can be synthesised and their quality is fully reproducible. However, particles like magnetite are not very stable and can be easily oxidized to maghemite or dissolved in an acidic medium. Since maghemite is another ferric particle of interest, this oxidation isn't much of a problem and sometimes can be deliberately induced, creating maghemite particles chemically stable in

alkaline and acidic medium [48], [80]. A drawback in coprecipitation synthesis is the fact that the control of particle size distribution is limited, producing NPs with a wide size distribution and therefore with a non-ideal magnetic behaviour for many applications. To achieve monodisperse iron oxide MNPs with the coprecipitation method, two key stages are involved: a short burst of nucleation, that happens when the concentration of species reaches critical supersaturation, and then, a subsequent slow growth of the nuclei occurs by diffusion of the solutes to the surface of the crystal. To obtain monodisperse MNPs it's crucial that these two stages are separated [48], [81]. Recently, the use of organic additives as stabilization agents, showed great results as a strategy to achieve more stable and monodisperse MNPs [82]. Thus, the selection of a proper surfactant is also an important issue for the stabilization of such particles [48]. Since coprecipitation processes require high-pH solutions, the by-products of this method may require further purification [79].

The hydrothermal method is another simple and widely used technique, that involves the production of NPs, usually iron oxides, by crystallization from an aqueous solution of ions at a high temperature under high vapor pressure [79]. The main processes performed with this method are hydrolysis and oxidation (where ferrous salts are used), or the neutralization of mixed metal hydroxides [80]. The reaction conditions, such as solvent, temperature and time have significant effects on the product. Thus, this technique allows a better control of the particles size, shape, composition and stoichiometry, producing MNPs with good monodispersity [79]. The size is mainly controlled through the rates of nucleation and grain growth, which are dependent on the reaction temperature. At higher temperatures, nucleation can be faster than grain growth, which results in a decrease in particle size. However, if the reaction time is extended, it will favour the grain growth and the particles obtained will be bigger. Surface capping agents, such as sodium oleate or PEG, can also be added during the reaction to stabilize the NPs and reduce the risk of agglomeration [48], [83].

The sonochemical method has been extensively used to synthetize MNPs with unusual magnetic properties. It involves the use of sonochemical techniques, such as a high-energy ultra-sonication, that creates cavitations, that is, the formation and growth of nuclei, and the implosive collapse of bubbles in liquid. The implosive collapse of the bubbles can provide localised heat with a temperature of about 5000 K [79]. This way we can obtain highly monodispersed oxide NPs from an aqueous solution of ions, with reduced agglomeration. However, sonochemical methods are not fit for large scale synthesis [52].

The methods mentioned above can complement each other, to easily produce MNPs with the desired physico-chemical properties.
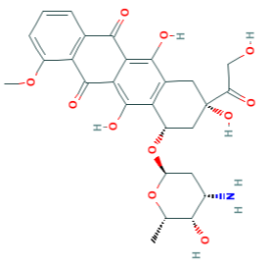
1.4.   Biomedical applications

1.4.1. Drug Delivery

Drug delivery is a process through which a pharmaceutical compound is incorporated into a vehicle and administered into the body to safely achieve its desired therapeutic effect, with diminished side effects. As mentioned before, the encapsulation of drugs in DDSs improves the bioavailability, pharmacokinetics (concentration versus time) and pharmacodynamics (effect versus concentration) of therapeutics, among numerous other advantages [33]. The requirements for drug delivery are known as ADMET profile, standing for absorption, distribution, metabolism, excretion and toxicity. This profile is determined by drug characteristics like lipophilicity, solubility, partition (logP) and distribution (logD) coefficients, molecular weight and median lethal dose, and it influences the performance and pharmacological activity of the encapsulated compound.

Doxorubicin (dox) was the drug chosen for this work due to its fluorescence properties, that allow the tracking of the drug in cells, and lipophilic character, that makes the encapsulation into the SLNs more efficient. Doxorubicin is a cytotoxic anthracycline antibiotic approved by the FDA, being already used to treat a wide variety of cancers. Some of the physico-chemical characteristics of this drug are shown in table 1 [84], [85]. In relation to its pharmacokinetics, dox is administrated intravenously since it is not absorbed by the gastrointestinal tract. It has a rapid and wide distribution (5-10 min) with a complete half-life of 12-18 h and a binding to plasma proteins from 50 to 85 % [86], [87]. Dox is mainly metabolised in the liver. It enters the cells via passive diffusion and has a rapid uptake by cells, but it does not cross the blood-brain barrier (BBB) [87]. After its metabolism 50% of the drug is already eliminated by the liver but its primarily excretion paths are biliary and faecal excretion [86]. Dox toxicity in rats was defined with a median lethal dose of 21800 µg/kg [84].

Table 1 - Physico-chemical characteristics of doxorubicin [84], [85].

Chemical structure	
Chemical formula	$C_{27}H_{29}NO_{11}$
Molecular weight	543.5 g/mol
Melting point	229-231 ºC
Water solubility	1.18 mg/mL (2% soluble)
LogP	1.27
LogD	0.02
PKa (dissociation constant)	Strongest acidic: 9.46 Strongest basic: 8.46

Doxorubicin has multiples mechanisms of action that lead to cell death. Some mechanisms are based on its interaction with DNA-associated enzymes. Dox intercalates into DNA base pairs and inhibits

13

macromolecular biosynthesis, producing a wide range of cytotoxic effects against human tumour cell lines [88], [89]. It can also induct DNA double-strand breaks and chromosomal aberrations by its interaction with topoisomerase II [84]. Upon enzymatic reduction, dox is able to originate ROS (OH·) which may cause extensive cell damage and cell death [87].

Despite its advantages a great problem with this drug is that it also induces apoptosis and necrosis in healthy tissues causing great toxicity in major organs like the heart, brain, liver and kidneys [89]. This can cause acute side effects like cardiac arrhythmias, nausea, vomiting, flares among others, and late side effects like myelosuppression, alopecia and chronic cardiotoxicity that can lead to heart failure [87]. For these reasons, over the years a great number of researchers have been studying to devise a DDS capable of enhancing the efficacy and selectivity of dox, being that in clinic is frequently administered in a liposomal solution, Doxil®.

The ideal DDS needs to ensure that the complex arrives and acts at the target location, and this targeting can be an active or passive process. In an active targeting, the nanocarrier (NC) surface is functionalized with ligands that bind to specific receptors in the target tissue, while in a passive targeting, the NC diffuses and accumulates at highly vascularized sites, such as tumours, where the overexpression of vascular endothelial growth factor (VEGF) increases vascular permeability [38]. The selective accumulation of the nanosystem in tumours, occurs via the enhanced permeability and retention (EPR) effect and active cellular uptake [90], [91]. Overall, these technologies are gathering great research attention, since they offer numerous advantages over conventional chemotherapy. They can be used solo (monotherapy) or synergistically combined with existing therapies, like magnetic hyperthermia, allowing a controlled release of the drug and enhancing its antitumoral efficiency [21].

Among the various nanoscale DDS, lipid nanocarriers (NCs) have emerged as central delivery systems, as they mimic in many ways the natural lipid environment found on biomembranes, presenting high biocompatibility and low toxicities when applied *in vivo* [92]. Moreover, in very limited cases, this kind of NCs show the capability to cross the BBB, which is relevant for the treatment of cerebral tumours. This is thought to happen because of their ability to mimic low-density lipoproteins (LDL) particles, being transported to the brain by a LDL receptor [93]. Examples of lipid NPs used as DDS are micelles, liposomes, ethosomes, nanoemulsions, nanostructured lipid carriers (NLCs) and solid lipid nanocarriers (SLNs) (figure 7). The last two particles are quite similar, differing only in the lipid matrix, which in SLNs contains only solid lipids, while in NLCs contains solid and liquid lipids [94].
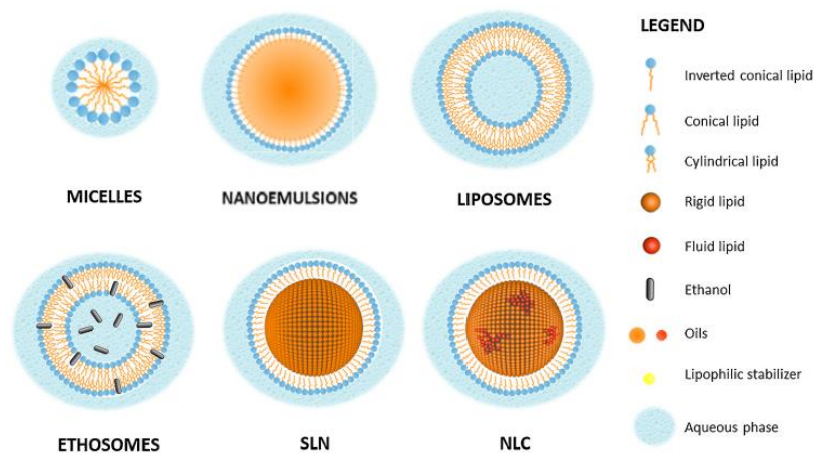
Figure 7- Types of lipid based nanocarriers. Adapted from [96].

The current development in cancer nanotechnology focuses on cancer detection, diagnosis, and treatment in a targeted manner using a single delivery system. Therefore, the focus of this work will be SLNs simultaneously loaded with a chemotherapeutic drug and magnetic and/or paramagnetic NPs. Thus, this bionanosystem will be able to provide: non-invasive imaging by MRI, diagnosis and follow-up; controlled release with MHT induction; and a synergistic treatment combining chemotherapy (dox) and MHT.

SLNs, also called lipospheres or solid lipid nanospheres, are solid lipids at human physiological temperature (37°), biodegradable, biocompatible and stable against aggregation or coalescence [46], [95]. In comparison with liposomes, SLNs present a higher stability, higher protection of the incorporated compound, higher entrapment efficiency for hydrophobic drugs, easy scale up potential and low production cost [96]–[98]. These NCs can be prepared by using solid lipids (at body and room temperature), including mono-, di- and triglycerides, fatty acids or waxes, water and surfactants to stabilize the particle and form administrable emulsions [95], [99], [100].

SLNs can be produced by various methods such as: microemulsification, solvent displacement, ultrasonication, phase inversion, solvent emulsification evaporation, solvent emulsification diffusion, melt-emulsification, cold homogenization and high-pressure homogenization (hot homogenization), with the latter being the most used due to its scale up potential [2], [95], [97], [99], [100]. Despite all the different mentioned methods, they can be summarized since all of these are based on lipid fusion. This process begins with the lipid phase being melted and posteriorly dispersed through high-speed agitation in an aqueous solution containing a surfactant, followed by a high-pressure homogenization, this way achieving a nanoemulsion. Lastly, emulsion droplets crystalize forming lipid NPs with a solid matrix. This matrix makes them ideal to encapsulate lipophilic drugs, such as doxorubicin, but the physico-chemical properties, polymorphic form and crystalline characteristics of the constituent lipids at biological

15

temperatures, can influence the drug loading into SLNs. This loading is done during the fusion step and before the high-shearing step in the lipid phase (for hydrophobic drugs) [97], [100].

The loading of dox in SLNs (dox-SLNs) to bypass MDR was addressed, showing that dox-SLNs efficiently enhance apoptotic cell death through higher accumulation of doxorubicin in dox-resistant breast cancer cells, overcoming chemoresistance [101]. Another study with dox-SLNs prepared via the solvent emulsification diffusion method, showed that the drug was released in higher rates at lower pH, as happens in tumour environment [102]. Mussi *et al.* studied dox-SLNs, evaluating at the same time the effect of docosahexaenoic acid (DHA), a fatty acid that increases the anticancer drugs activity and its encapsulation efficiency. This study showed greater dox release at lower pH and higher cytotoxicity in lung tumour cell line when DHA was incorporated, proving its efficiency as a nanoscale DDS against cancer [103]. Dox-SLNs were also studied for glioblastoma treatment, showing great drug cytotoxicity against glioma cell lines and increasing its permeation through a cell monolayer, assumed as a model of the BBB. These results validated SLNs as promising NC for dox delivery to the brain in glioblastoma treatment [104].

Overall, nanotechnology allied to drug delivery is very promising, and new formulations are now being intensively explored, thereby providing hope for new cancer treatment options in the near future.

1.4.2. Magnetic Resonance Imaging

Nowadays, MRI is one of the most powerful imaging tools, not only in clinical diagnosis but also in biological research. MRI is a non-invasive technology to obtain real-time images of the internal anatomy and physiology of living organisms and it's the most efficient available method to identify soft tissues. For that reason, it has been extensively used to study the brain, asses cardiac function and detect abnormalities in the organism [105]. In spite of all its capabilities, MRI still needs supplements to help distinguish abnormal soft tissues more accurately. For this effect, compounds known as contrast agents can be used. CAs are introduced into an organism to enhance imaging quality, being able to give anatomical and functional information.

MRI is based on the nuclear magnetic resonance (NMR) principle in which the nuclear magnetic moment of water protons aligns with an external magnetic field and is later excited with a radiofrequency (RF) pulse, generating an electric signal of a specific frequency (Larmor frequency, ω_0) [106], [107]. This pulse disturbs the protons spins from the direction of the applied magnetic field, and on their way back to their original low-energy state, two relaxation times can be defined: the longitudinal relaxation time (T_1, spin-lattice), which is based on energy transfer and reflects the length of time it takes to recover from a

decreased net magnetization in the direction of the applied magnetic field; and the transverse relaxation time (T_2, spin-spin), which is based on spin dephasing and reflects the length of time it takes for a NMR signal to decay in the perpendicular direction to the applied magnetic field (figure 8) [108]. The spin dephasing can be caused by local inhomogeneities due to tissue-inherent factors or to external sources. When this process accounts for both of these factors, the images produced are called T_2^* [108].
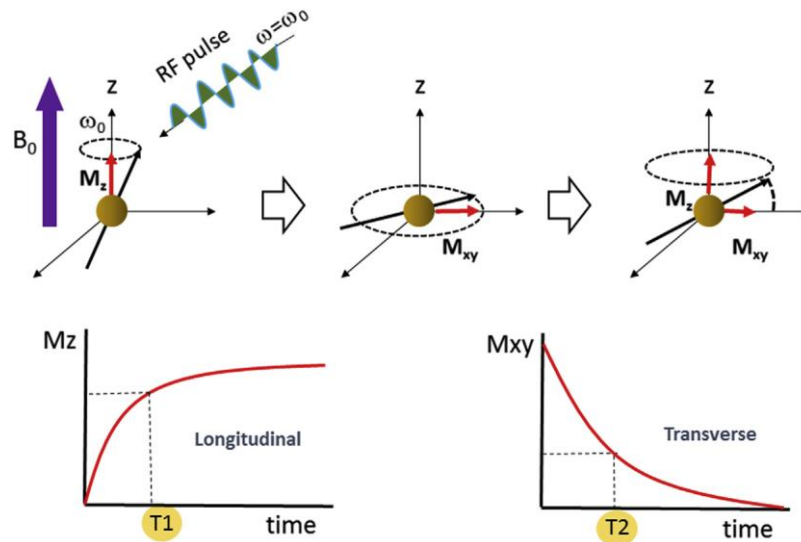
Figure 8 - Fundamentals of MRI based on nuclear magnetic resonance principle. B_0, external magnetic field [108].

Depending on the nature of the CAs, they can preferentially modify the T_1 or T_2 relaxation times [109]. The contrast that can be seen in MR images is the result of local variations of T_1 and T_2 relaxation times of water molecules in adjacent regions. Therefore, as the human body is composed of 60% water, CAs able to reduce the water relaxation times and subsequently enhance MRI contrast are needed [106]. These CAs are often based in (para)magnetic NPs. When placed under an external magnetic field, each particle creates a magnetic field of its own that induces field inhomogeneities in surrounding areas, which will disturb the proton spins of surrounding water molecules [108]. These events will change the MR signal, measured as a shortening of T_1, when there is a close interaction between protons and CAs, and a shortening of T_2, when there is a large susceptibility difference between the particles and the surrounding medium that results in small magnetic field gradients [108]. These measures are able to intensify the signal differences between the healthy tissues and the diseased ones, with T_1 CAs giving a bright contrast and the T_2 CAs offering a dark contrast.

The efficiency of a determined CA is given by its longitudinal and transversal relaxivity values, r_1 e r_2 respectively. These values are obtained by measuring the relaxation rates (inverse of relaxation times), R_1 ($1/T_1$) or R_2 ($1/T_2$), at different concentrations of CA. The higher the relaxivity of a given formulation, the higher its efficiency as an MRI CA. Thus, the smaller the relaxation time of CA, the greater its contrast enhancement efficiency [106]. Dual CAs are already being developed by several researchers [110], [111].

These are able to enhance simultaneously T_1 and T_2 signals, which will allow the observation of different tissues with increased specificity, being able to give a more accurate diagnose without the need of injecting more than one kind of contrast. For the evaluation of these formulations their relaxivities are still considered, but so is the r_2/r_1 ratio. This ratio is an important parameter defining CA performance: high r_1 values and r_2/r_1 ratios near 1 result in bright contrast in T_1-weighted imaging; high r_2 values with high r_2/r_1 ratios result in a dark contrast enhancement in T_2-weighted images; intermediate r_2/r_1 ratios enable a dual T_1-T_2 enhancement [112], [113].

Although ferric ions have 5 unpaired electrons that increase their r_1 value, iron oxide NPs possess high M_S and consequently a high r_2 relaxivity and a large r_2/r_1 ratio. For these reasons these NPs are not appropriate for T_1 contrast enhancement [114]. SPIONs were already commercialized as T_2 MRI CAs by AMAG Pharmaceuticals, Guerbet group and Bayer Schering Pharma [46], [52]. Due to their strong magnetization and superparamagnetic behaviour, these iron oxide NPs create local microscopic field inhomogeneities and activate the dephasing of protons. This way, the use of SPIONs results in a prolonged shortening of both T_2 and T_2^* relaxation times in the region around them, creating hypointense dark domains in MR images (negative contrast) [105], [115]. Furthermore, the high susceptibility of SPIONs allows the efficient tracking of labelled cells and can induce perturbations of the magnetic field in normal tissues, creating a "blooming effect" that demolishes the background around lesions [109]. As a result, SPIONs can be used to detect infection and inflammation, with higher accuracy than gadolinium-based CAs (paramagnetic T_1 CAs), since they can be phagocytised by macrophages leading to imaging hypointensity of macrophage infiltrated tissues [115], [116]. The larger magnetic moment of SPIONs compared to gadolinium CAs, explains the increased relaxivity of SPIONs compared with gadolinium at similar tissue concentrations [115]. Iron oxide NPs can also be used for functional MRI (fMRI) using the BOLD (Blood Oxygen Level Dependent) technique, being useful for the diagnosis of cardiovascular diseases and cancer [52]. Another important property of SPIONs is their potential for safe use in patients with chronic kidney disease, given its rapid removal through extravasations and renal clearance, which can be an advantage over the Gd-based CAs on the market [50], [115], [117], [118]. Despite all the advantages, these T_2 CAs also have disadvantages that limit their clinical use. One example could be the fact that their negative contrast is sometimes confused with other hypointense areas (calcifications, bleeding and metal deposits), which can deceive the clinical diagnosis [109]. For this reason, dual CAs active in both T_1 and T_2 imaging acquisition modes are highly needed to unequivocally distinguish physiological interferences.

Currently, only T_1 CAs are used in the clinic in Europe. These agents are based on a paramagnetic ion, Gd^{3+}, that due to its short blood circulation times and toxicity has to be strongly chelated with organic molecules [118]. Unlike T_2 CAs, T_1 CAs present high r_1 relaxivity and a small r_2/r_1 ratio, producing a bright (hyperintense) positive contrast. Manganese-based T_1 CAs have revealed a longer circulation half-time, that enhances the signal in tumours, a higher biocompatibility and they do not cause susceptibility artefacts such as T_2 CAs [114]. MnO NPs are great candidates to substitute/complement T_1 Gd CAs, used now in the clinic, since manganese, unlike Gd does not present significant toxic effects in the human body [114]. Studies have showed that nanosheets of responsive MnO_2, undergo structural changes under pH and redox stimuli, to enhance their MRI performance over 50 fold [6], [119], [120]. MnO_2 particles present an OFF-ON activatable character, since their paramagnetic character increases, upon reduction to Mn^{2+}, enhancing their MR signal [5], [6]. Mn^{2+} ion exhibits very prominent contrasting effects, revealing detailed physiologic and biological information. This ion allows the visualization of subanatomic structures of the brain and its neurological activity, unlike Gd^{3+} and T_2 CAs [109], [114].

1.4.3. Magnetic Hyperthermia

The use of hyperthermia in the treatment of tumours is an old practice that consists in rising the temperatures of a specific part of the body or the whole organism, above the physiological level (41-45°C). This treatment is considered as a supplementary treatment to chemotherapy, radiotherapy and surgery in cancer treatment [26], [121]. Conventional hyperthermia treatments, such as hot water bath, perfusion heating, high-frequency radiation or ultrasound, among others, were employed in the ablation of malignant tumours [122]. However, a problem with classic hyperthermia is the lack of homogeneity in the heat distribution profile, which can cause unwanted hot spots in healthy tissues and cold spots in the tumour (allowing its repopulation) [22]. Through the use of NPs, nanotechnology can improve hyperthermia, allowing for a more localised treatment (figure 9).
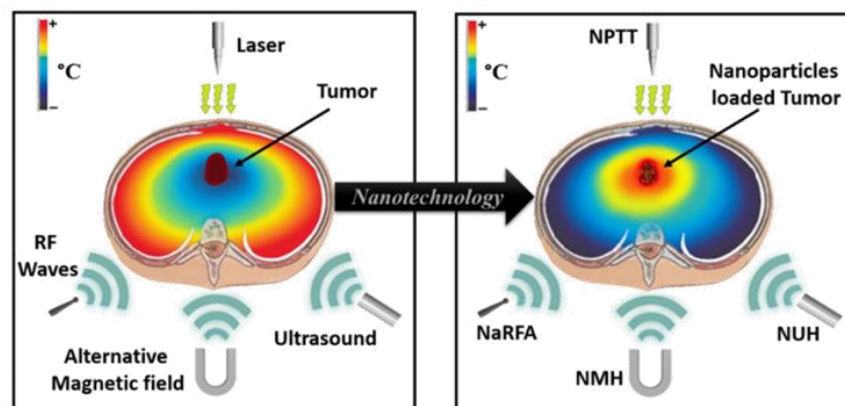
Figure 9- Nanoparticles concentrated inside the tumour can enhance the effects of conventional hyperthermia, while reducing possible side effects. NPTT: Nano-Photo-Thermal Therapy; NaRFA: Nano-Radio-Frequency Ablation; NMH: Nano-Magnetic Hyperthermia; NUH: Nano-Ultra sound hyperthermia [22].

Magnetic hyperthermia is a minimally invasive treatment, where MNPs produce heat through magnetic energy losses, that occur in the presence of an alternating magnetic field. This heat can be used for the ablation of tumours, since cancer cells are more sensitive to high temperatures (>41°C) than normal cells [22], [80]. One of the most sought-after administration routes for MNPs is through intravenous injection. One option to accumulate the MNPs in the tumours after injection is the use of magnetic fields; MNPs are guided towards the target tissue due to the presence of a sufficiently strong magnetic field, that can make the NPs overcome the blood flow [4]. An adequate MNP functionalization can also improve the targeting of the NPs. On a recent study, Liao *et al.* studied the effect of iron oxide NPs functionalized with alginate and galactosamine as the cell-targeting ligand (Fe₃O₄@Alg-GA) in MHT *in vitro.* The results showed that this nanostructure is able to promote hyperthermia, significantly decreasing the cell viability in a human hepatocellular cell line (HepG2) [53].

Currently, iron oxide NPs are considered the favourite heating agent for MHT, because of their interesting size-dependent properties, biocompatibility, minimal toxicity and ease of excretion and functionalization. SPIONs are already commercialized for hyperthermia purposes by the European Institute of Science and Magforce (NanoTherm®) [52]. In multi-domain and single-domain particles, the main heating processes are hysteresis losses and relaxation losses (Néel or Brown relaxation), respectively [4], [22]. Thus, the heating of SPIONs is mainly due to relaxation losses during the reorientation of the magnetization under alternating field exposure. Néel relaxation results from random flips of the spins without particle rotation, being the only relaxation process in MHT with immobilized NPs [22]. Brown relaxation results from frictional forces if the particle can rotate in a medium of low viscosity [48]. The quantity of heat produced by the MNPs should be as high as possible, in order to diminish the dose, and it depends strongly on NPs properties such as: mean size, magnetic anisotropy (shape), M_S and on the amplitude and frequency of the oscillating magnetic field [48]. An important characteristic of MNPs utilized in clinical hyperthermia is their specific absorption rate (SAR), defined as the rate at which electromagnetic energy is absorbed by unit mass of a biological material [80], expressed in W/g:

$$SAR = \frac{cdT}{m_{NP}dt} \tag{1}$$

where c is the heat capacity, and dT is the temperature increment in a certain time (dt), and m_{NP} is the mass of the NP in question per mL of water. The SAR, that results from loss processes, depends on the applied AMF frequency and on the magnetic field. The efficiency of MNPs in energy conversion is of great importance, and for this reason, the ideal particle would present a high SAR at low AMF, since it implies

a lower time of residence of the NPs in the human body and lower dosages to be administered [4], [80], [123].

MHT is most of the times used in combination with other therapies such as radiotherapy and chemotherapy. The main aim of radiotherapy is to eliminate cancer, maintaining the therapeutic dose in the diseased cells, while reducing the radiation dose on adjacent healthy cells. Therefore, controlling and killing the tumours at a cellular level is of great importance. This can be achieved using both targeted MNP and an AMF, to sensitize tumour cells for posterior radiotherapy treatments. In a clinical trial, Maier-Hauff *et al.* investigated the efficacy of MHT combined with radiation therapy in the treatment of glioblastoma multiforme. The results showed that MHT was well tolerated by all patients and the median survival rate was greatly increased [124]. The use of MHT also reduced radiation dose, leading to a prolonged overall survival [125], [126].

Chemotherapy can also be enhanced with the application of concomitant MHT. MHT can increase the blood flow, perfusion and blood vessel pore size in the tumour, facilitating drug accumulation and penetration in solid tumour tissues. MHT can also improve drug cytotoxicity through an enhanced intracellular uptake of drugs, because of the increased cell membrane permeability. Inhibition of DNA repair and acceleration of cytotoxic reactions, can also contribute to increase drug toxicity in combined treatments [121]. Itoh *et al.* evaluated the thermal enhancement of cisplatin and adriamycin cytotoxicity *in vitro,* using human bladder cancer cell line (T24). The results showed that the combined chemotherapy and MHT treatment had a higher anti-tumour effect than either hyperthermia or chemotherapy alone. The survival rate was the same in combined and drug alone treatments, however the drug concentration was 10-fold higher in the latter. This indicates that the quantity of drugs used can be significantly reduced in the combined treatment, hence limiting chemotherapy side effects [127].

Overall, MNPs can be used in diverse biomedical applications, being extensively explored in the field of diagnosis and treatment of cancer. Recent research has been focused on the use of these NPs for early detection and treatment of solid tumours, creating in this way an innovative tool for the fight against cancer.

1.5.   Objectives

The main aim of this project is the development and initial validation of a novel theranostic nanocomposite system to help in the fight against cancer. The individual goals of the project are:

- The design of a nanocomposite comprising a lipid matrix, a chemotherapeutic drug and a (para)magnetic core;

- The characterisation of this new nanosystem in terms of physico-chemical properties;

- The functional characterisation of the nanosystem in terms of performance as MRI contrast agent, MHT effector and controlled drug delivery vehicle.

CHAPTER 2 - CHARACTERISATION TECHNIQUES

In this chapter, the techniques required for the physico-chemical and functional characterisation of the developed nanoparticles will be synthetically explained, to give a better insight and understanding of their principles and functioning.

2.1. Dynamic light scattering

Nowadays, dynamic light scattering (DLS) is a standard technique widely used in the industry, such as in biopharmaceutical industry, to determinate the size, polydispersity index (PI) and zeta potential of particles. This technique allows the evaluation of the hydrodynamic size and shape of NPs through their Brownian motion, with nanometric resolution. Brownian motion is the random movement of particles suspended in a liquid medium, resulting from the particles collision with the solvent molecules that surround them [128]. The velocity of this motion is called translational diffusion coefficient (D) and is dependent on the particle size: smaller particles move more rapidly, while bigger particles move more slowly [129]. Therefore, the hydrodynamic diameter of the particles can be calculated with this coefficient, by using the Stokes-Einstein equation (2):

$$d(H) = \frac{kT}{3\pi\eta D} \tag{2}$$

where, d(H) is the hydrodynamic diameter, k the Boltzmann's constant, T the absolute temperature, η viscosity and D the translational diffusion coefficient [128].

It should be noted that the DLS measured radius is referred to how the particles diffuse within a fluid. Thus, by definition, the DLS measured radius is the radius of a hypothetical hard sphere, that diffuses with the same speed as the particle under examination. Hence, the diameter calculated from the diffusional properties of the particle is indicative of the apparent size of the solvated particle [130].

A typical DLS system, shown in figure 10, comprises: ① a laser, used to illuminate the sample contained in a cell ②; a detector ③ positioned either at 173° or 90°, used to measure the fluctuation of the scattered light; an attenuator ④ used to reduce the intensity of the scattering if too much light is detected; a correlator ⑤ that stablishes a correlation between the size of the particles and the scattering intensity at successive time intervals; and a computer ⑥ where the information is analysed [128].
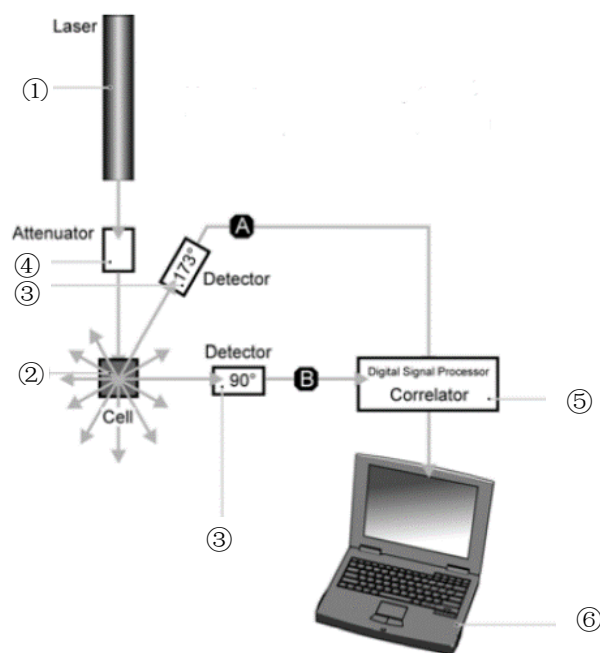
For the two positions available for the detector (A and B, figure 10), a 173° angle it's the most reliable to measure small NPs, because the light detected at this angle is essentially scattered by smaller NPs, and this way the effect of contaminants like dusts, can be significantly reduced since they mostly disperse light at 90°. For size measurements the dilutions used are very important, since they can influence the polydispersity index of the sample and make the measurements less reliable (low PI). The PI is indicative of the homogeneity of a given formulation, since a big PI indicates the existence of NPs with different sizes or agglomerates. According to the literature a PI<0.2 is acceptable for lipid-based delivery systems, however for SLNs containing not only MNPs, but also a drug, is very difficult to obtain a PI so low [131]. Thus, in this work, values below 0.5 were considered good, and only values over 1 were considered indicative of a polydisperse formulation.

Electrophoretic Light Scattering (ELS) is a technique used to measure the zeta potential of the particles. Zeta (ζ) potential is defined as the electric potential difference between two components of the liquid layer that surrounds the particle: the slipping plane, where the ions are more diffuse and the Stern layer, where the ions are strongly connected to the particle (figure 11A) [132]. In other words, it is a measure of the effective electric charge on the particles surface [133]. Knowing the value of this electric charge is important because it is indicative of the system stability: a very positive or very negative value, superior to 30 mV or inferior to -30 mV, is considered to have enough repulsive force to prevent aggregation and make the formulation stable; on the other hand, values between -30 and 30 mV can result in particle aggregation due to the van der Waals attractive forces [134].

24

To determine the ζ-potential an electrode cell is used (figure 11B). Briefly, the diluted sample is put inside the cell, then a laser goes through the sample and a magnetic field is applied in the electrodes of the cell, creating a potential difference. This potential difference forces the charged NPs to migrate in the direction of the electrode with the opposite charge with a determinate velocity, known as electrophoretic mobility, which is linearly related to their ζ-potential [135].
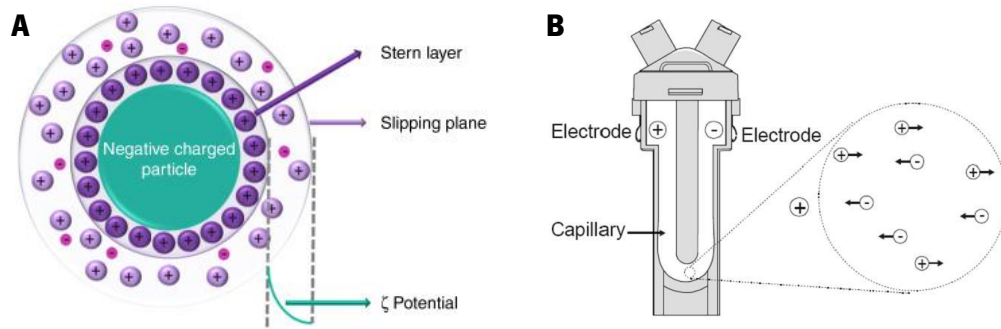
Figure 11 - A: Diagram showing the ionic concentration and ζ-potential, as a function of distance from the surface of a negative charged particle, suspended in a dispersion medium [131]; B: schematics of a typical electrode cell [133].

2.2.   Spectroscopy

Spectroscopy is defined as the study of the interaction between matter and an incident electromagnetic radiation that results in the absorption or emission of light. The results are normally presented in a spectrum of radiation intensity as a function of wavelength.

2.2.1. Ultraviolet-Visible absorption spectroscopy

UV-vis (ultraviolet - visible) spectrophotometry is a quantitative analytical technique with a radiation absorption near-ultraviolet (180-390 nm) and/or visible (390-780 nm) by chemical species in solution or in gas phase [136]. This energy absorption allows an electronic transition of a photon, from a ground state to an excited state of superior energy, as long as the energetic difference between those states is the same or lower than the energy of the absorbed radiation [137]. In spectroscopy is important to know the transmittance of the sample, that refers to the light that passes through the sample, in order to get the material absorbance at a determined wavelength λ (3)(4):

$$T_{(\lambda)} = \frac{I}{I_0} \tag{3}$$

$$A_{(\lambda)} = -\log(T_{(\lambda)}) \tag{4}$$

where I_0 is the incident light intensity and I is the transmitted light intensity. When it goes through an absorbing medium, the incident light decays exponentially, according to the expression (5):

$$I = I_0 \cdot e^{-\varepsilon_{(\lambda)} \cdot c \cdot l} \tag{5}$$

These expressions are related and can be simplified by using the Lambert-Beer's Law (6).

$$A_{(\lambda)} = \varepsilon_{(\lambda)} \cdot c \cdot l \qquad (6)$$

where $A_{(\lambda)}$ is the absorbance at a determined wavelenght, $\varepsilon_{(\lambda)}$ the molar absorption coefficient, c the concentration of the absorbing solution and l the distance of the absorbent medium that the radiation goes through.

The Lambert-Beer law states that the decrease in the intensity of monochromatic radiation at a determined wavelength, that passes through an absorbing medium, is proportional to the intensity of that radiation, to the concentration of the absorbent species and to the thickness of the absorbent medium that the radiation goes through. However, this is just valid when using a monochromatic radiation, measuring diluted solutions with only one absorbent species. One there is more than one absorbing species, the absorbance will be the sum of all the absorbances by each species.

An UV-Vis spectrophotometer uses two distinguished lamps for the emission of electromagnetic radiation: a deuterium lamp (D$_2$) for the UV region and a tungsten lamp for the Vis/IR region [138]. In the most common design, first the radiation goes through a filter and a slit to control how much light enters the spectrometer and accurately select a monochromatic radiation, then a monochromator selects the range of wavelengths chosen. Afterwards the beam is split in two by the beam splitter, to focus in both the reference cell (with the solvent) and the sample cell. Then the photodetector, detects the light that passed through the sample and the reference and creates an absorbance spectrum as a function of the wavelength. Figure 12 schematizes a typical UV-Vis spectrophotometer [139].
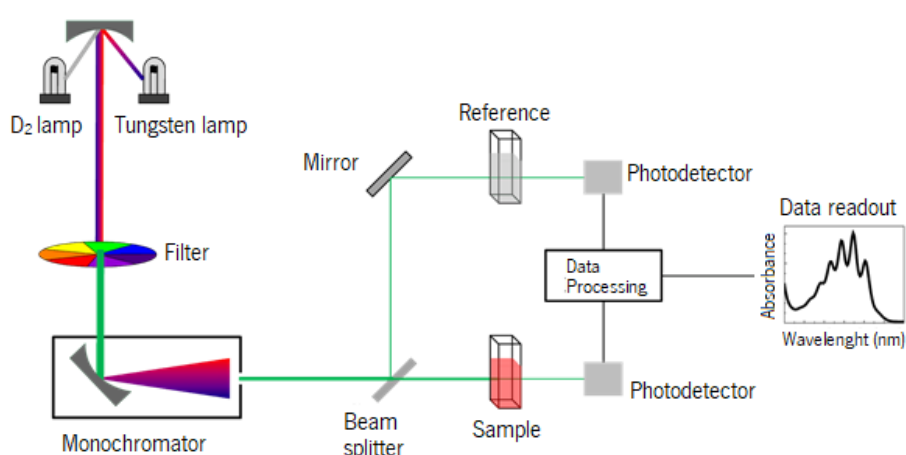
Figure 12 - Schematic representation of a typical UV-Vis spectrophotometer. Adapted from [137].

The absorbance calculated by the equipment is dependent on the incident light, the material of the cell and the components of the sample including the solvent. Thus, it is important to have a reference

cell to create a baseline to deduct the absorbance of the solvent and the cell material, obtaining this way a more clean and precise absorbance spectrum of the samples.

2.2.2. Fluorescence spectroscopy

Fluorescence spectroscopy is a sensitive and specific tool for biochemical and biophysical studies and can be complementary to absorbance spectroscopy [140]. Once a molecule absorbs light and transits to an excited state, it tends to be unstable leading the molecule to relax back to the ground state. This relaxation can happen through non-radiative and radiative processes. It is a non-radiative process if it occurs due to the collision of the excited molecule with solvent molecules, while it is a radiative process if it occurs through the emission of photons. Fluorescence spectroscopy is based on a light emitting process (radiative process) that is triggered by the absorbance of a photon, excited with an excitation wavelength (λ_{ex}), characteristic of the molecule being analysed [141]. The emission process, called fluorescence, happens when the excited molecule returns from the lowest vibrational level of the excited state (S_1) to the several vibrational levels of the ground state (S_0). In this process the emitted light disappears right after excitation.

Figure 13 shows a general and simplified scheme of a spectrofluorometer [142]. The functioning of this equipment is very similar to the UV-Vis. Briefly, a continuous source of light (Xenon lamp) shines onto an excitation monochromator, which selects a band of wavelengths. This monochromatic excitation light is directed onto a sample which first absorbs and then emits luminescence. The luminescence is directed into a second, emission monochromator, which selects a band of wavelengths, and

Figure 13 - Simplified representation of a spectrofluorometer [140].

shines them onto a detector. The signal from the detector is reported to a system controller and host computer, where the data can be manipulated and presented, using special software.

2.2.3. Fourier Transform Infra-red spectroscopy

Fourier transform infra-red spectroscopy (FT-IR) provides a sensitive probe for the identification of specific functional groups in different materials, using an infrared (IR) light source to measure the absorption of a solid, liquid or gas. When the IR radiation is absorbed, the molecule is excited to a higher vibrational level if its dipole moment changes during the vibration [143]. IR radiation corresponds to the energy required for rotational, translational and vibrational energy transitions, being that vibrational

transitions are the strongest and most important in IR spectroscopy [144]. Generally, a molecule with N atoms has 3N degrees of freedom, that are the maximum number of potential transitions of that molecule. All molecules have three translational degrees of freedom, being able to move in three directions. But if the molecule is nonlinear it also has three rotational degrees of freedom and if it's linear, it has two rotational degrees of freedom. Thus, nonlinear and linear molecules have 3N-6 and 3N-5 vibration modes, respectively [144].

When irradiated, molecules absorb frequencies that are characteristic of their structure, being possible to determine their vibrational frequencies and consequently the corresponding functional group. The most common vibration modes are: bending, that involves changes in the bond angles of the atoms and can be further classified as scissoring, rocking, wagging and twisting; stretching, that changes the length of the bonds between atoms; and torsional modes that involve the twisting of the backbone of the molecule (figure 14) [143], [144]. These motions can also be symmetrical or asymmetrical and in-plane or out-of-plane, and can only be IR active if the corresponding vibration changes the molecular dipole moment [145] .
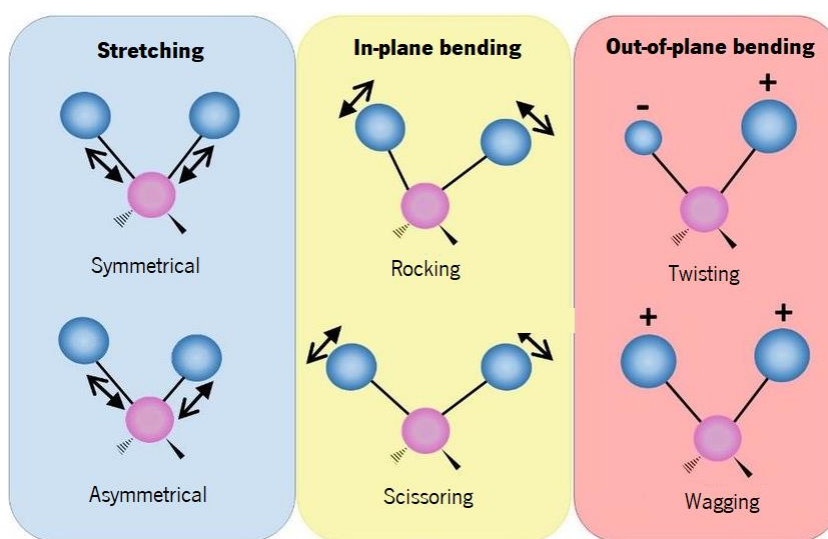
Figure 14 - Possible vibrational modes of molecules. Adapted from [145].

Opposed to other spectroscopies FT-IR has a high spectral resolution, good signal-to-noise ratios and an ability to measure a broad region of the spectrum, normally from 4000 to 400 cm^{-1}, in little time [146]. The absorption bands of the spectra are characterised by its frequency, intensity and shape, which are unique features for each individual molecule. The band frequency indicates the presence of certain functional groups, the band shape gives information about the group functionality and the material purity, and the band intensity provides information on the amount and type of a determined functional group of the molecule, by comparison with other bands [144].

Experimentally, first the background spectrum of the IR source is recorded. Next, the spectrum of the IR source with the sample in place is recorded. At this point, the radiation of different wavelengths goes through a Michelson interferometer, where the light is directed to a beam splitter that reflects half of it into a fixed mirror and other half into a movable mirror, creating two different optical paths. The beams from both mirrors are returned to the beam splitter and partially reflected to the detector. The Michelson interferometer is responsible for recombining these two beams, conducting them into the sample, and then into the detector that measures the optical path difference of the beams. Afterwards, the computer takes that raw absorption data (interferogram) and conducts a math process known as the Fourier Transform, to decompose the signal obtained into its constituent frequencies, this way generating a readable absorbance spectrum [147]. In figure 15 is shown a schematic representation of this process [148].
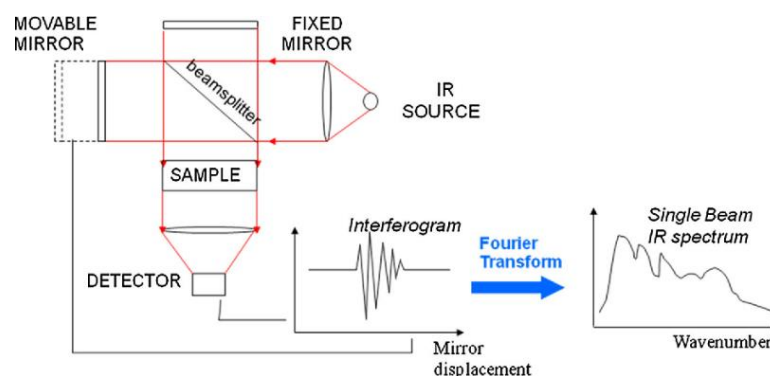
Figure 15- Schematic representation of a FT-IR spectrometer [146].

2.2.4. Inductively coupled plasma-atomic emission spectroscopy

Inductively coupled plasma-atomic emission spectroscopy (ICP-AES) is a widely used technique to identify and quantify the presence of metals in different samples. It is a commonly used technique in nanomedicine to quantify the mass percentage of a determined element in nanocomposites. It combines an induced coupled plasma, with a spectrophotometer to obtain a spectrum that is representative of ppm levels of trace elements [149]. These spectrophotometers are capable of running almost every metal in a large number of samples per run [150].

The source of an ICP-AES instrument is an argon-based plasma that is generated by a RF coil and when power is applied an alternated current oscillates and creates a magnetic field from the coil to the torch. This field helps to maintain the argon flow and breaks down the argon gas into ions and electrons, this process is called inductively coupled plasma [150], [151]. The plasma provides high thermal energies from 5500 to 6500 K, that can destroy to a great extent the molecular bonds of most elements, this way the analytes dry, dissociate and atomize [152]. To get the sample into the plasma it must be nebulized. The sample is pumped into a pneumatic nebulizer that forms an aerosol and then enters a spray chamber

that selects very small droplets [150], [152]. These droplets are carried by the argon gas into the plasma and their atoms collide with energetically excited argon species, ionize and emit characteristic atomic and ionic spectra that are collected by a detector [149]. The emitted radiation is specific to the element and its intensity is proportional to the element concentration in the sample [150].

Before reaching the detector, the emitted light is focused onto the entrance slit of a spectrometer by using a convex lens arrangement (figure 16). The light is then separated by a diffraction grating into its component wavelengths in a spectrometer. The spectrometer can have different configurations to achieve different ends. In the case of the Echelle spectrometer represented in figure 16, the diffracted light from the grating focuses on a prism, suffering a secondary dispersion, this way avoiding spectral overlap [153]. With respect to the detection system the spectrometer can also be sequential or simultaneous. In the sequential spectrometers only the radiation from a selected wavelength is detected, being that this selection occurs by rotating the grating. In the simultaneous spectrometer the detector, normally a charge coupled device (CCD) detector is used and allows the simultaneous analysis of many wavelengths or elements [149], [153]. This equipment allows a large number of samples to be analysed with a very high sensitivity and a very broad dynamic range.
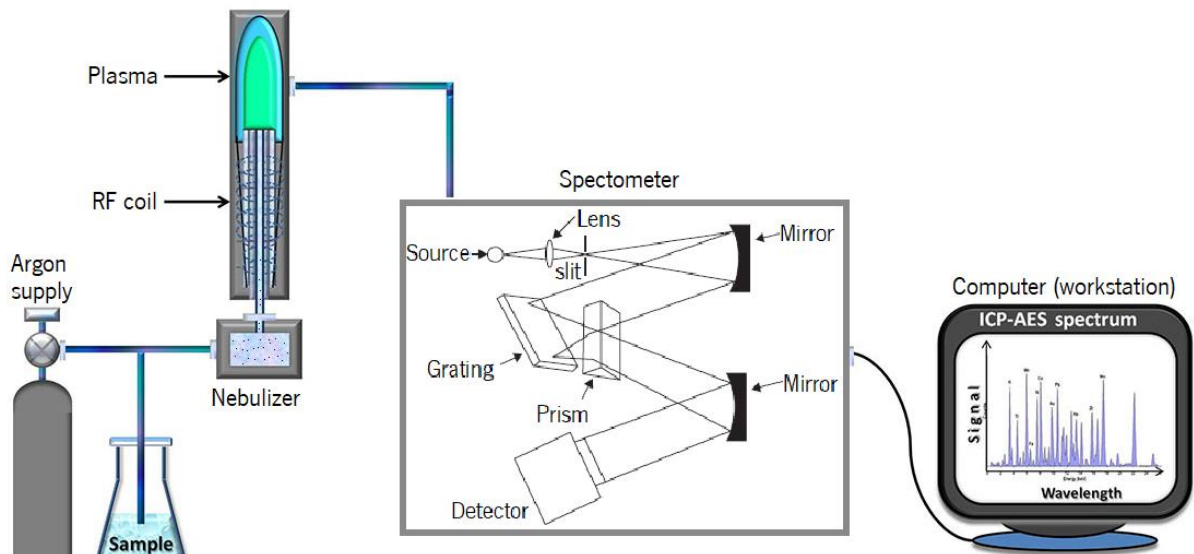
Figure 16 - Schematic representation of an ICP-AES equipment with an Echelle spectrometer. Adapted from [151] and [153].

2.3. Microscopy

Microscopy is a technical field widely used in research to study materials or specimens not visible to the naked eye, using microscopes. In this work optical and electron microscopy were used to study the NPs by themselves and applied in cells.

All microscopes present a resolution limit that can be influenced by the source and the lenses conditions. Ernst Abbe discovered the optical equation (7), called Abbe diffraction limit, that indicates the requirements needed to obtain a clear image, without distortion caused by aberrations. This equation states that the resolution of a given instrument is proportional to the wavelength of the transmitted light, and inversely proportional to the numeric aperture (NA) [154].

$$d = \frac{\lambda}{2n \sin \theta} = \frac{\lambda}{2NA} \tag{7}$$

where λ is the wavelength of the light source, n is the index of refraction of the medium between the object and the objective and θ is the acceptance angle of the objective lens. The $n \sin \theta$ represents the numeric aperture, that measures the capacity of a lens to receive the transmitted light [154]. Since there's a clear dependence of the resolution over the wavelength, optical microscopy was used to observe cells, which are bigger, and electron microscopy was used to observe NPs, which are smaller.

2.3.1. Optical microscopy

In optical microscopy a beam of light is directed to the sample and transmitted through or reflected by it. The microscope allows its observer to analyse the effects of light as it interacts with the sample, obtaining a magnified image of the sample.

For this work an inverted optical microscope with a camera was used. This microscope distinguishes itself from the regular upright microscopes, because its objectives are placed below the stage, while its light source and condenser are on top [155]. The light source, that can be a LED (light-emitting diode) illuminator or a halogen lamp, shines through the condenser lens that guides the light evenly across the field of view (FOV) of the microscope. The image is amplified by the objectives and eyepiece lens. These microscopes can have a digital camera connected to them, to make easier to take pictures of the sample. They normally support various methods like fluorescence microscopy, phase contrast method and bright field (BF), among others.

2.3.2. Confocal microscopy

Confocal microscopy is a type of optical microscopy, that allows the acquisition of fluorescence micrographs with increased contrast and resolution, using a focused laser for excitation and a pinhole to block out-of-focus light [156]. Two dimensional (2D) images are acquired plane to plane, at different depths, which allows fluorescence detection in thick samples. Tri dimensional (3D) objects can be visualized by scanning several planes and stacking them, using a microscopy deconvolution software (z-stack). This equipment allows the visualization of different sections of a sample using different

fluorophores, through the illumination of the sample with a multiwavelength laser that uses various laser excitation lines [157].

Figure 17 shows a general and simplified scheme of a confocal microscope. A laser ③ is used to illuminate a source pinhole ④ that focus the light into a dichroic mirror or beam splitter ⑤. Then the light is reflected into an objective ⑥ that converges the light into a single point in the focal plane of the specimen. The emitted fluorescent light (purple line) from this focal point is focused at the detector pinhole ② and reaches the detector ①. The light emerging from objects outside that plane (red line) is largely excluded by the pinhole, not contributing to the final image [158], [159]. This microscopes

Figure 17 - General representation of a confocal microscope [157].

can also include excitation and emission filters, allowing a more detailed fluorescence imaging [157]. This process contributes to an image with more resolution and less artefacts, ideal to the observation of cells and their components.

2.3.3. Transmission electron microscopy

Transmission electron microscopy (TEM, an acronym that also stands for transmission electron microscope) is a microscopy technique in which an accelerated electron beam is transmitted through a sample. Through this technique it is possible to analyse the morphology, composition and the crystallographic structure of materials, with a resolution of approximately 0.2 nm [30]. This high resolution is obtained through the acceleration of the electrons. The wavelength of an electron is dependent upon accelerating voltage (generally from 80 to 300 kV), accordingly to the equation (8):

$$\lambda = \frac{h}{\sqrt{2meV}} \tag{8}$$

where h is the Planck's constant, m the mass of the electron, e its electronic charge and V the accelerating voltage applied. When the applied electron beam is accelerated with high values of voltage, TEM can obtain high resolution for extremely short wavelengths, and the previous equation can be approximated to the following (9):

$$\lambda \sim \frac{1,23}{\sqrt{V}} \tag{9}$$

Therefore, the desired electron wavelength can be achieved by varying the accelerating voltage of the electron beam. The higher the accelerating voltage, the smaller the wavelength of the electrons and the higher the possible achievable resolution [160].

Figure 18 shows the schematics representation of a TEM. The mechanism of imaging of TEM can be explained as follows: an electron gun generates an electron beam, that is controlled by many electromagnetic lenses and metal apertures, arranged sequentially along the microscope column [161]. The column should maintain a high vacuum, since the electrons cannot move in atmosphere. The focusing phenomenon occurs because the electrons behave as negatively charged particles, that are deflected by the magnetic and electric components of the microscope [160]. The condenser lens and aperture, exclude high angle electrons, modulating the electrons into a defined beam that focus in the sample [161]. The ideal

Figure 18 - Schematic representation of a TEM. Adapted from [159].

thickness of the sample should be around 100 nm, so that the electrons can pass through [160]. The objective lens, right above the specimen stage, focuses the transmitted electrons into one point in the image plane obtaining the first image. With the objective aperture, a well-defined electron beam is attained and an electron diffraction pattern can be obtained [161]. Then, the projector lens magnifies the image and the diffraction pattern onto the phosphorescent screen, to translate the electron image information into a visible form [160]. Normally this equipment is fitted with electron detection system, mainly charged coupled devices. A CCD camera is positioned above the phosphorescent screen, to acquire digital images of the specimen. Additional lenses and detectors can be installed to perform different TEM modes, or simply to correct chromatic aberrations.

Electrons are one type of ionizing radiation, that produces a wide range of secondary signals when interacting with the sample, which will be dependent on the thickness of the sample. The thicker the sample, the longer the electron path, and the more likely it is that an electron will experience multiple scattering events [161]. Primary and secondary electrons, transmitted and back-scattered electrons (BSE), low energy Auger electrons and X-rays are some examples of scattering events (figure 19) [160].
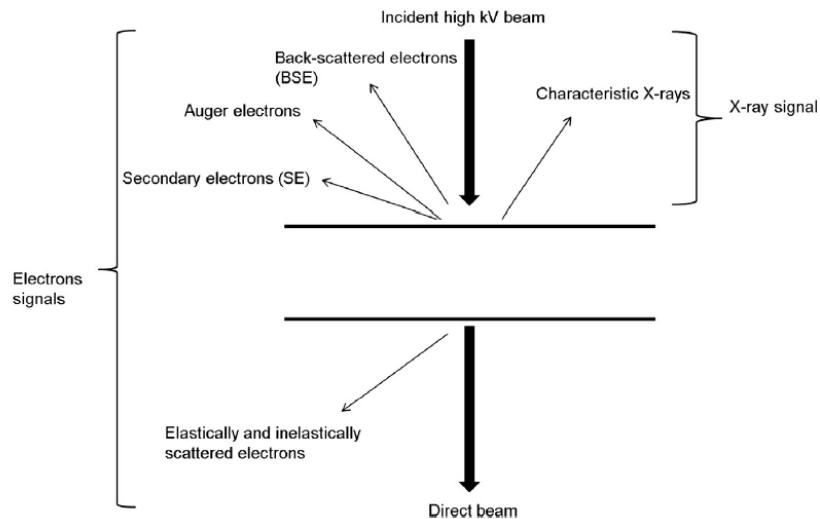
BSE and transmitted electrons may experience elastic (no energy loss) or inelastic (energy loss) scattering, that can be useful in different TEM modes. Many of these signals are used in other techniques like scanning transmission electron microscopy (STEM) and energy dispersive X-ray spectroscopy (EDX), in the case of characteristic X-rays [162].

2.3.3.1. STEM-EDX mode

Scanning transmission electron microscopy is a mode that can be available in TEM. For this mode, the instrument needs to be fitted with STEM scan coils, which can scan a focused electron beam across the sample. The TEM would also need to be equipped with BF (bright field) and annular dark-field (ADF) detectors for imaging [163]. This technique can be combined with analytical techniques like EDX, to obtain a mapping of the elemental composition of the sample [160].

For the EDX an X-ray detector needs to be mounted in line-of-sight of the specimen. The characteristic X-rays generated by the interaction of electrons with the sample, are collected and counted according to their energy by the detector. This way, in a little time collection, an EDX spectrum can be obtained, allowing an elemental analysis of the sample [164]. Combining this technique with STEM, an X-ray spot spectrum can be attained from many locations across the sample. This enables a BF or ADF image acquisition with the elemental distributions marked in specific areas of the sample surface, throughout the image [161].

Electron microscopy techniques are contributing significantly in various areas of research, being particularly relevant in the study of the morphology and chemistry of NPs, so useful for drug delivery studies.

2.4.   Thermogravimetric analysis

Thermogravimetric analysis (TGA, also thermogravimetric analyser) is an essential technique used for material characterisation regarding their composition. It allows to monitor the mass of a substance as a function of temperature over time [165]. The sample is positioned under a controlled isothermal or varying temperature in a given atmosphere [166]. The TGA relies on a high degree of precision in three different extents: weight, temperature and weight change with temperature over time. This permits the determination of degradation temperatures, the quantity loss of water or solvent, decarboxylation, the level of organic and inorganic components, the amount of residue remaining, among others [167], [168].

Figure 20 shows a schematic representation of thermogravimetric analyser with horizontal furnace, which helps minimize turbulence caused by thermal buoyancy and the purge gas [165]. This equipment consists of a sample pan that is supported by a precision balance ①. These components are contained inside a furnace, that can be vertical or horizontal, and achieve temperatures as high as 2700 K [166], [167]. A thermostated balance chamber ②, is used to minimize environmental influences in the balance cell and two adjustments ring weights ③, to help in the weight measurement. Temperature sensors are placed right above the sample pan ④, to measure its temperature, and in the furnace ⑤, to measure the atmospheric temperature inside the furnace. A furnace heater ⑥ is also present inside the furnace to either heat it or cool it [165]. A purge gas supply system consisting of a gas inlet ⑦ and a gas outlet ⑧, controls the sample environment. This gas may be inert or a reactive gas that flows over the sample through a reactive gas capillary ⑨ [168].
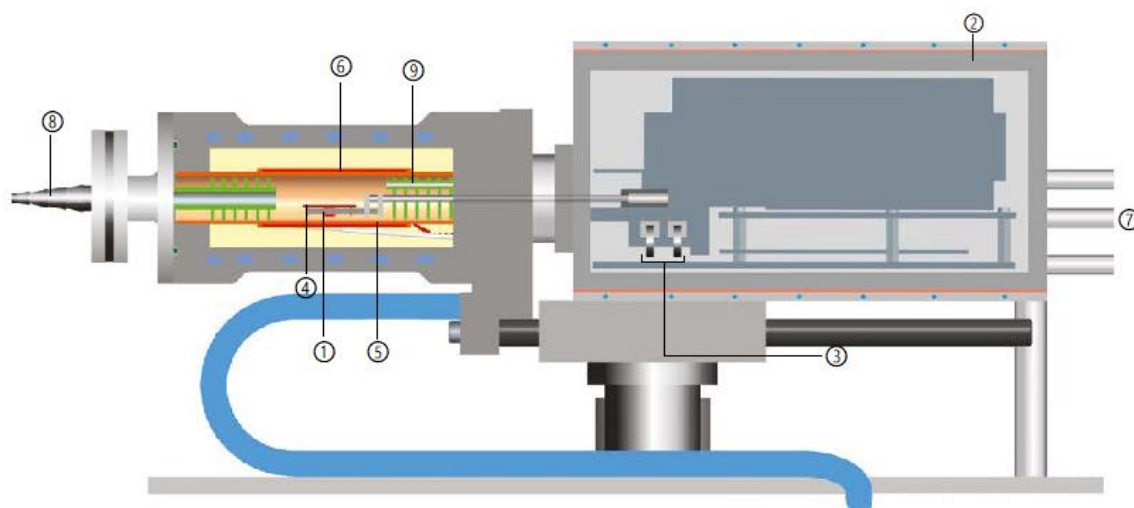
Figure 20 - Schematic representation of a TGA with a horizontal furnace. Adapted from [163].

The descending TGA thermal curve indicates the weight loss occurred in function of temperature. For simultaneous detection of thermal events, the TGA can feature a DSC (differential scanning

calorimetry) heat flow measurement [165]. This measurement can be attained in the presence of a DSC sensor that detects thermal events, like fusion and crystallization, being able to register accurately the exact transition temperatures.

2.5. Magnetic measurements

2.5.1. Vibrating sample magnetometer

A vibrating-sample magnetometer (VSM) is a scientific equipment used to measure the magnetic properties of a material. In this technique a sample is vibrated sinusoidally at a small amplitude, perpendicularly to a homogeneous magnetic field [169]. The vibrating component causes a change in the magnetic flux, which generates an electrical signal in the coils based on Faraday's Law of Induction (10). This law states that an electromotive force (ε in volts) is induced in a conductor by a time varying magnetic flux [170]:

$$\varepsilon = -N \frac{\Delta \phi_B}{\Delta t} \tag{10}$$

where N is the number of turns of a coil, $\Delta \phi_B$ the change in magnetic flux and Δt the change in time.

Figure 21 shows a schematic representation of a VSM. First, the electromagnets create a uniform magnetic field, that magnetize the sample [170]. Then, the electrodynamic sample vibrator induces a sinusoidal vibration of the sample at constant frequency, with the help of a straw used as the sample holder. The oscillating magnetic field of the vibrating sample causes a change in the magnetic flux of the nearby pick up coils (detection coils). This change induces a voltage in the suitable located pick-up coils, that is proportional to the magnetization (M) of the sample. A second voltage can be induced in similar coils, called reference coils, by a reference sample that can be a permanent magnet. This will generate a reference signal that can make the measurements insensitive to changes of vibration amplitude and frequency, magnetic field inhomogeneities among other instabilities [169]. Both the signals coming from the different sets of coils are processed by a lock-in amplifier and then converted into a graph of magnetization versus magnetic field strength (H), normally referred to as hysteresis curve [171].
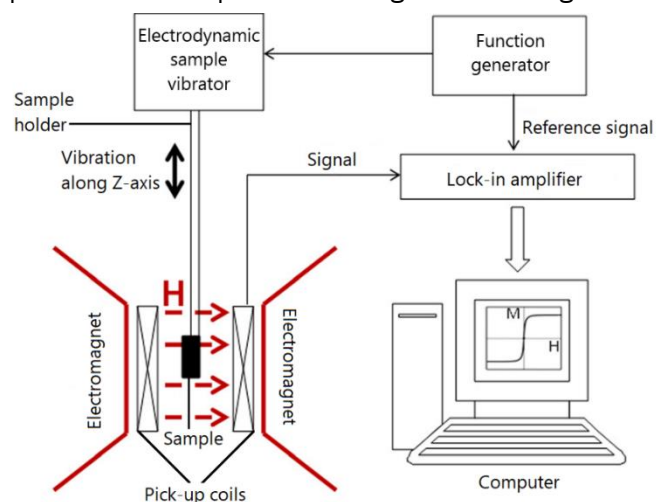
Figure 21 - Schematic representation of a measurement process by VSM. Adapted from [168].

2.5.2. Superconducting quantum interference device

The superconducting quantum interference device (SQUID) is a very sensitive magnetometer able to detect changes in an applied magnetic flux. This device can measure the magnetic properties of a material with a field resolution of 10^{-17} T, based on superconducting loops containing Josephson junctions. To have superconductivity is necessary to refrigerate the system with liquid Helium, below a critical temperature of 4.2 K. A SQUID device consists of a superconductor ring interrupted by one or more Josephson junctions (figure 22A) [172]. The Josephson junctions create a resistive barrier between two superconducting regions, leading to electron tunnelling across the junction [173]. If a constant biasing current is maintained in the SQUID sensor, it develops a voltage across the junctions. The magnetic flux passing through the loop enhances the current in one junction and reduces it in the other, which causes the voltage across the junction to oscillate [173]. When an external magnetic flux is coupled into the loop, the voltage changes in a periodic manner that corresponds to an increase of one flux quantum. By measuring the change in voltage it is possible to determine the magnetic flux of the material coupled to the SQUID [174].

The measuring process in the SQUID is very similar to the one in VSM. The sample is put inside a straw and moved vertically along a set of three superconducting pick-up coils and subjected to a uniform magnetic field [175]. The coils are connected by a single piece of superconducting wire and are only sensitive to the magnetic fields of the sample, eliminating any contribution from external fields. The coils, the wire and the squid create a superconducting loop. Any change in the magnetic flux will produce a proportional change in the persistent current of the coils, consequently producing variations in the SQUID output voltage [175]. The output signal is then transformed into electronic signals, thus allowing the extraction of the magnetic properties of the material [176]. This process is illustrated in figure 22B.
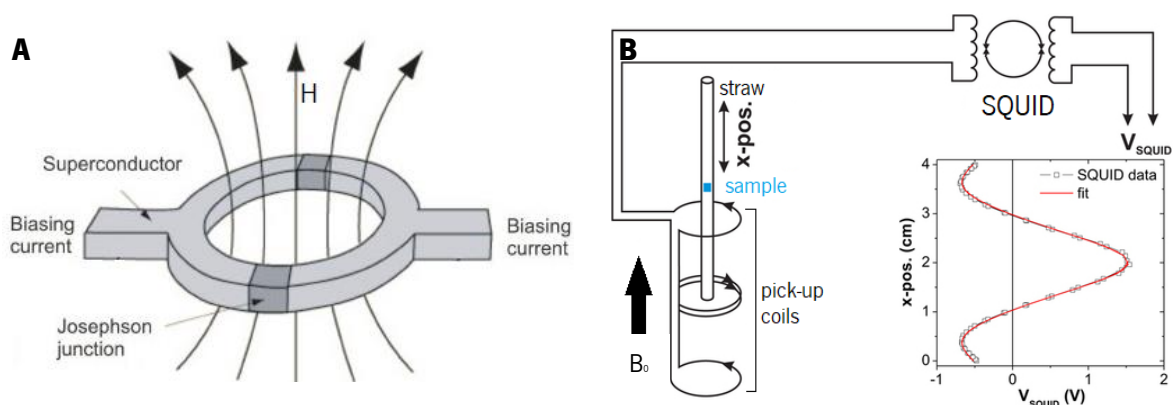
Figure 22 - A: dual Josephson junction of a SQUID device; B: schematic setup of a SQUID magnetometer and an inset showing the squid response in voltage versus the sample position. Adapted from [172] and [174].

This equipment has a more intense and homogeneous magnetic field than other magnetometers in the market, being able to detect incredibly small magnetic fields with high precision. Some equipment can incorporate a vibrating sample measurement (VSM) mechanism, similar to the one used in the VSM previously mentioned. The SQUID allows to take measurements of the magnetization at different temperatures, which is important to determinate magnetic behaviours and phase transitions.

2.6.   X-ray diffraction

X-ray diffraction (XRD) is a non-destructive analytical technique widely used to characterise crystalline materials [177]. In a crystal the atoms are distributed in planes presenting periodic repetition. XRD is based in the elastic scattering of X-ray photons by atoms in a periodic lattice, used to determine the crystalline phases, orientation, average spacing between rows of atoms, grain size and shape among other [178]. The X-rays are able to pass through the crystalline surface originating different reflections from the different atom planes. Given the periodic spacing between planes, the scattered monochromatic X-rays cancel each other in most directions (destructive interference), but also combine themselves generating a constructive interference, this phenomenon is called X-ray diffraction. The constructive interference happens when the angle between the plane and incident radiation results in a difference in the optic path travelled by the beams (figure 23) [178]–[180]. This process only happens when conditions satisfy Bragg's law. Bragg's law (11) explains the relationship between the incident X-rays and their diffraction off from the crystal surface:

$$2\,d\sin\theta = n\lambda \tag{11}$$

where d is the spacing between the crystal planes, θ is the angle between the incident and the diffracted beams, n is the diffraction order and λ is the wavelength of the X-rays [177], [180].
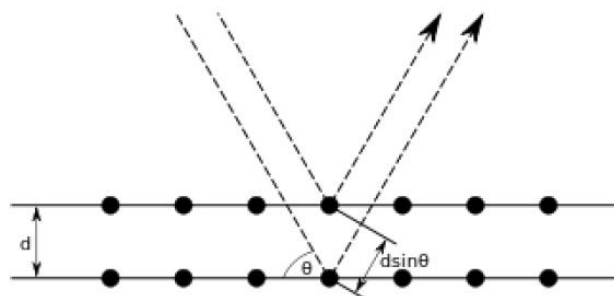
Figure 23 - Schematic representation of Bragg model [177].

The equipment required for this analysis is an X-ray diffractometer, figure 24 shows a simplified representation of its functioning. Briefly, the X-rays are generated in an X-ray tube by heating a filament (cathode) that produces electrons. By applying a voltage these electrons are accelerated in the direction of an anode, normally made of copper, containing a metallic plaque (target). The accelerated electrons

remove the inner shell electrons of the target metal and the electrons from the outer shells fill in the vacancies, which results in the generation of X-rays [177]. These X-rays are filtered to produce monochromatic radiation, collimated and directed towards the sample. The diffracted X-rays are detected by an X-ray detector, processed, counted and then traduced to an X-ray spectra [177]. The geometry of an X-ray diffractometer is very important to satisfy Bragg's law. The sample rotates in the path of the incident beam at an angle of θ, while the detector is mounted in a way that the X-rays are collected at an angle of 2θ. To maintain these angles and rotate the sample, the equipment processes a sample holder or goniometer [177].
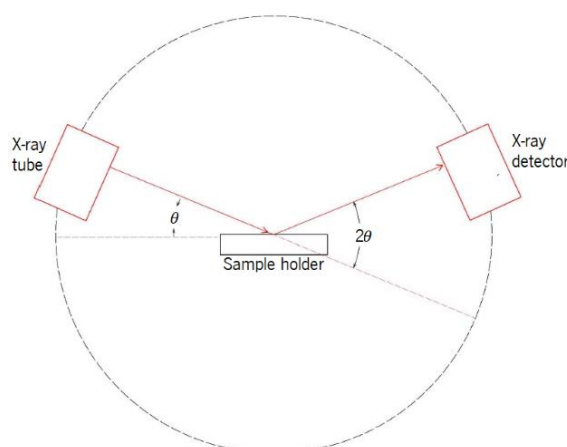
Figure 24 - Schematic representation of the functioning of an XRD.

2.7.   High-Performance Liquid Chromatography

High-performance liquid chromatography (HPLC) is a separation technique widely used in analytical chemistry, to separate and analyse compounds in a mixture. The separation involves a passing mixture dissolved in a mobile phase, that runs off in a defined direction through another material, called stationary phase [181], [182]. In HPLC technique the stationary phase consists of porous spherical particles present on a column, through which the mobile phase passes continuously at a high pressure with controlled flux [181]. This allows a faster and more efficient analysis. Usually, analytes have different interactions with the mobile and stationary phase. The analytes that have stronger interactions with the stationary phase will tend to move slower than the analytes that have weaker or no interactions with this phase, this process is called elution [181], [182]. The strength of analytes interaction with both phases its determinant for the chromatographic separation.

Figure 25 illustrates the process of a HPLC measurement that operates in a closed circuit. The main components of a HPLC are: solvent delivery systems, where the solvent or mobile phase reservoir and the high pressure pump are included; the sample injector; a column (stationary phase), normally made

of stainless steel; a detection system, that may have UV and fluorescence detectors; and a computer data station [181].
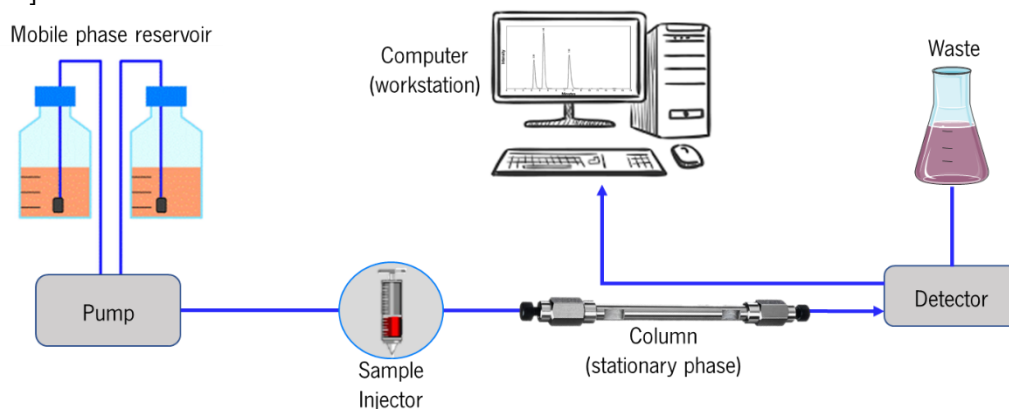
Figure 25 - Schematic representation of the process of a HPLC instrument.

Briefly, one or more solvents are kept in a glass reservoir and a pump delivers the solvent mixture through the whole chromatograph at high pressure, at a broad range of flow rate with no flow fluctuations, guaranteeing the reproducibility of the process. The sample injection system is responsible for introducing the liquid sample into the flow stream of the mobile phase. In analytical HPLC, it is important to work with small injection volumes, this way it is easier to ensure that volume taken is always the same, avoiding peak deformations or double peaks [181]. Most instruments already operate in an automatic manner (autosampler), allowing the programming of continuous automatic injections of the samples [182]. Then the analytes of the sample are transported through a column, that is constituted by a specific packing material, the stationary phase, that is composed of little porous particles which can withstand extremely high pressures [181], [182]. The separation column is normally maintained at room temperature, but it can be cooled or heated in most equipment. After passing through the column the eluting sample reaches the detector, which emits a response generated by the analytes. It is important to choose a suitable detector, depending on the physical and chemical properties of the components of the sample. In a computer workstation the detected signals are turned into peaks and presented on a chromatogram [181].

2.8. Magnetic Resonance imaging

The basic principles of MRI were discussed in chapter 1, in this section a more detailed description of the MR scanner functioning will be described.

MRI is a technique widely used in clinic to form pictures of the anatomy and physiological characteristics of the body, producing reliable diagnoses. MRI scanners use strong magnetic fields to measure the spatial distribution of nuclear proton spins in the body, by using the precessional motion of the proton spins after they are excited by RF pulses [107]. This machine can provide high spatial

resolution images with intense contrast that facilitates the visualization of diseases in animal tissues [183].

Figure 26 shows a schematic representation of a typical MRI scanner. Briefly, a patient or in this case a sample, is positioned within the scanner bore. A superconducting or permanent magnet creates a stable, strong and spatially uniform external magnetic field, that causes the hydrogen ions in the body to align with this field [184]. Then, an electromagnetic field is switched on and off by gradient coils, at an appropriate resonance frequency, causing the selected atoms to alter their
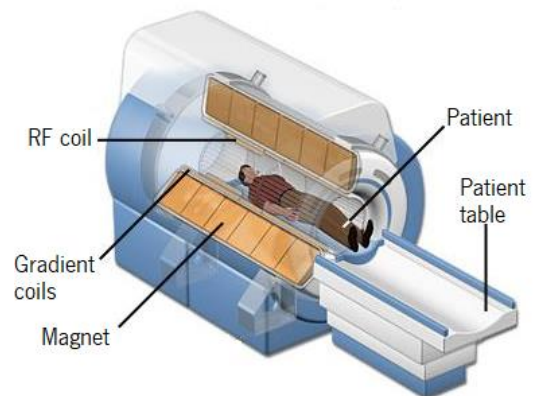
Figure 26 - Schematic representation of a MRI scanner. Adapted from [182].

alignment and switch back to their original relaxed state when the field is off [184]. Gradient coils (x, y and z) are able to encode position information from the MR signal by varying the main magnetic field in all directions. When a current pass through these coils a gradient is created in the main magnetic field. This gradient disturbs the main field, causing the resonance frequency of protons to vary in function of their position [185]. The RF coils are able to excite the sample and detect the resulting NMR signal coming from the excited atoms [185]. The detected signal is then transformed by Fourier Transform, amplified and presented in a computer.

In this equipment the images can be acquired with different sets of pulse sequences and gradients that will result in a different image appearance. The most common sequences are the spin echo (SE) with proton density (PD), T_1 and T_2 weighted images. A spin echo is produced by pairs of RF pulses at any angle. Regardless, two RF pulses at different angles are the most used: one at 90° to excite the magnetization, and another one at 180° to rephase the spins, causing them to gain coherence and generate the spin echoes, that on this particular case can be referred to as Hahn echo [186], [187]. The time between the first pulse and the peak of the generated spin echo is called echo time (TE) and the length of time between successive pulse sequences applied to the same slice is called repetition time (TR), both measured in milliseconds (ms) (figure 27) [187], [188]. An inversion time (TI) can also be defined for an Inversion recovery (IR) pulse sequence, that consists in a conventional SE sequence preceded by a 180° inverted pulse. The TI can be defined by the time between the first 180° inverting pulse and the 90° pulse from SE sequence, during this time the proton spins restore their equilibrium through a T_1 recovery [189].
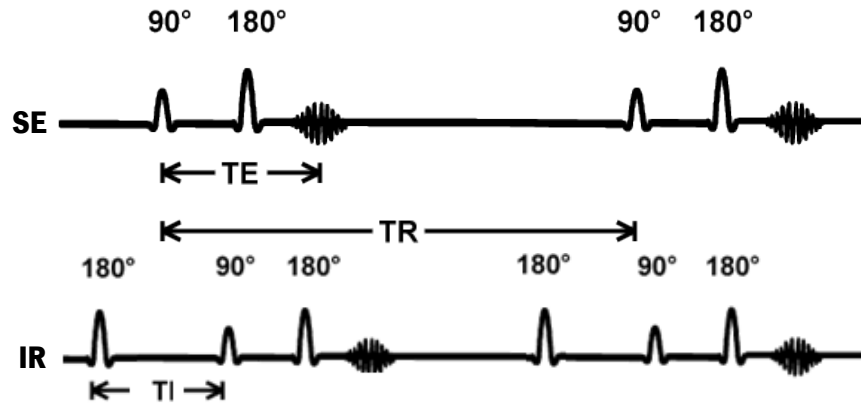
By varying the TR and TE is possible to control image contrast and the weighting of an MR image. For T_1 weighted images short TR and short TE times are used; for T_2 weighted images long TR and long TE times are used; and for PD (proton density) weighted images long TR and short TE times are used [188]. Depending on the desired end different times can be defined, and different sequences can be used being also possible the combination of two or more different sequences [190]. This equipment is also capable of acquiring T_1 and T_2 maps, which are a combination of several T_1 or T_2 weighted slices of the subject acquired at different TI or TE times respectively, that altogether forms a stack from which it is possible to extrapolate relaxivity values.

2.9.   Magnetic Hyperthermia

The basic principles of MHT were discussed in chapter 1, in this section an overview of this technique will be addressed.

MHT has been increasingly researched recently, and due to its promising results it is already being used in the clinic [106]. In this technique the heating of biological tissues is supplied by the oscillations of the MNPs induced by an external AMF [191]. As previously mentioned iron oxide NPs are the most used nanoheaters nowadays, and their hyperthermia effectiveness depends on their magnetic, colloidal and structural properties, but also on the technical parameters of the MHT equipment like frequency and field intensity [106], [191].

In most MHT equipments the frequency and the magnitude of the external magnetic field can be selected by the user. For safety considerations, the selected parameters need to fulfill the following condition, for an 1 hour treatment (12):

$$Hv < 4.85 \times 10^8 A/m \text{ s} \tag{12}$$

where H is the magnetic field amplitude and v is the frequency of the AMF [106]. Briefly, an alternated currents passes through a water-cooled induction coil and a function generator generates a square wave function at a selected frequency. This process will generate a non uniform magnetic field, where its distribuition and intensity are heavily dependent on the geometry of the coil (figure 28) [192]. Therefore, the sample is placed at the centre of the coil, where the maximum amplitude of the AMF is achieved. A temperature sensor (fiber optic-based) connected to a computer is used to record the temperature increase as a function of time.
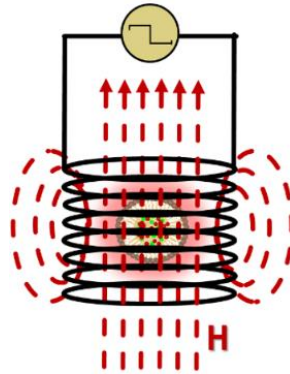
Figure 28 - Scheme of a MHT setup. At the centre of the coil a MNP as nanoheater. At the top, a square wave function for frequency selection. H, magnetic field.

MHT systems can be mounted on the laboratory according to the users goal, presenting interchangeble parts for selecting the frequency and intensity of the AMF and different coil configurations. Most of these systems exhibit exposed coils that can put at risk the repeatability of an experiment, but they present a great advantage since their configuration can be exchanged which gives access to different types of experiments with the same equipment. Figure 29 shows a schematic representation of this kind of equipment set up for *in vitro* experiments.
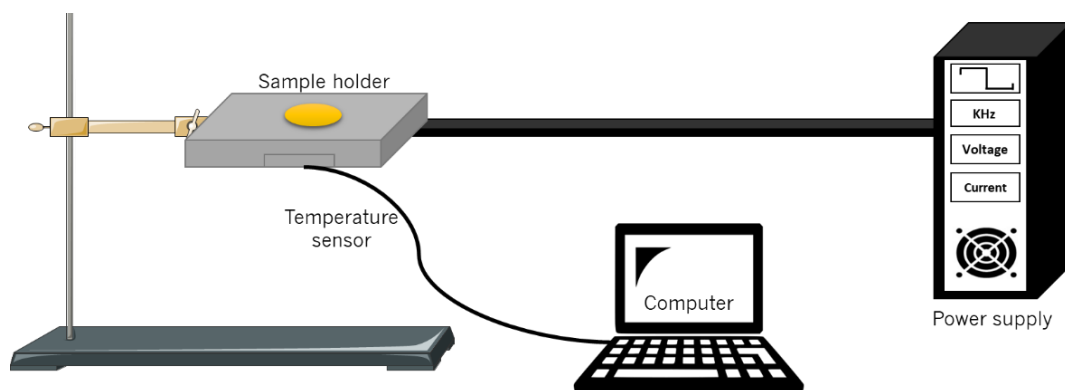
Figure 29 - Schematic representation of a MHT equipment set up for in vitro experiments.

There are also equipments with all the interparts already set up, like the DM100 series from nanoScale Biomagnetics, where it is possible to choose from a wide range of frequencies and field intensities with a maximum intensity up to 20 mT. In this case the coils are protected in the interior of the MHT apllicator, improving its safety and avoiding contaminations. In this equiment the sample holder

is fixed in the center of the coil as shown in figure 30, providing a good thermal isolation that diminishes the loss of heat generated by the sample and avoid interferencial heatings from the electronics. This configuration ensures experiment repeatibility and the validity of the field readings. The temperature sensors in this equipment are incorporated in the sample holder [192]. This particular configuration is the most reliable to calculate the SAR of magnetic colloids, but it is less versatile for other *in vitro/ in vivo* experiments.
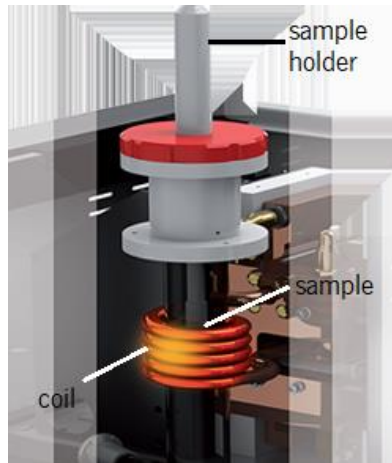
Figure 30 - Schematic representation of a MHT applicator ideal for calorimetric studies. Adapted from [190].

CHAPTER 3 - MATERIALS AND METHODS

3.1. Materials

In this section, all the materials used for the development of this project, from equipment to chemicals, will be listed in table 2.

Table 2 - List of all equipment, materials, software and reagents used throughout the course of this project.

Equipment	- Centrifuge miniSpin - eppendorf; - Centrifuge UNIVERSAL 320 – Hettich zentrifugen; - Compact Spectrofluorometer - FluoroMax-4 – Horiba Scientific; - Confocal microscope– LSM780 on inverted Axio Observer - Zeiss; - Digital Sonifier® - Branson Ultrasonics Corporation; - Dynamic Light Scattering – Zeta potential - SZ-100Z – Horiba Scientific; - Fluorescence plate reader (Biotek, model: SYNERGY H1); - Fourier Transform Infrared Spectroscopy – Vertex 80v – Bruker; - High Performance Liquid Chromatography – 1290 Infinity – Agilent Technologies; - Inductive Plasma Atomic Emission Spectrometer - ICPE 9000 - SHIMADZU; - Inverted microscope - Eclipse TS100 with a digital sight DSFi1 camera – Nikon; - Magnetic Hyperthermia applicator – Magnetherm version 1.5; - Magnetic Hyperthermia equipment – DM1 - nanoScale Biomagnetics; - MR solutions 3.0 Tesla benchtop magnetic resonance imaging system; - Precision balance – ABT 120-5DM – KERN; - Superconducting Quantum Interference Device – Vibrating Sample Measurement – MPMS - Quantum Design - Thermogravimetric Analyser – TGA/DSC 1/1100 SF STARe System - Mettler Toledo; - Transmission Electron Microscope – JEOL JEM 2100 200 kV (Cryo & Tomography); - Ultra-sound – Elmasonic P - Elma; - UV-Vis SpectroPhotoMeter - UV-2550 – SHIMADZU corporation; - Vibrating-sample magnetometer – model 3473-70 electromagnet - GMW magnet systems; - Vortex – VV3 - VWR; - X-Ray Diffraction System – X PERT PRO MRD – PANalytical
Software	- Image J (Fiji); - Microsoft Office 365; - Origin 9.0; - Paint 3D; - Zen 3.0 (Blue edition)
Materials	- Filters (30000 Da) – Millipore; - Pur-a-lyzer (60000 Da) – Sigma Aldrich; - Custom printed MRI holder; - Carbon coated copper grids, 400 mesh – Ted Pella,Inc. - CELLView™ dish with 4 compartments and glass bottom – Greiner Bio-One; - 24 well plates; - 96 well plates;
Reagents/solutions	- AlexaFluor 647 (Invitrogen)

	- Ammonium hydroxide (Sigma-Aldrich);
	- anti-α-tubulin antibody (Sigma-Aldrich)
	- Aquabluer (MultiTarget Pharmaceuticals, LLC);
	- *Carnauba Wax* (Koster Keunen Holland BV);
	- Chloroform (analytical grade or better: Sigma-Aldrich);
	- DAPI (4',6'-diamino-2-fenil-indol) (Sigma-Aldrich)
	- DiO (3,3'-Dioctadecyloxacarbocyanine Perchlorate)(Iris Biotech);
	- Doxorrubicin (Adooq Bioscience);
	- Dulbecco's modified Eagle's medium (DMEM);
	- Fetal bovine serum (FBS);
	- Hexane (analytical grade or better: Sigma-Aldrich);
	- Iron(II) chloride tetrahydrate (Sigma-Aldrich);
	- Iron(III) chloride hexahydrate (Sigma-Aldrich);
	- Milli-Q water (ultra-pure);
	- Oleic Acid ≥99% (Sigma-Aldrich);
	- Penicillin-Streptomycin;
	- Phospate-buffered saline (PBS, ph - 7.4), (Sigma-Aldrich);
	- Potassium Permanganate (Sigma-Aldrich);
	- Shandon Immu-mount mounting media (Thermo Scientific);
	- Tween 80 (Sigma-Aldrich);

3.2.   Methods

In this section the methods used for the synthesis and characterisation of NPs are described. The procedures done for the drug studies and *in vitro* experiments are also described.

3.2.1. Synthesis of superparamagnetic iron oxide nanoparticles (SPIONs)

Hydrophobic nanoparticles of magnetite (Fe_3O_4@OA) were prepared by coprecipitation method adapted from [193]. Briefly, 9.2 g of iron(II) chloride tetrahydrate and 15 g of iron(III) chloride hexahydrate were dissolved in 250 mL of mili-Q water and stirred for 10 min at 50 °C. After 10 min, 30 mL of ammonium hydroxide, NH_4OH (12 mol/L), were added starting this way the coprecipitation that resulted in a dark precipitate of Fe_3O_4. Then 2.5 mL of oleic acid (OA) were added and the mixture was heated at 80 °C for 1 h. The excess of NH_4OH and OA was removed by magnetic separation of Fe_3O_4@OA with the use of a magnet, followed by the decantation of the supernatant and the redispersion of the solid in fresh solvent. The washing procedure was repeated five times with milli-Q water and four times with hexane. Finally, the Fe_3O_4@OA NPs were dried, dispersed in chloroform and stored in the fridge [194]. Figure 31 illustrates this procedure.
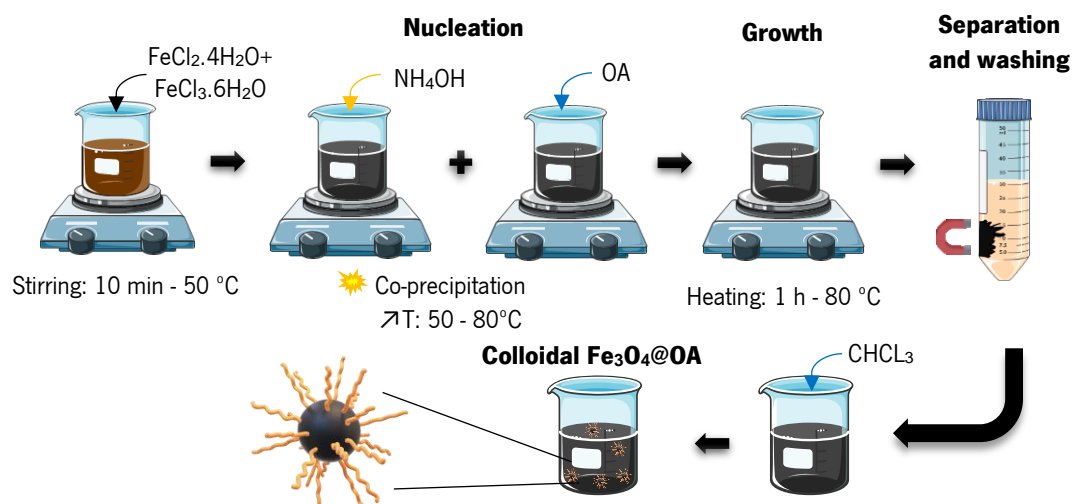
Figure 31 - Illustration of the coprecipitation method, used for the synthesis of Fe₃O₄@OA NPs.

3.2.2. Synthesis of manganese oxide nanoparticles

Hydrophobic manganese oxide (MnO@OA) nanoparticles were prepared according to [195]. The procedure is illustrated in figure 32. For the preparation, 0.5 g of potassium permanganate ($KMnO_4$) were dissolved in 250 mL of Milli-Q water and left stirring for about 30 mins. A total of 5 mL of OA were added and the sample was left stirring, at room temperature, for 24 h. The next day there was a brown 'solid' floating on a colourless solution, this solution was decanted and the solid washed twice with mili-Q water. After this, ethanol (EtOH) was added to remove any possible residue reactants. At this point the solid was resuspended in the solvent, transferred to falcon tubes and centrifuged for 5 min at 8500 rpm. The supernatant was once more discarded and the pellet resuspended in hexane, resulting in a dark-brown solution that was stored in the fridge until further use.
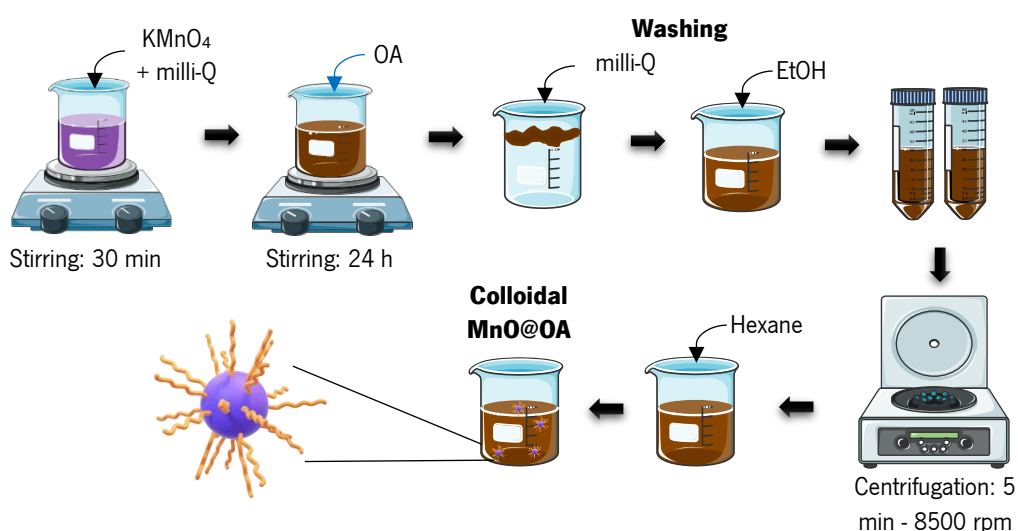
Figure 32 - Illustration of the procedures used for the synthesis of MnO@OA NPs.

3.2.3. Synthesis of manganese dioxide nanoparticles

A sonochemical method was used for the preparation of manganese dioxide nanostructures (MnO$_2$@Glc), based on the mild reduction of MnO$_4$ by glucose (Glc) (figure 33) [5]. In a typical synthesis, 0.057 g of Glc were dissolved in 30 mL of mili-Q water. Then 0.25 g of KMnO$_4$ were added and the purple solution was immediately sonicated for 20 min at 25% power, with a 10 mm tip in a digital sonifier. Then, for the purification of the samples, the solutions were centrifuged at 8500 rpm for 15 min, the supernatant was discarded and the pellet re-suspended in 40 mL of water. This process was repeated 2 more times and finally the pellet was resuspended in 30 mL of water. This solution was then centrifuged for 3 min at 3000 rpm to remove large aggregates. This time the supernatant was kept and stored until further use.
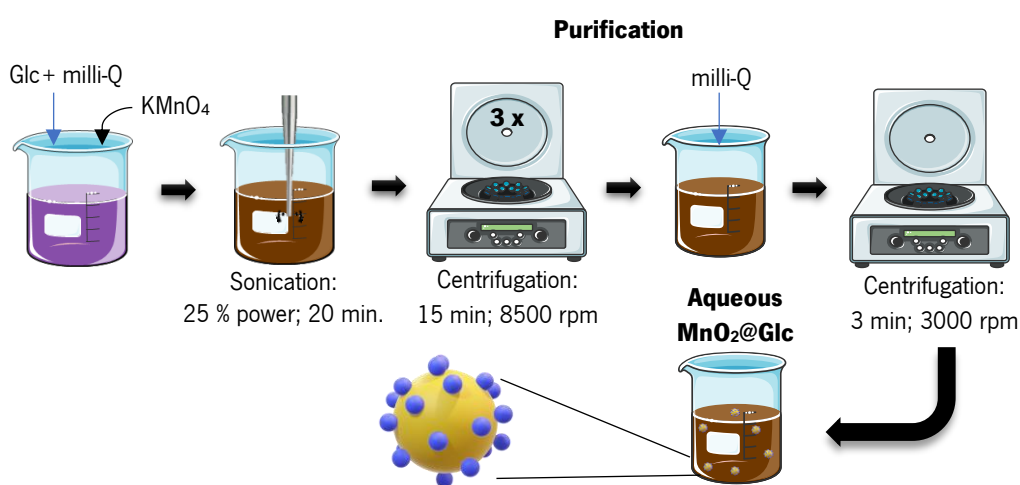
Figure 33 - Illustration of the sonochemical method, used for the synthesis of MnO₂@Glc NPs.

3.2.4. Synthesis of solid lipid nanocarriers

Throughout the development of this work non-magnetic and magnetic SLNs (mSLNs) were synthetized. All the nanoparticles presented are made of a surfactant, Tween 80 that is approved by the FDA; a solid lipid matrix made of the biocompatible carnauba wax; and DiO, a green fluorescent lipophilic carbocyanine, useful to trace the NPs in cells. The mSLNs can contain Fe$_3$O$_4$, MnO and MnO$_2$ combined in different ways. The final NPs comprise a (para)magnetic core and a chemotherapeutic drug, doxorubicin. A general procedure for the mSLNs will be explained, the details about each formulation can be found in table 2.

A modified melt-emulsification method was used for the preparation of SLNs (figure 34). Initially, 200 mg of carnauba wax were mixed in a glass vial with a colloidal solution of MNPs, 0.25 mL of a chloroform solution of DiO (1 mg/mL), added only in final formulations, and dox. This mixture was then placed in the digital sonifier. At this point, 4.5 mL of Milli-Q water and 0.5 mL of a water solution of Tween 80 (50 mg/ml) were added to the vial and the sample was ultrasonicated with a 3 mm tip, for 2 min, at 25%

power, at 20 second working intervals, while being simultaneously heated with a heat gun. Immediately after the sonication, the sample was immersed in ice to solidify the lipid NPs. Once cold, the formulation was centrifuged for 10 min, at 3000 RPM to remove big wax aggregates, the supernatant was stored in a glass vial and the pellet was discarded.
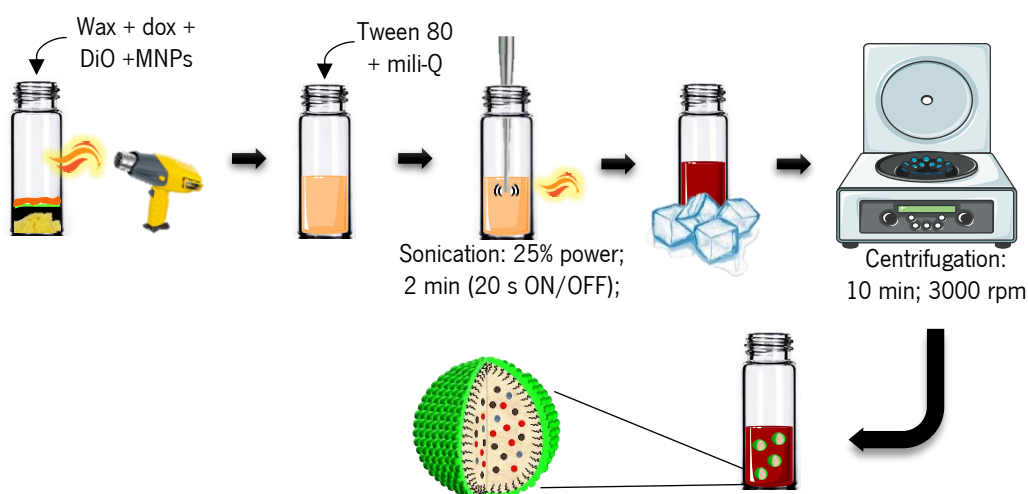
Figure 34 - Illustration of the modified melt-emulsification method used for the synthesis of mSLNs.

Prior to the synthesis of our final SLNs, containing SPIONs, MnO and dox (SLN@Fe$_3$O$_4$-MnO-dox), several intermediary experiments were made along the way. First, it was necessary to test if the drug and the different MNPs could be efficiently encapsulated into the SLN's alone (SLN@dox, SLN@Fe$_3$O$_4$, SLN@MnO, SLN@MnO$_2$) and once they were, the following procedure was to encapsulate both magnetic and paramagnetic particles (SLN@Fe$_3$O$_4$-MnO, SLN@Fe$_3$O$_4$-MnO$_2$). Table 3 shows the theoretical percentage of each compound that was used, in relation to the quantity of Carnauba wax.

Table 3 - Percentage of dox and MNPs present in the SLNs.

Formulation	dox (%)	Fe$_3$O$_4$ (%)	MnO (%)	MnO$_2$ (%)
SLN@dox	20	-	-	-
SLN@ Fe$_3$O$_4$	-	30	-	-
SLN@ Fe$_3$O$_4$–dox	20	5	-	-
SLN@MnO$_2$	-	-	-	10
SLN@ Fe$_3$O$_4$–MnO$_2$-dox	10	5	-	20
SLN@MnO	-	-	22	-
SLN@ Fe$_3$O$_4$–MnO	-	10	20	-
SLN@Fe$_3$O$_4$–MnO–dox	20	10	20	-

49

3.2.5. Physico-chemical characterisation techniques

3.2.5.1. DLS

To measure the average size, PI and the zeta potential of the SLNs a Dynamic Light Scattering – Zeta potential, SZ-100Z equipment from Horiba Scientific with nanometric resolution (from 0.3 nm to 8 µm) was used. For all the measurements an electrode cell was used. For all the measurements 1 mL of sample was used, with a dilution of 1:100, since it was the ratio at which the lowest PI values could be obtained.

For the DLS and ELS measurements for the SLNs containing both MnO and Fe_3O_4, only the refractive index of magnetite was used. For the SLNs containing either of those components it was used their respective refractive index. For the SLNs without MNPs a generic organic sample refractive index was used. All the samples were measured at 25°C, 3 to 5 times, with a stabilization time of 90 seconds, being that the final values presented are the mean of all the measurements. For the size only the "mean average" of the peak was considered, and for the zeta only the ''mean zeta'' value. The parameters used for the measurement of the size and zeta potential are listed in table 4.

Table 4 - Parameters used to measure the size and zeta potential of the NPs.

Cell	- Electrode cell: carbon, 6mm
Detector angle	- 173°
Sample - **Dilution** - **Refractive index**	- 1:100 - Magnetite: 1.900 – 1.700i - Manganese: 2.170 – 0.000i - Organic samples: 1.600 – 0.000i
Dispersion medium - **Refractive Index** - **Temperature** - **Viscosity**	Water - 1.333 - 25 °C - 0.88 cP

3.2.5.2. UV-Vis absorption spectroscopy

For the UV-Vis spectrum acquisition an UV-Vis SpectroPhotoMeter - UV-2550 from SHIMADZU corporation, with a spectral range from 190 to 1100 nm was used. The samples were highly diluted in water or hexane, so the references used were either water or hexane. These measurements were made only for manganese NPs and SLNs containing manganese, since this material presents a known peak in the UV-Vis spectrum. This way, by analysing the spectra obtained, it was possible to identify the presence

of manganese in the samples analysed. The wavelength range used for these measurements was from 300 to 800 nm, the slit aperture was 5 nm and the cells used were quartz cells.

3.2.5.3. Fluorescence spectroscopy

The acquisition of fluorescence spectra was made with a Compact Spectrofluorometer, FluoroMax-4 from Horiba Scientific. This technique was used to analyse the samples of SLNs containing dox, to confirm the presence of the drug, since it is a fluorescent drug with an emission peak around 590 nm. The emission spectra of DiO, a fluorescent dye with an emission at around 506 nm, was also recorded. The spectra were acquired from 500 to 700 nm, using 5 nm entrance and exit slits, with λ_{ex} of 480 nm for dox, and 489 nm for DiO. Both these wavelengths are very close to each other, making it difficult to read the spectra. For the spectra acquisition the samples were highly diluted, and a four opening disposable cell was used.

3.2.5.4. FT-IR

For the spectra acquisition a FT-IR - Vertex 80v from Bruker was used (figure 35A). This system is equipped to perform in the middle infrared (MIR) and far infrared (FIR) ranges. For that effect a MIR source, made of silicon carbide is installed inside the equipment, and a FIR source, a water-cooled mercury lamp, is installed externally. The spectrophotometer is also equipped with a transmittance and an ATR (attenuated total reflectance) accessories, shown in figure 35B and 35C respectively. The operation mode used in this work was the MIR-ATR mode. The detector used was a very sensitive MCT (Mercury-Cadmium-Telluride) detector, cooled with liquid nitrogen.
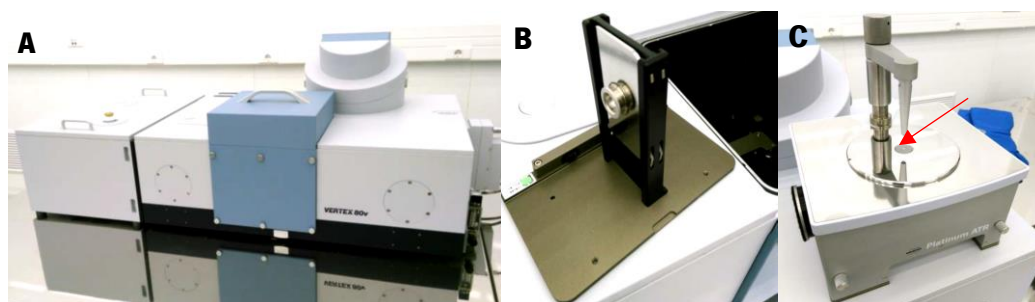
Figure 35 - A: Vertex 80v FT-IR system; B: accessory for the transmittance operation; C: accessory for ATR operation mode.

This technique was used to obtain information about the functional groups present in the SLNs and their constituents (Tween 80, Carnauba wax and MNPs) and compare their spectra. For sample preparation 500 µL of the MNPs and the SLNs were dried in the vacuum and put directly in the ATR. The Tween 80 and C. wax did not need any preparation. After a background acquisition, the sample is put in the diamond present in the ATR accessory, which has a higher refraction index than the sample, and is

then submitted to vacuum and the measurements are taken. It is to note that the FT-IR is a relative technique and the simple observation of its spectra is necessary, but not a sufficient condition to determine the presence of functional groups.

3.2.5.5. ICP-AES

For the ICP-AES measurements standard solutions with predefined well-knonw concentrations of the elements to be analysed (Fe and Mn) needed to be prepared. This allows to stablish a calibration curve for each element, that would be used by the system to calculate the metals concentration. For the iron, the solutions prepared ranged from 0 to 10 ppm and for the manganese, the standards ranged from 0 to 0.5 ppm. For sample preparation 5 or 10 µL of MNPs or 100 µL of SLNs were pipetted into a 15 mL falcon together with 1 mL of hydrochloric acid and left to react overnight. Before the analysis 9 mL of mili-Q water were added to the falcon and placed in the carousel of the equipment to measure. To analyse the concentration of iron and manganese the emission wavelengths used were 235 nm and 257 nm, respectively.

3.2.5.6. TEM/ STEM-EDX

For the development of this project a TEM, JEOL JEM-2100-HT (Cryo & Tomography), with an accelerating voltage between 80 kV and 200 kV and a resolution of 0.24 nm was used. This instrument is equipped with a high brightness LaB_6 (lanthanum hexaboride) electron gun and a fast-readout OneView 4k x 4k CCD camera. The JEOL allows not only TEM, but also STEM with a resolution of >1.5 nm. It also has an EDX from Oxford Instruments, with a solid angle of 0.13 and a hard X-ray aperture for elemental analysis.

This equipment was used to analyse the morphology of the synthetized MNPs and SLNs. Its major use was for the SLNs, to verify if the MNPs were efficiently encapsulated. When it was not possible to visualize the MNPs encapsulated, namely the case of MnO_2, a STEM-EDX analysis was performed. This technique enabled the localization of MnO_2 particles within the SLNs, through the elemental mapping of the sample.

For sample preparation the samples were highly diluted into the respective solvents, and then 7 µL of these dilutions were loaded into carbon coated copper grids with 400 mesh (squares across the grid) from Ted Pella Inc., represented in figure 36, and dried in the vacuum [196]. In the microscope the sample was loaded with a single tilt holder,
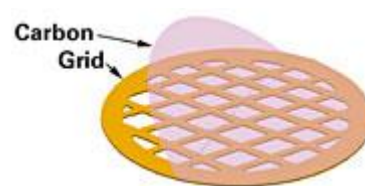
Figure 36 - Schematic representation of a carbon copper grid from Ted Pella [194].

and the accelerating voltage was set at 200 kV, for both TEM and STEM-EDX analysis. STEM-EDX analysis were performed with BF contrast.

The images were analysed and treated using Image J (Fiji) software, mainly for NPs measurements, brightness and contrast corrections.

3.2.5.7. TGA

For this work a TGA/DSC 1, 1100 SF, STARe system from Mettler Toledo was used. For this analysis no sample preparation was needed, 50 µL of the liquid samples were loaded directly into the sample pan (figure 37) and its weight registered. The analysis was performed under a nitrogen atmosphere. In the case of the SLNs the method used consisted in a temperature increase from 25 to 900 °C at 10°C/min, with an approximately 30 min stop at 120 °C to assure that all the

Figure 37 - TGA sample pan [163].

water had evaporated. In the case of the SPIONs the method consisted in a temperature increase from 25 to 900 °C at 5°C/min, with a 10 min stop at 60 °C to make sure that the $CHCl_3$ had evaporated.

3.2.5.8. VSM

To magnetically characterise MnO and MnO_2 NPs a VSM 3473-70 electromagnet with a coil gap of 127 mm, from GMW was used. For sample preparation, 500 µL of sample were dried in the vacuum and then loaded into a gelatin capsule. The sample was weighted and fixed with cotton and placed in a glass straw that is the sample holder (figure 38A). Then the sample was carefully placed in the equipment, between the two electromagnets and the measurement was started (figure 38B). For these measurements a magnetic field of $\pm$ 2 T was applied.
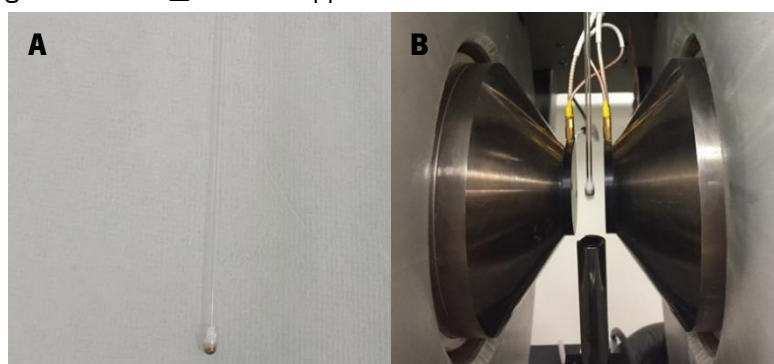
Figure 38 - A: sample holder and sample for VSM; B: sample placed in the VSM equipment.

3.2.5.9. SQUID

To magnetically characterise SLNs a SQUID-VSM, MPMS magnetometer from Quantum Design was used. This equipment combines the SQUID technology with a vibrating sample measurement, also used in the VSM equipment. For sample preparation, 500 µL of sample were dried in the vacuum and then

loaded into a gelatin capsule (figure 39A). The sample was weighted and fixed with cotton and then placed in a straw that was attached to a measuring rod and placed inside the equipment (blue arrow, figure 39B). For the magnetization measurements the samples were submitted to a magnetic field of 100 Oe at 5 K and 300 K.
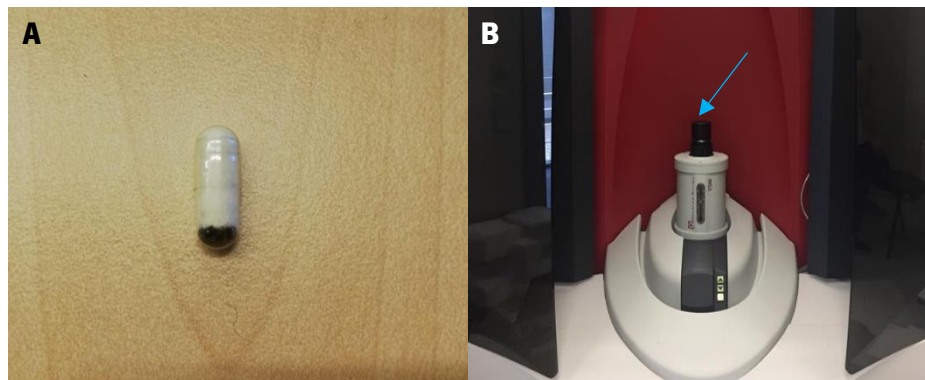
Figure 39 - A: sample for SQUID-VSM; B: SQUID-VSM equipment, blue arrow indicates the place through which the sample is loaded.

3.2.5.10. XRD

An X-Ray Diffraction System, X'Pert PRO MRD from PANalytical with a copper X-ray tube (CuKα) in a Bragg Brentano configuration was used to identify the samples crystallographic structure. In the case of magnetite NPs the sample was directly loaded into the sample holder, until it covered the entire circumference of the holder, and dried in the vacuum. For MnO and MnO_2 NPs, the sample was first dried in the vacuum, and then loaded into the sample holder, being more difficult to cover the entire circumference of the holder.

3.2.5.11. MRI

A MR Solutions 3,0 Tesla benchtop MRI system was used to evaluate the efficiency of prepared formulations as MRI CAs. This equipment has variable field strengths of 1,5 and 3,0 T. It presents high spatial resolution and superior field homogeneity [197]. Only T_1 and T_2 maps were studied in this work. The evaluated formulations were: SLN@MnO, SLN@MnO₂, SLN@Fe₃O₄ (with and without dox), SLN@MnO-Fe₃O₄, SLN@MnO-Fe₃O₄-dox and SLN@MnO₂-Fe₃O₄-dox. All the samples were measured at a magnetic field of 3.0 T and room temperature.

For sample preparation the samples containing MnO_2 were separately diluted in water and hydrogen peroxide (H_2O_2, 10 mM), to evaluate their responsiveness to redox conditions. If when in H_2O_2 the particles exhibit lower relaxation times, this

Table 5 - Element concentrations used for the MRI studies for each formulation.

Formulation	[Mn] (mMolar)	[Fe] (mMolar)
SLN@MnO₂	0,08 – 0,2	–
SLN@MnO₂-Fe₃O₄-dox	0,05 – 0,12	0,06 – 0,17
SLN@MnO	0,08 – 0,43	–
SLN@Fe₃O₄-dox	–	0.01 – 0.075
SLN@MnO-Fe₃O₄-dox	0,002 – 0,025	0,01 – 0,13

would be indicative of responsive, oxygen generating particles. Therefore, the relaxivity values are expected to be higher in H_2O_2. All the remaining formulations were diluted in water. The concentrations of iron and manganese used for each formulation are summarized in table 5.

After sample preparation, 300 µL of each sample dilution were loaded into a custom printed MRI holder, ranging from the least concentrated to the highest, as shown in figure 40A by the blue arrow. The spaces with no sample were filled with water for reference. Then the holder was positioned in the centre of the MRI scanner bore, shown in figure 40B by the red arrow, and a SCOUT acquisition was made to verify the correct positioning of the sample. Afterwards, the T_1 and T_2 maps were acquired using MPRAGE (magnetization prepared rapid gradient echo) and MEMS (multi-echo multi-slice) sequences respectively, and their characteristics are presented in table 6. Image J (Fiji) software was used to reconstruct the maps using the "MRI analysis calculator" plugin by Karl Schmidt, and to determinate the relaxation times for each sample concentration. The relaxivity values were extrapolated from the slope of the graph of relaxation rate versus ion concentration.
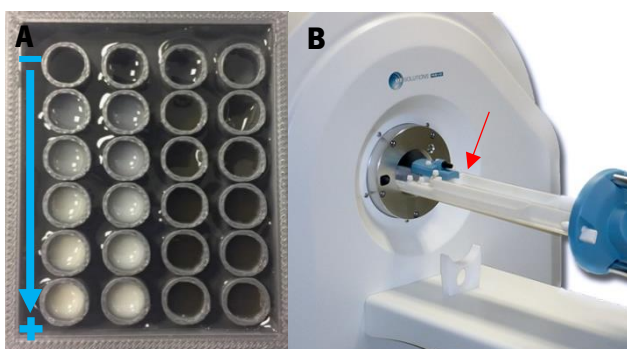
Figure 40 - A: costume printed sample holder loaded with samples, the blue arrow indicates the increase in sample concentration; B: MRI equipment, red arrow shows the place in which the sample holder is positioned.

Table 6 - MRI specifications for T_1 and T_2 maps acquisition.

	T1 map	T2 map
Nº echoes	11	10
TR (ms)	10000	1400
TE (s)	5	0.015 – 0.15
TI (s)	0.275 – 26.25	–

3.2.5.12. MHT

MHT technique was used in various steps of this work, one of them being the characterisation of the heating efficiency of the final SLNs, through the calculation of the specific absorption rate (SAR) of the SLNs@Fe_3O_4-MnO-dox. To this effect a MHT equipment DM1 from nanoScale Biomagnetics was used. No sample preparation was required, 250 µL of the formulation were pippetted directly into a glass vial, that was placed in the sample holder of the equipment. Then, the frequency was set to 869.0 KHz and the intensity of the magnetic field was set to 20 mT. The sample was subjected to an AMF for 1 h straight, inducing a temperature increase that was recorded in a graph of temperature variation as a function of time. The SAR could be calculated from the slope of the initial part of the T vs t curve, using the equation (1) presented in chapter 1.

3.2.5.13. Encapsulation efficiency

To study the encapsulation efficiency (EE) of dox into the SLNs, an aliquot was taken from the sample right after its synthesis, while it was immersed in ice. Then, this aliquot was extracted with chloroform. After a few minutes the non-encapsulated dox was extracted to the chloroform that was then pippetted into a HPLC vial and its dox concentration measured by HPLC. Prior to the EE measurements, a dox calibration curve was determined by HPLC using a gradient of water: acetonitrile (from 100% to 25:75%) and an Aeris 1.7 μm peptide XB-C18 column. Fluorescent detection (460 nm excitation, 560 nm emission) was used for the identification of dox peak. This calibration curve was used to calculate the dox EE, using the following equation (13):

$$EE\% = \frac{[\text{encapsulated drug}]}{[\text{total drug}]} \times 100 \tag{13}$$

3.2.6. Drug release studies

Drug release studies were performed to evaluate the capability of the SLNs to release their drug content over time. The passive release and the release induced by MHT were studied. In both cases the dox release profiles were determined by HPLC using a gradient of water: acetonitrile (from 100% to 25:75%) and an Aeris 1.7 μm peptide XB-C18 column. UV (214 nm) detection was used for the quantification of dox peak. A dox calibration curve was posteriorly used to calculate the dox concentrations in passive and induced release studies. Results from drug release experiments were performed by triplicate and expressed as mean $\pm$ standard error of the mean (SEM). Comparisons between three independent groups and between the two runs were performed with a 2-way ANOVA, followed by the Bonferroni posttest. p<0,05 was considered significant.

3.2.6.1. Passive release

The passive release studies were performed as follows: initially, 0,8 mL of Milli-Q water were loaded into a Pur-a-lyzer (6000 Da), shown in figure 41A, and left inside a beaker with Milli-Q water for 5 min. In parallel, two centrifugal filters (30000 Da) filled with Milli-Q water were centrifuged for 3 min at 7500 rpm to clean the filters. Afterwards, to filter the dox that was not encapsulated, 300 μL of a SLN@Fe$_3$O$_4$-MnO-dox solution were added to each filter and centrifuged for 40 min at 2000 rpm. The solution with encapsulated dox stayed in the filter, being transferred to new eppendorfs through inverted centrifugation for 3 min at 3000 rpm. These solutions were then combined, followed by addition of Milli-Q water to make up 600 μL. At this point three 50 mL falcon tubes (3 repetitions) with 40 mL of Milli-Q water with a Pur-a-lyzer inside were set. The filtered NP solution was loaded into each Pur-a-lyzer. Then, 1 mL of water

from the beaker cup was collected to a HPLC vial at different time points during 4 hours (0.5, 1, 2, 3 and 4 h). Note that every time water was taken from the beakers, the same volume of fresh water was added in, since the volume of water will influence the concentration of the drug, consequently influencing the drug release profile. After the experiment concluded, the vials were taken to HPLC to measure the dox release profile.

Figure 41 - Pur-a-lyzer;

3.2.6.2. Induced release

For the induced drug release experiments a MHT applicator version 1.5 with interchangeable parts from MagneTherm was used. The procedure was very similar to the one detailed for the passive release studies. In this case the falcon tube, was placed in the centre of the coil of the MHT equipment for 4 hours under an AMF (174,5 KHz; 23 mT) (figure 42). During this time the same time points as above were taken, in the same manner as in the passive release studies. Afterwards the vials were taken to HPLC to measure the dox release profiles.
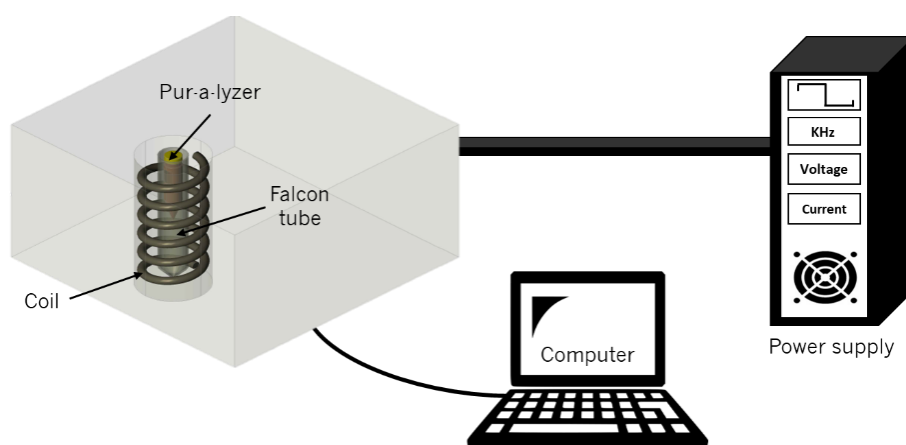
Figure 42 - Schematic representation of a MHT equipment set up for induced drug release experiments.

3.2.7. *In vitro* studies

3.2.7.1. Cell culture

Hs578T triple negative breast carcinoma cells were maintained in Dulbecco's modified Eagle's medium (DMEM) supplemented with 10 % fetal bovine serum (FBS) and 1 % Penicillin-Streptomycin and cultured in a 37 °C incubator with humidified atmosphere of 5% CO_2.

3.2.7.2. Cytotoxicity studies

Hs578T cells were seeded onto 96-well plates (2000 cells per well) and left to adhere for 24 h. Afterwards, cells were incubated with the nanoparticles SLN@MnO, SLN@MnO$_2$, SLN@Fe$_3$O$_4$, SLN@MnO-Fe$_3$O$_4$ at different concentrations respective to the metal ion (Fe, Mn, Fe+Mn) content of the nanoparticles

(0,5; 1; 1,5; 2; 5 and 10 µg/ml). Cell viability was assessed at 48 h using AquaBluer as an indicator of viable cells according to the manufacturer's recommendations. Briefly, AquaBluer reagent was diluted 100x in DMEM. The culture medium in each well was replaced with the 100x diluted AquaBluer medium (100 µL/well) and cells were placed in the CO_2 incubator for 4 hours. The fluorescence intensity at 540ex/590em was measured in a fluorescence plate reader from Biotek.

An inverted optical microscope, Eclipse TS100 with a digital sight DSFi1 camera from Nikon was used to observe the 48 h viability of Hs578T cells treated with 1.5 µg/mL of SLN@Fe$_3$O$_4$, SLN@MnO$_2$, SLN@MnO and SLN@ SLN@Fe$_3$O$_4$-MnO. The method used was a phase contrast, ideal for transparent samples, that acts by generating contrast from the phase variation of light passing through the specimen [156].

3.2.7.3. SLNs internalization

Hs578T cells were seeded in a 24 well plate onto coverslips at a density of 10^5 cells/well and left to adhere for 24 h. Cells were then incubated with SLN@MnO-Fe$_3$O$_4$-dox at a concentration of 5 µg/mL of dox (total ion concentration of 0,194µg/ml) for 4 h. Thereafter cells were washed twice with PBS (pH = 7.4) and fixed/permeabilized in ice cold methanol for 5 minutes at room temperature. Then, cells were washed with PBS and incubated with a mouse monoclonal anti-α-tubulin antibody for 1 hour at 37°C, followed by a washing step with PBS and incubation with an anti-mouse secondary antibody conjugated with AlexaFluor 647 for 1 hour at 37°C. Afterwards, cells were washed with PBS and incubated with DAPI for 5 minutes at room temperature, washed again in PBS and mounted onto a microscope slide using the Shandon Immu-mount mounting media. Cells were visualized under a scanning confocal microscope LSM780 on an inverted Axio Observer microscope from Zeiss, with the following lasers: 405 nm (DAPI); 488 nm (DiO); 561 nm (dox); 633 nm (α-tubulin). This allowed a visualization of the internalization of the SLNs, due to the presence of DiO, and the accumulation of doxorubicin in the cell nuclei after release from the SLNs.

3.2.7.4. MHT

Hs578T cells were seeded in a cell culture dish (35/10 mm) with 4 compartments at a density of 10^4 cells/well and left to adhere for 24h. Cells were incubated with the SLN@MnO-Fe$_3$O$_4$-dox, SLN@MnO-Fe$_3$O$_4$, SLN@dox and free doxorubicin at a final concentration of 2 µg/mL of dox (or corresponding amount of Fe$_3$O$_4$ in the case of SLN@MnO-Fe$_3$O$_4$). The cell culture dish was placed in a MHT applicator for one hour under an electromagnetic field (H=20 mT; f=224,53 kHz). Cells were then placed at 37 °C in an incubator with humidified atmosphere of 5 % CO_2 for 48 hours and viability was measured using

AquaBluer as an indicator of viable cells. The culture medium in each well was replaced with 100x diluted AquaBluer medium (500 µL/well) and cells were placed in the CO_2 incubator for 4 hours. The fluorescence intensity at 540ex/590em was measured in fluorescence plate reader.

3.2.7.5. Statistical analysis

Results from *in vitro* experiments were expressed as mean $\pm$ standard error of the mean. Comparisons between 3 or more independent groups and between groups with two independent variables were performed with 1- or 2-way ANOVA, respectively, followed by the Bonferroni posttest. $p < 0,05$ was considered significant.

CHAPTER 4 - RESULTS AND DISCUSSION

4.1. Synthesis of nanoparticles

For the synthesis of MNPs (Fe$_3$O$_4$, MnO$_2$ and MnO) the goal was to attain a solution with high concentration of particles and in great quantities. Since the NPs are stable in solution for long periods of time, having great quantities of these NPs will allow their utilisation for many ends, in this case to produce various SLNs. The surface of all MNPs were functionalized with either OA or Glc, to stabilize the final NPs and prevent their aggregation. This was a critical step to obtain stable monodisperse colloidal and aqueous suspensions over time.

For the synthesis of spherical magnetite NPs functionalised with OA, a hydrothermal method was tested first. Even though the quantities obtained with this method were good, the concentration of magnetite obtained was small and not ideal for its encapsulation into SLNs. Therefore, a simpler, two-step coprecipitation method was tested. This last method offers an economic route to produce great quantities of monodisperse hydrophobic Fe$_3$O$_4$@OA NPs for biomedical applications. The OA is adsorbed on the surface of the NPs through chemical interaction between OA COO groups and Fe atoms. This way the hydrophobic tails of the OA face outwards forming hydrophobic Fe$_3$O$_4$@OA NPs (figure 43). These NPs were dispersed in a non-polar solvent, CHCl$_3$, which is not only useful for their encapsulation into the SLNs, but also to prevent oxidation. The colloidal solution obtained had high concentrations of iron ([Fe]=67 mg/mL]).
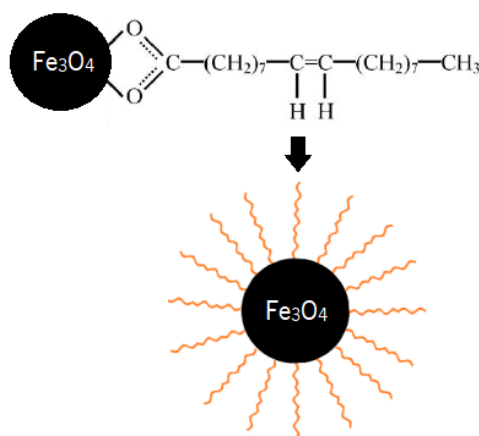
Figure 43 - Schematic representation of oleic acid-coated magnetite NPs.

For the preparation of manganese oxide NPs, a simple method based on stirring was used. The main reaction is based on the reduction of the KMnO$_4$ by the OA, being that the molar ratio of these two compounds crucial to determine the size and morphology of the nanostructures [195]. As the reaction is conducted in water, it is easier scale up, offering an economic route for the preparation of MnO. Therefore, with this method great quantities of a monodisperse colloidal solution of MnO@OA NPs were obtained, with a concentration of manganese of 44.6 mg/mL. Unlike magnetite, MnO NPs present an irregular shape that can vary by using different molar ratios of KMnO$_4$/OA, in this case the particles present themselves in the form of nanosheets (figures 48A and 48B).

For the synthesis of manganese dioxide NPs, various methods were tested along the way. The main problem with most of these methods was that the NPs presented very low concentrations with non-

uniform shapes. Also, despite the hydrophobic character of the prepared NPs, its encapsulation into the SLNs was not efficient. For these reasons hydrophilic MnO_2@Glc NPs were produced using a sonochemical method that is an easy one step method to break $KMnO_4$ chemical bounds. The reaction is based on a mild reduction of MnO_4^- by Glc. With this method high quantities of "crushed paper" like NPs were obtained with a low manganese concentration of 0.412 mg/mL. Despite their hydrophilic character these were the only MnO_2 NPs produced, that were efficiently loaded into the Carnauba matrix of the SLNs, yet in minimal concentrations.

For the SLNs synthesis a modified melt emulsification method was used due to its simplicity and scalability [198]. With this method monodisperse aqueous solutions of SLNs containing MNPs and dox were obtained. The organic matrix of the NPs made of the biocompatible and FDA approved Carnauba wax, its ideal to incorporate the MNPs and the drug. The procedure allows to obtain SLNs with a regular size and zeta potential, however from batch to batch it is difficult to obtain constant concentrations of MNPs in the SLNs. As showed on chapter 3, different formulations had different percentages of magnetic content, but even when these theoretical percentages were the same in different batches, variable concentrations of MNPs were obtained. Table 7 shows the different values of concentration for each ion (Mn and Fe) in each formulation. Mn concentrations are always much lower than the theoretical values (as expected on the other hand at least for MnO_2 due to their hydrophilic nature), which can limit the Mn NPs utility in biomedical applications.

Table 7 - Concentration of ions for each SLN formulation.

Formulation	Fe (mg/mL)	Mn (mg/mL)
SLN@ Fe_3O_4	1.470	-
SLN@ Fe_3O_4–dox	0.200	-
SLN@MnO_2	-	0.141
SLN@ Fe_3O_4–MnO_2-dox	0.083	0.117
SLN@MnO	-	0.289
SLN@ Fe_3O_4–MnO	0.347	0.129
SLN@Fe_3O_4–MnO–dox	0.222	0.042

In the synthesis of SLNs containing dox the concentration of drug, fixed at 20% in relation to the Carnauba wax, was totally reproducible. Different batches with the same theoretical percentages of dox, showed constant encapsulation efficiency values of almost 100%. Nevertheless, the content of dox is spontaneously released over time until the quantity of dox inside and outside the lipid particles is the same, so the percentage obtained can be lower over time. For the final formulation (SLN@Fe_3O_4-MnO-

dox) the EE was 99.6±0.2 %, which is an encouraging result. The concentration of DiO was fixed from the beginning to a level at which it is ideal for fluorescent optical imaging.

4.2. Physico-chemical characterisation

4.2.1. (Para)magnetic nanoparticles

MNPs and lipid NPs were extensively characterised in the present study. Structural, chemical, magnetic and functional characterisation were performed through the techniques mentioned in chapter 3, to exploit the NPs capabilities and understand their behaviour, in order to validate the final bionanosystem for biomedical applications.

Magnetite NPs stabilized with OA were first structurally characterised using TEM. The size obtained by TEM analysis corresponds only to the NP crystal core (without the organic coating). From figures 44A and 44B, acquired with 50k and 500 k times magnification respectively, it is possible to see that the magnetite NPs present a pseudo-spherical shape with a monodisperse distribution. The average size was determined by measuring 300 NPs from several TEM micrographs. The measurements revealed that the size of the crystals vary from 4 to 18 nm, and present a bell-shape size distribution that could be fitted to a Gaussian equation, characteristic of this kind of magnetic particles (figure 44C) [199]. The particles were measured, presenting an average diameter of 9.7±0.1 nm.
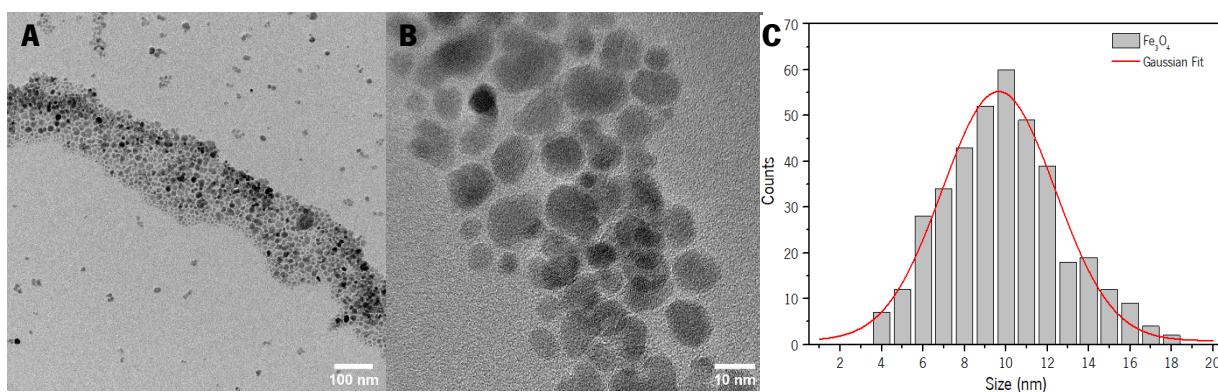
Figure 44 - A-B: TEM micrographs of magnetite NPs capped with OA; C- Size distribution obtained by TEM of OA capped magnetite NPs, fitted to a Gaussian distribution.

The X-ray diffraction pattern of Fe_3O_4@OA NPs presents well-defined diffraction peaks, signifying that these NPs are highly crystalline. Figure 45 shows the XRD spectra obtained and the already documented magnetite pattern. The diffraction peaks with 2θ values of 30.1, 35.5, 37.1, 43.1, 53.5, 57 and 62.6 degrees are in agreement with the known Bragg reflections of magnetite (Crystallography Open Database), which are indexed as (2,2,0), (3,1,1), (2,2,2), (4,0,0), (4,2,2), (5,1,1) and (4,4,0) [200]. When in contact with oxygen magnetite can be easily oxidized and transformed into maghemite and hematite at high

temperatures [201]. The absense of diffraction peaks characteristic of these coumpounds or any other secondary phase in the XRD spectrum, indicates that the synthetyzed product is purely magnetite.
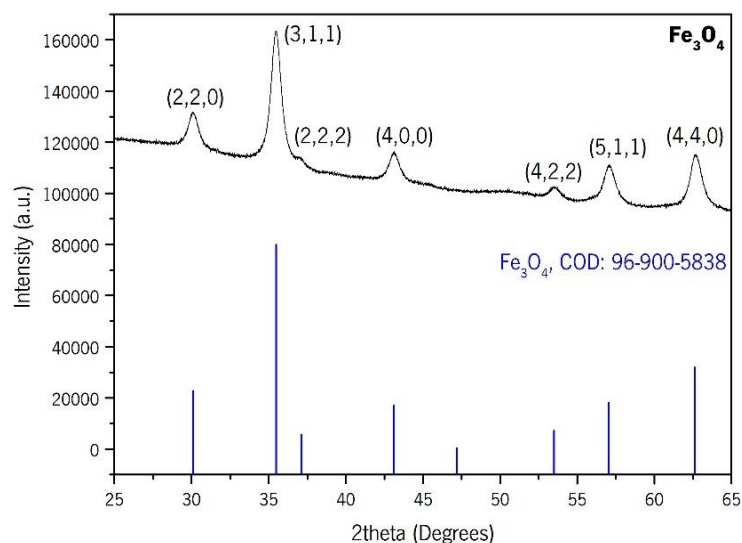
Figure 45 - X-ray diffraction pattern of oleate-coated magnetite.

The thermogram obtained by thermogravimetric analysis for oleic acid-coated magnetite NPs is shown in figure 46. The TGA curve shows three distinguished steps of wheight loss. Over the temperature of 120 to 300 °C, ①, the weight loss corresponds to the physic decomposition of the OA adsorbed on the surface of the NPs; from 300 to 500 ° C, ②, to the chemical decomposition of this coating agent [202], [203]. The reason for the third weight loss its not clear, but one hypothesis can be that its due to the reducing gases produced by the OA degradation. Thus, the weight loss represented on ③, above 700 °C may be of the magnetite itself due to its reduction by the reducing gases produced during the OA decomposition [203]. From this analysis it is possible to extrapolate that the Fe_3O_4@OA NPs contain aproximately 10% of OA.
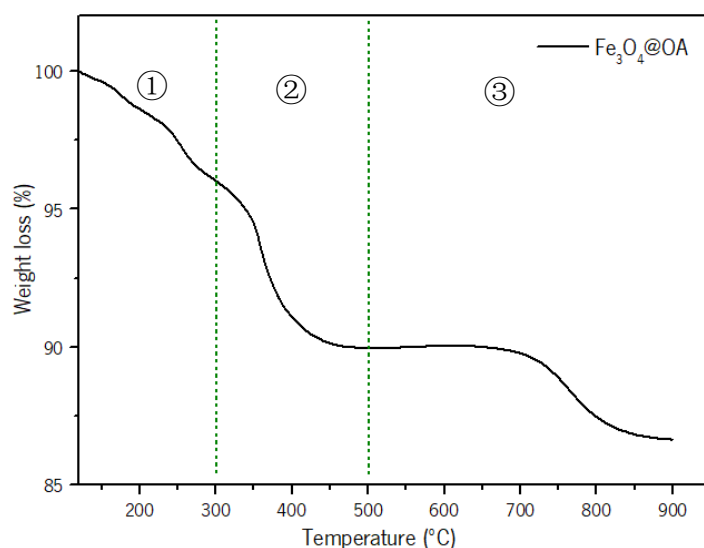
Figure 46 - Thermogravimetric profile of the hydrophobic Fe_3O_4@OA in N_2 atmosphere.

The magnetic properties oleate-capped magnetite NPs were measured with the SQUID-VSM equipment at 5 K and 300 K (room temperature). The field-dependent magnetization curves, represented on figure 47A, show the typical superparamagnetic behaviour of magnetite NPs. The hysteresis loop is more evident at 5 K, suggesting that at low temperature these particles are in a superparamagnetic magnetically blocked regime showing ferromagnetic-like behaviour (open hysteresis loop). However, at room temperature, they behave as a pure superparamagnetic, in which both remanent magnetization and coercivity are very close to 0 (M_r= 2.9 emu/g; H_c= 0.03 kOe). The Fe_3O_4@OA NPs present high saturation magnetization (M_s= 67 emu/g), significantly lower than the value of bulk magnetite (M_s= 92 emu/g). It is important to highlight that the M_s value was higher than that of Feridex® (M_s= 45 emu/g), which is a SPION formulation FDA approved as MRI contrast agent [204]. The reduced magnetization compared to the bulk material, may be attributed to the phenomenon of spin canting, defined as a non-uniform distribution of spins [205]. The distortion of the spin alignment is more pronounced at the surface of the particles, leading to a higher reduction of saturation magnetization in particles with a higher surface to volume ratio, like the oleate-capped magnetite NPs [205]. However it is important to note that the M_s value obtained for these particles increases, if only the magnetite core of the particles is taken into account for the magnetization normalization, instead of the total mass of the sample. Lastly, figure 47B shows the zero-field cooled and field cooled (ZFC-FC) magnetization curves under an applied magnetic field of 100 Oe. These curves reveal a blocking temperature (T_B) of 150 K, which represents a magnetic transition from a magnetically blocked state to a superparamagnetic regime for the synthetised OA-capped SPIONs.
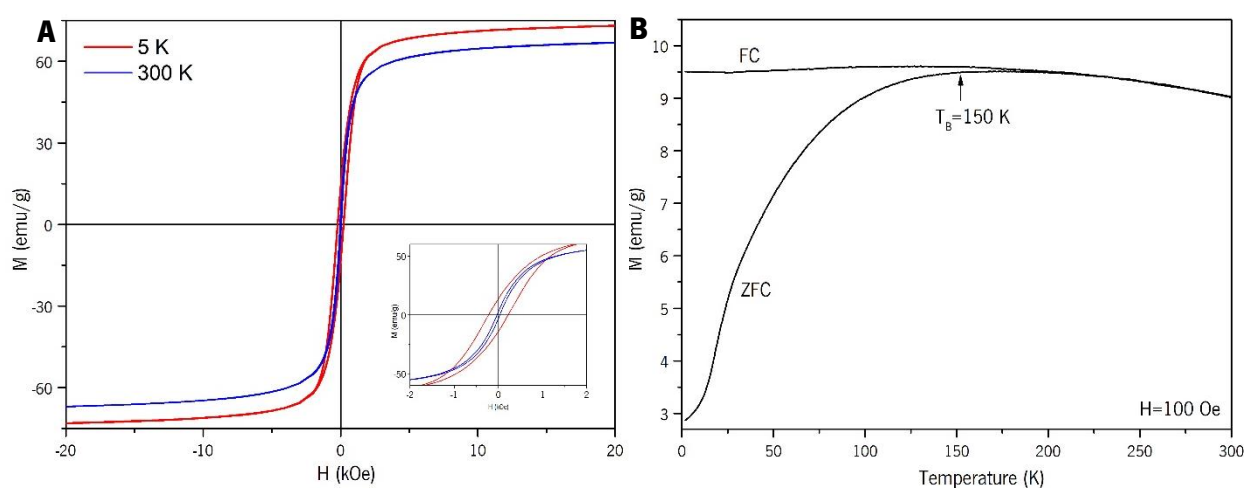
Figure 47 - A: Field-dependent magnetization curves of OA-capped magnetite NPs at 5 and 300 K. The inset is a close-up of both curves; B: ZFC-FC magnetization curves under a magnetic field of 100 Oe.

Paramagnetic manganese oxide NPs (MnO@OA) were structurally characterised by TEM. The size obtained with this technique is attributed to the nanoparticle without the oleic acid coating as in the case of magnetite NPs explained before. As seen in figures 48A and 48B, acquired with 50 k and 150 k times

magnification respectively, the MnO is presented as nanosheets that form spherical aggregates of themselves. The size of these NPs could not be perceived clearly, so the measurements where made along the major axis of the spherical form, formed by the nanosheets. The average size was determined by measuring 100 NPs in different micrographs. The size varied from 30 to 100 nm and the determined average size was 53.6$\pm$2.5 nm, still small enough to be considered for encapsulation.
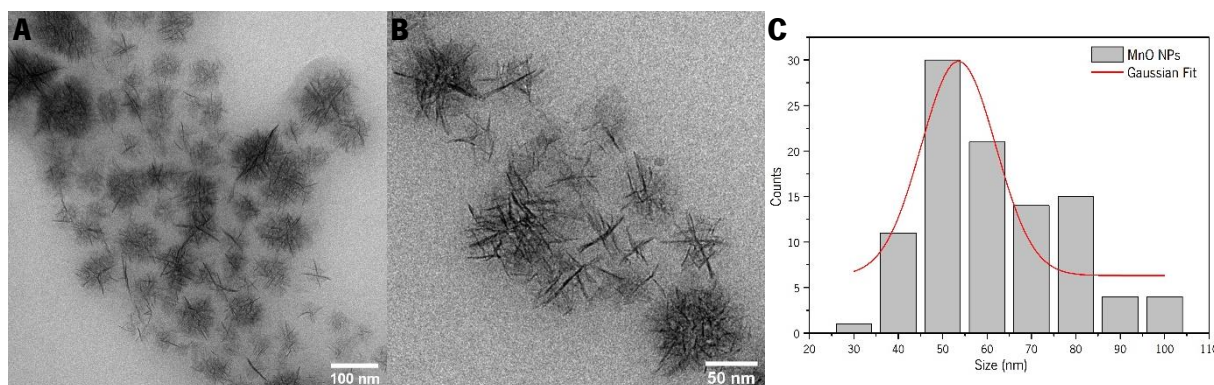
Figure 48 - A-B: TEM micrographs of MnO NPs capped with OA; C- Size distribution obtained by TEM of OA capped MnO NPs, fitted to a Gaussian distribution.

The absorbance of the colloidal suspension of MnO was acquired by UV-Vis spectroscopy. The spectrum shows a shoulder of absorption around 350-400 nm, which is typical of this kind of MNPs [206]. This absorbance may be due to the quantum confinement effects of MnO nanosheets, that are present at nanometric scale [207].
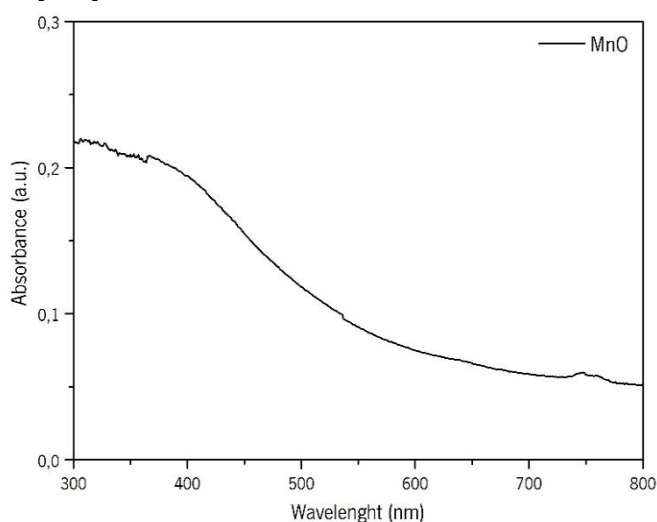
Figure 49 - UV-Vis spectrum of colloidal solution of MnO@OA nanosheets.

Figure 50 shows the X-ray diffraction pattern obtained for these particles and the already documented MnO pattern. The XRD spectrum of MnO@OA NPs did not present well-defined diffraction peaks, thus a background subtraction was made so the existing peaks became more distinguishable. The diffraction peaks with 2θ values of 35.2, 40.9 and 88.7 degrees are the only peaks in agreement with the known Bragg reflections of MnO (Crystallography Open Database), which are indexed as (1,1,1), (0,0,2) and

(0,0,4) [200]. The identified peaks are not sufficient to extrapolate from the XRD graph that the analysed sample is indeed manganese oxide. This could be due to the versatile nature of Mn and its many oxidation states, which in addition to with the nano size of the particles that broadens the peaks, makes it very difficult to unequivocally identify the phase of the particles.
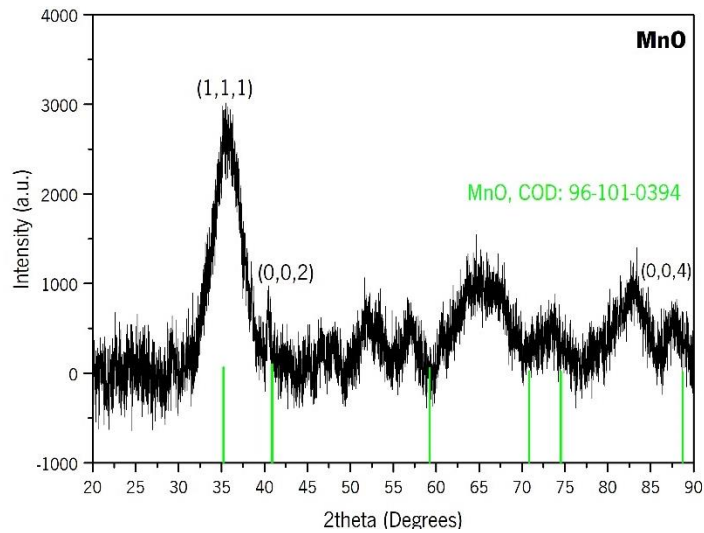
Figure 50 - X-ray diffraction pattern of oleate-coated manganese oxide nanosheets.

The magnetic behaviour of MnO@OA NPs was analysed by a vibrating sample magnetometer. This equipment is less sensible than the SQUID-VSM, but it is able to determine the magnetic character of a sample. The field-dependent magnetization curve of OA coated MnO NPs measured at room temperature is shown in figure 51. Through the observation of figure 51 it is possible to notice that no M_s or hysteresis are present and the curve is almost a straight line. This linear increase of the magnetization with the applied magnetic field indicates that the sample has a paramagnetic behaviour, in agreement with the reported magnetic behaviour for manganese oxide NPs, with a maximum magnetization of 0.15 emu/g at the highest field measured [208].
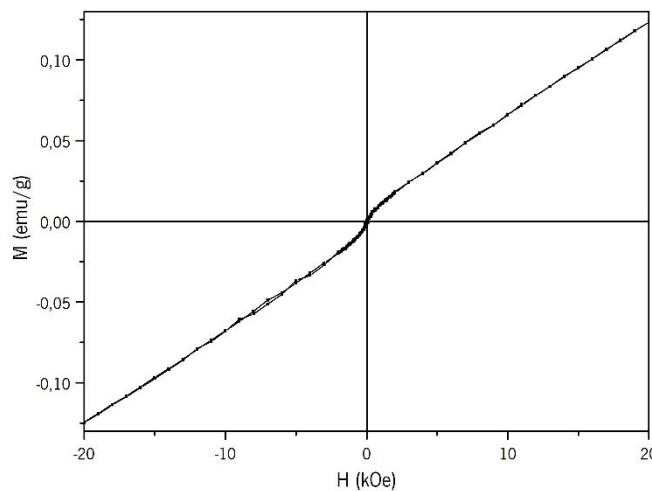
Figure 51 - VSM graph for MnO@OA nanosheets.

Responsive manganese dioxide NPs functionalized with glucose where morphologically characterised using TEM. As seen in figures 52A and 52B, acquired with 50 and 120 k magnification respectively, the MnO$_2$ is presented as nanosheets with an irregular shape resembling crushed paper sheets. The size of MnO$_2$@Glc could not be perceived clearly, so the measurements where along the major axis of more external nanoparticles. The average size was determined by measuring 100 NPs from different TEM micrographs. The size varied from 15 to 30 nm and the determined average size was 21.8±0.3 nm, which is ideal for the encapsulation into the SLNs.
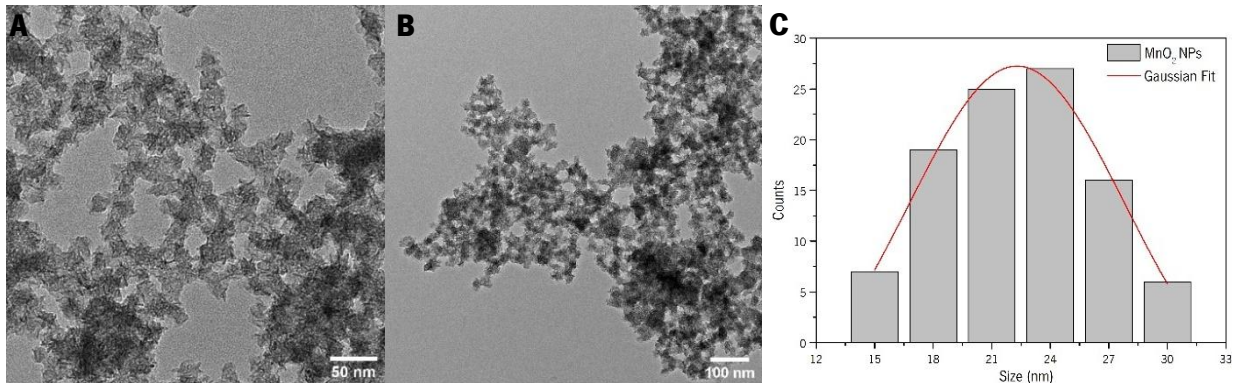
Figure 52 - A-B: TEM micrographs of MnO$_2$ NPs capped with glucose; C- Size distribution obtained by TEM of OA capped MnO NPs, fitted to a Gaussian distribution.

The absorbance of the aqueous solution of MnO$_2$ was obtained by UV-Vis spectroscopy. Like the MnO NPs, the spectrum shows a shoulder of absorption around 350-400 nm, which is characteristic of MnO$_2$ nanosheets [5]. As before, quantum confinement effects are responsible for this behaviour.
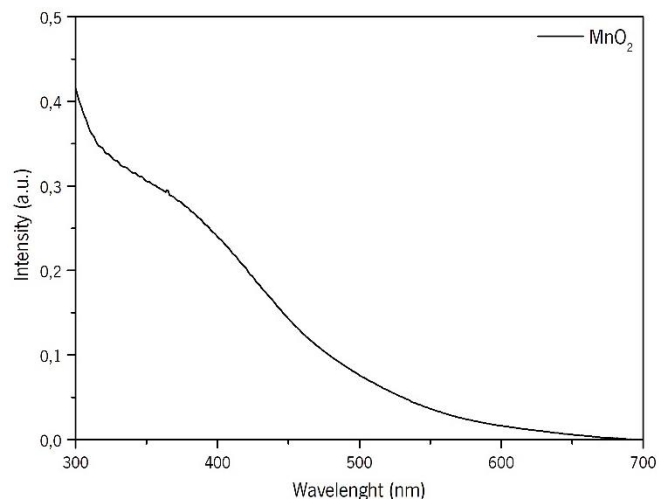
Figure 53 - UV-Vis spectrum of colloidal solution of MnO2@Glc nanosheets.

The XRD spectrum obtained for these particles and the documented MnO$_2$ pattern are shown in figure 54. The spectrum of MnO$_2$@Glc NPs did not present well-defined diffraction peaks, which as mentioned above may be due to the various oxidation states existing for Mn and to the effect of the nano size of the particles that broadens the peaks. The diffraction peaks with 2θ values of 37.2, 67.1 degrees

are in agreement with the known Bragg reflections of MnO_2 (Crystallography Open Database), indexed as (0,1,0) and (1,1,0) [200]. The information retrieved from this diffractogram is again not enough to extrapolate the crystalline structure of the sample. It is important to note that at the nanometric scale preferential crystallographic orientations can appear, that modify the peak intensity relations and hinder the phase identification by comparison with a given database.
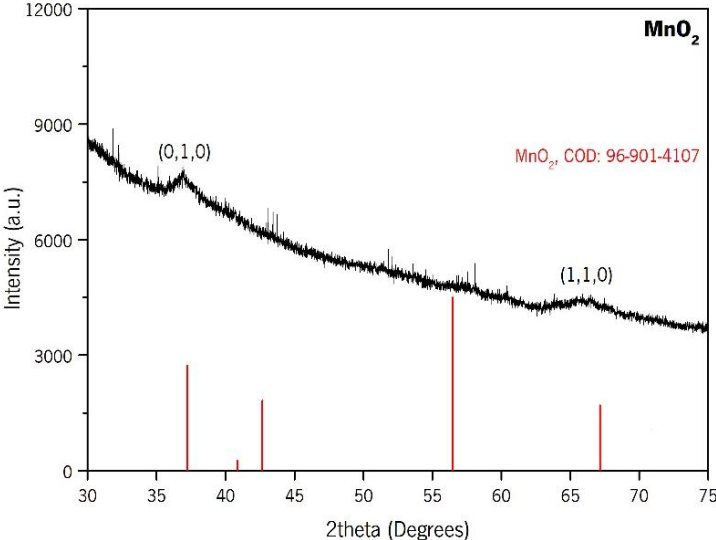
Figure 54 - X-ray diffraction pattern of glucose-coated manganese dioxide nanostructures.

The magnetic behaviour of manganese dioxide NPs functionalized with glucose was analysed by a VSM. The magnetization curve of MnO_2@Glc nanosheets, represented in figure 55, was measured at room temperature. The measured sample exhibits the typical paramagnetic behaviour (linear increase of the magnetization with the magnetic field) characteristic of manganese dioxide NPs, with a maximum magnetization of 0.8 emu/g at the highest magnetic field measured   [208].
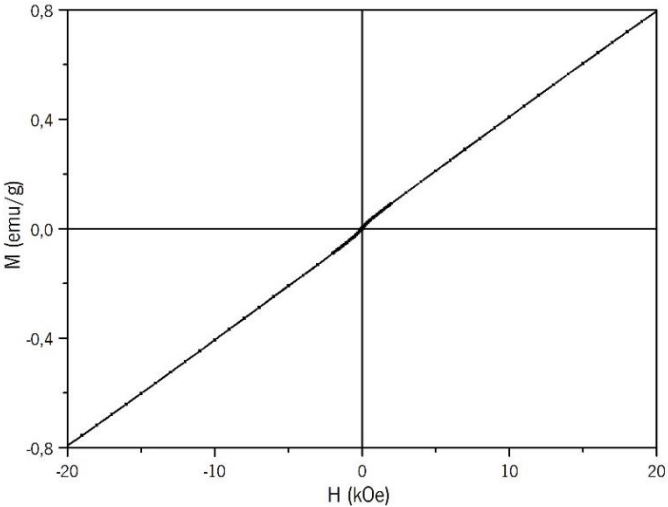
Figure 55 - VSM graph for MnO_2@Glc nanosheets.

4.2.2. Solid lipid nanocarriers

The solid lipid nanocarriers were first characterised using dynamic light scattering. Regarding the size of the different nanocomposites, DLS analysis provided a hydrodynamic diameter of around 150/200 nm with a PI varying between 0.2 and 0.6, indicating that the values obtained for size are reliable. The zeta-potential of the particles was also analysed, giving that the particles with no drug presented great stability with values of ζ-potential around -50 mV. However, the particles loaded with drug suffered a ζ-potential inversion to values of around 25 mV, due to the positive charge of dox at physiological pH (pKa=8.4, PubChem). The concrete values for each formulation are presented in table 8. For the final formulation (SLN@Fe₃O₄-MnO-dox) the hydrodynamic size was 170 ± 14 nm with a PI of 0.24 ± 0.06, which in terms of particle size indicates its suitability for administration. The ζ-potential for this formulation was 29 ± 1 mV, which is the threshold for a good stable formulation (if stabilised only by electrostatic repulsion).

Table 8 - DLS and ELS analysis results for each SLN formulation.

Formulation	PI	Size (nm)	ζ-potential (mV)
SLN@dox	0.49 ± 0.03	133 ± 19	24 ± 2
SLN@ Fe₃O₄	0.36 ± 0.04	185 ± 58	-67 ± 10
SLN@ Fe₃O₄–dox	0.51 ± 0.01	146 ± 6	22 ± 2
SLN@MnO₂	0.39 ± 0.00	153 ± 40	-50.0 ± 0.8
SLN@ Fe₃O₄–MnO₂-dox	0.63 ± 0.04	118 ± 11	38 ± 1
SLN@MnO	0.50 ± 0.02	197 ± 1	-45.0 ± 0.14
SLN@ Fe₃O₄–MnO	0.45 ± 0.04	145 ± 10	-48.1 ± 0.6
SLN@Fe₃O₄–MnO–dox	0.24 ± 0.06	170 ± 14	29 ± 1

All the SLNs were morphologically characterised using TEM. Unlike other lipid systems, the high melting point of Carnauba wax (82-86 °C) enables direct TEM imaging. The particles observed by TEM may lose their content, aggregate and appear bigger than the size obtained by DLS, this can happen due to the vacuum they are submitted to after being deposited on the grid and to changes in the particles while being irradiated with the electron beam for a long time.

A TEM micrograph of the SLNs@dox taken at 12 k magnification, is shown in figure 56A. The SLNs appear as dark spherical forms, due to its dox content. Their size seems bigger (200-300 nm) than the one determined by DLS and the particles are slightly aggregated and deformed. As mentioned above, sample preparation for TEM require the vacuum drying of samples which deform the particles going from spherical form to squashed spheres, appearing larger in 2D TEM images [209]. The optical properties of

these particles were also studied by fluorescence spectroscopy. Figure 56B shows the fluorescence spectra for the SLNs@dox, showing a fluorescence peak at 562 nm with a second shoulder around 590 nm that matches the position of the peak from free dox, but normally the second peak is more intense [210], [211]. This optical behaviour indicates the presence of dox in the NPs, thus its efficient encapsulation into the lipid carrier.
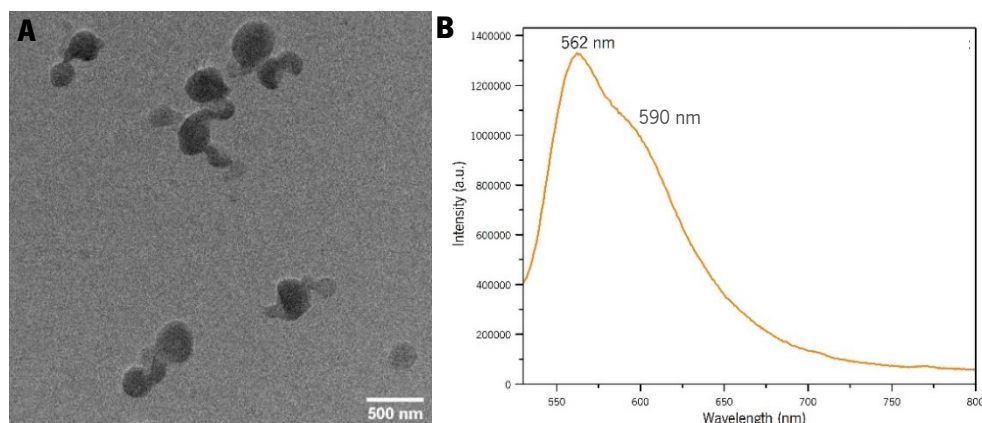
Figure 56 - A: TEM micrograph of SLNs@dox; B: Fluorescence spectrum of SLNs@Dox at an exitation wavelenght of 480 nm.

The SLNs containing only SPIONS (30 %) and SPIONS-dox (5 %) are shown in figures 57A (25 k magnification) and 57B (12 k magnification), respectively. Both the formulations present SLNs with a spherical shape, however the formulation containing doxorubicin seemed more unstable, which is in accordance with the zeta-potential observed. The presence of magnetite nanoparticles inside the SLNs is clearly observed in both samples. It is also observed that the magnetite nanopartilcles in sample SLNs@Fe$_3$O$_4$ (30% Fe) are uniformly distributed inside the SLNs particles, whereas in SLNs@Fe$_3$O$_4$-dox (5 % Fe) the ironcontent is much lower and the nanoparticles are found unheavenly dispersed in the sample.
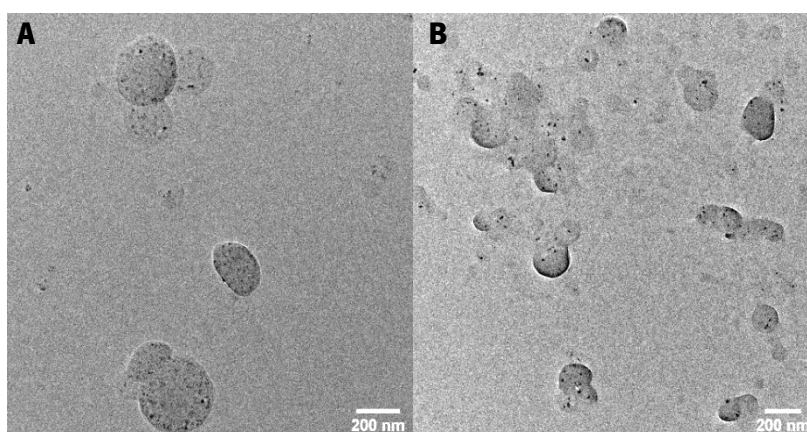
Figure 57 - A: TEM micrograph of SLNs@Fe$_3$O$_4$; B: TEM micrograph of SLNs@Fe$_3$O$_4$-dox.

The TGA curves for SLNs containing 5 and 30 % of Fe$_3$O$_4$@OA NPs are shown in figure 58. The first step of weight loss, ①, is the most relevant and represents the degradation of the organic components of the SLNs. Above 250 °C the degradation of the surfactant Tween 80 initiates and its later accompanied by the degradation of the Carnauba wax, that has been reported to initiate at around 360 °C [212]–[214].

The weight loss for the red curve (SLNS@Fe$_3$O$_4$-dox) is more prominent due to its larger organic/inorganic content ratio. The presence of doxorubicin in this system may contribute to accentuate the weight loss in ①, since this drug degradation can occur at around 237, 320 and 400 °C [215]. The OA also degrades in the first step [202]. The second step of weight loss is minor, ②, and the reasons for its occurrence are unclear. It is possible to be due to the continuous degradation of the Carnauba wax, which has been reported to also occur at around 440 and 520 °C [213]. Another hypothesis may be the slight degradation of the magnetite itself [203]. The inorganic content of SLN@Fe$_3$O$_4$ and SLN@Fe$_3$O$_4$-dox was of 54 and 42 %, respectively.
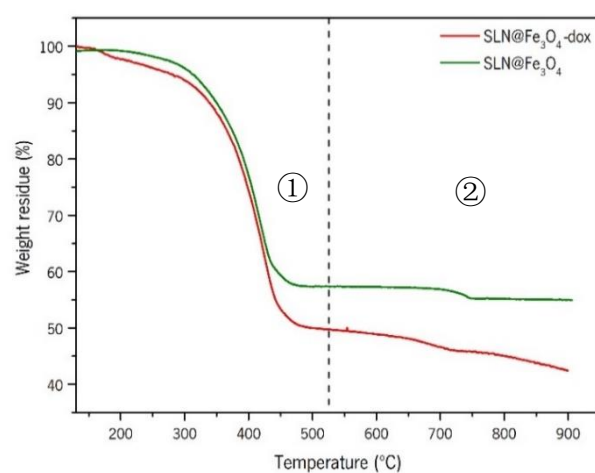
Figure 58 - Thermogravimetric profiles of SLNs@Fe$_3$O$_4$ with and without dox in N$_2$ atmosphere.

The magnetic properties of SLNs@Fe$_3$O$_4$, with and without dox, were measured with the SQUID-VSM equipment at room temperature. The field-dependent magnetization curves (figure 59A) and the ZFC-FC magnetization curves of under an applied magnetic field of 100 Oe (figure 59B) confirm the superparamagnetic behaviour of these particles. The curves for OA-coated magnetite NPs are also represented in both graphs for comparison.
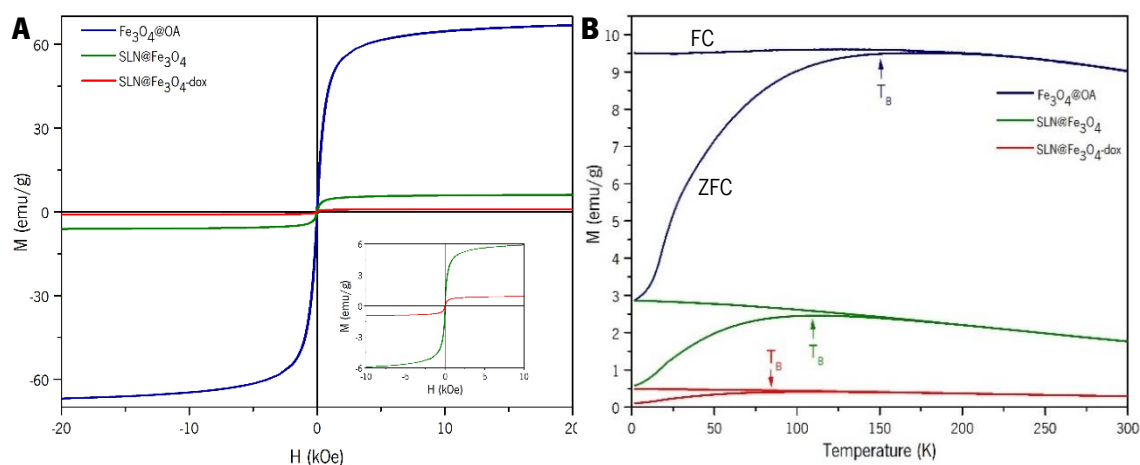
Figure 59 - Field-dependent magnetization curves of SLN@Fe$_3$O$_4$ with and without dox and Fe$_3$O$_4$@OA at 300 K; B: ZFC-FC magnetization curves under 100 Oe.

As expected, the non-encapsulated magnetite NPs present much higher saturation magnetization values than the SLNs containing magnetite, and in turn the SLNs with 30 % of magnetite (SLNs@Fe$_3$O$_4$)

showed higher M_s values than the SLNs with 5 % of magnetite (SLNs@Fe₃O₄-dox). The great difference in M_s between the mSLNs and the magnetite alone is due to the differences in concentration of iron in the total mass of the sample. This also occurs when comparing the mSLNs with and without dox, since the final Fe content in them was found to be significantly different, as determined by ICP. The M_r and H_c values are also smaller when the magnetite is encapsulated, nevertheless all the particles present values close to zero, which is indicative of their superparamagnetic behaviour. This could be ascribed to the weaker magnetic dipolar interactions between magnetite nanoparticles that occur when they are encapsulated inside the SLNs. Their spatial distribution in the lipid matrix increases the nanoparticle-nanoparticle distance and reduces their magnetic interaction. This is also confirmed by analysing the blocking temperature (T_B) in the ZFC-FC curves. The T_B is clearly greater for the oleate-capped magnetite NPs compared to the mSLNs (150 K vs 109 K/86 K). Also, it is higher for the mSLNs with higher concentration of SPIONs (109 K vs 86 K). By increasing the concentration of magnetite in the lipid wax matrix, the magnetic interactions between the particles increase, leading to a positive shift in the blocking temperature of the materials. Table 9 summarizes the magnetic properties of each particle.

Table 9 - Magnetic properties of each particle.

	[Fe] (mg/mL)	M_s (emu/g)	M_r (emu/g)	H_c (kOe)	T_B (K)
Fe₃O₄@OA	67	67	2.9	0.03	150
SLN@Fe₃O₄	1.5	6.1	0.77	0.036	109
SLN@Fe₃O₄-dox	0.2	1	0.13	0.036	86

The SLNs@MnO₂ observed by TEM are shown in figures 60A and 60B, acquired at 20 k magnification. In general, the particles present spherical shapes and bigger sizes (200-400 nm) than those determined by DLS. In most of the images, the particles appear more aggregated than the previous ones, which may be not just because of the vacuum effects, but also because of the encapsulation of hydrophilic NPs into the hydrophobic core of SLNs. The red arrows in both figures point to the presence of MnO₂ NPs inside the SLNs.
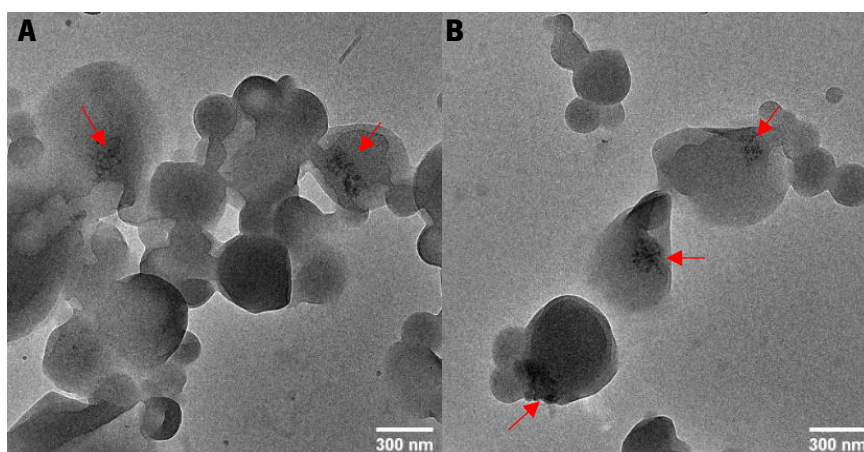
Figure 60 – A,B: TEM micrographs of SLN@MnO₂, the red arrows point to what its thought to be the MnO₂@Glc NPs.

Since the encapsulation of the particles into the SLNs is less evident than in the case of magnetite, and this is an important step to proceed with the experiments, a STEM-EDX analysis was performed. A STEM-EDX map for the SLNs containing MnO_2@glc is presented in figure 61. It consists in the mapping of elemental manganese throughout a selected region of an image acquired in STEM mode. The pink dots in figure 61 represent the Mn element distribution in the selected area. The STEM-EDX

Figure 61 - STEM-EDX mapping of SLNs@MnO₂.

analysis revealed that the MnO_2 NPs are present in the SLNs, confirming their encapsulation despite their hydrophilic character.

No further physico-chemical characterisation was performed for the SLN's containing manganese dioxide, since the formulation did not turn out as expected, presenting high aggregation and instability. Nevertheless, a final formulation of SLNs containing MnO_2@glc, Fe_3O_4@OA and dox was synthetized to evaluate if the co-encapsulation of the two kinds of MNPs was viable.

The TEM micrographs of SLNs@Fe_3O_4–MnO_2-dox, acquired at 20 k magnification, are shown in figures 62A and 62B. The particles observed present irregular shapes and appear aggregated being difficult to distinguish the particles boundaries. The red arrows in both images point to MnO_2 NPs, and although further imaging acquisitions would be needed to confirm, most of them seem not to be totally inside the particles but attached or embedded in. SPIONs can also be seen in both images as small black dots, and since the Fe concentration in these SLNs in much lower than the Mn, SPIONs are observed in considerably lower quantities. In previous formulations both the MNPs (SPIONs and MnO_2) were individually encapsulated into the SLNs, but when put together, and according to TEM images (bearing in mind that TEM is not the most adequate methodology to infer stability) the formulation showed greater instability. This very likely due to the hydrophilic/hydrophobic character of them, although magnetic interactions between the MnO_2@glc and the Fe_3O_4@OA NPs cannot be discarded. As explained above, SLNs@Fe_3O_4–MnO_2-dox showed great instability and no further physico-chemical characterisation was performed.
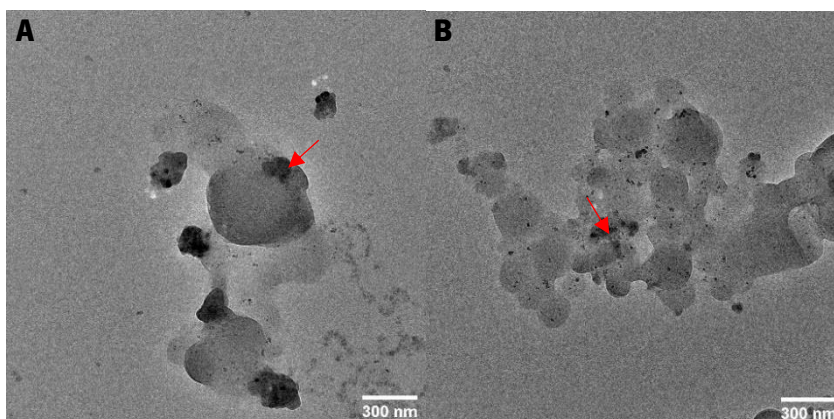
Figure 63 - A,B: TEM micrographs of SLN@Fe₃O₄-MnO₂-dox, the red arrows point to what its thought to be the MnO₂@Glc NPs.

Manganese oxide was also used for encapsulation into the SLNs, with the purpose of obtaining a dual contrast in MRI. SLNs containing MnO@OA were morphologically characterised by TEM. Figures 63A and 63B, acquired at 20 k and 40 k magnification respectively, show spherical SLNs@MnO. In general, the formulation appeared stable and the MnO NPs efficiently encapsulated in the wax matrix. The red arrows in both images point to MnO@OA NPs.
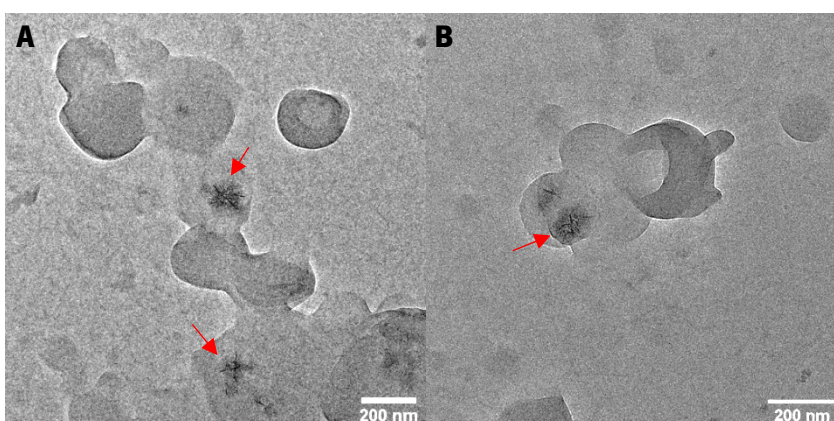
Figure 62 - A,B: TEM micrographs of SLN@MnO, the red arrows point to the MnO@gOA NPs.

The thermogram for SLNs containing MnO@OA NPs is shown in figure 64. The curve displays only one major step of weight loss, ①, that represents the degradation of the organic components of the SLNs. As stated before for SLNs@Fe₃O₄, the step of weight loss from 250 to 500 °C corresponds to the degradation of the surfactant Tween 80, the Carnauba wax and the OA [202], [212]–[214]. The inorganic content of SLNs@MnO was found to be 42 %.
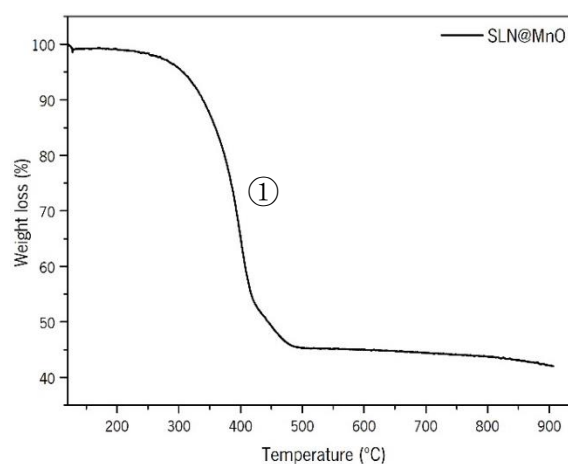
Figure 64 - Thermogravimetric profile of SLNs@MnO in N₂ atmosphere.

The magnetic properties of SLNs@MnO, were measured with the SQUID-VSM equipment at 5 and 300 K. The field-and temperature dependent magnetization curves are presented in figures 65A and 65B, respectivily. The magnetization curves show a linear M-H relationship, confirming the paramagnetic character of these NPs. The maximum magnetization is approximadely ten times greater at 5 K (0.5 emu/g) than at room temperature. According to the Curie law, $\chi_{PM} = C/T$, this is explained by the inversely proportional temperature dependence of the paramagnetic susceptibility (χ_{PM}). The magnetization curve at 300 K also shows a very small diamagnetic contribution in the low field region that comes from the diagmagnetic behavior of the sample holder plus the cotton used to stick the powder to the gelatine capsule, which is only observed at low magnetic fields where the magnetization is very low for paramagnetic substances. As the magnetic field increases, the paramagentic behavior of the sample increases and the diamagnetic contribution is no longer appreciated. In the M vs H curve at 5K the paramagnetic susceptibility is higher and this diamagnetic contribution is not even observed (see inset of Figure 65). The ZFC-FC curves show a strong magnetization decay with temperature that obeys the Curie law characteristic of paramagnetic materials [216]. A peak is observed at low temperature whose origin is unclear. In order to elucidate the origin of this magnetic feature a more detailed magnetic characterization should be performed.
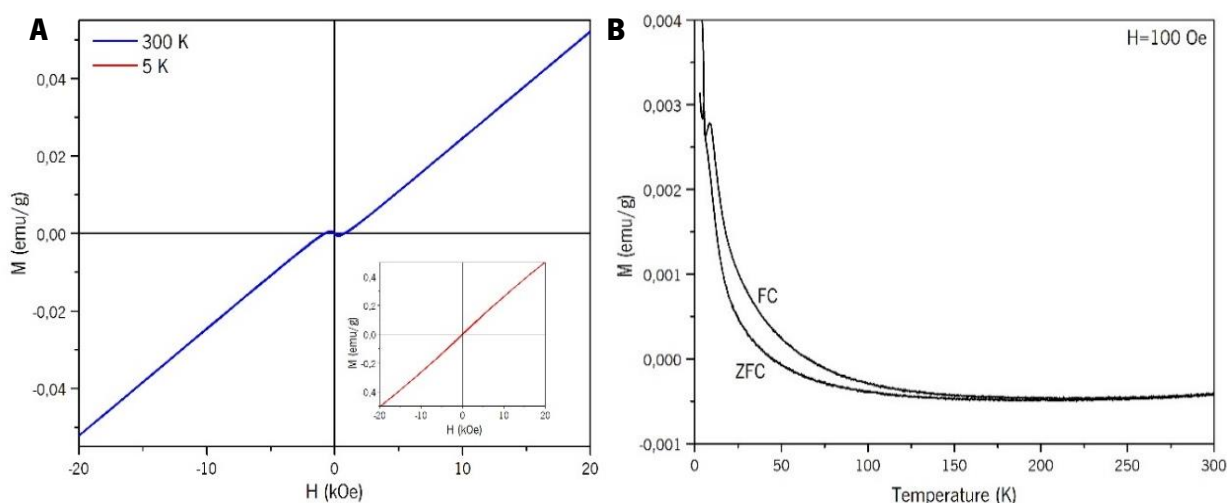
Figure 65 - Field-dependent magnetization curves of SLN@MnO at 300 K and at 5 K (inset); B: ZFC-FC magnetization curves at 100 Oe.

Prior to the synthesis of the final NPs (SLNs@Fe₃O₄-MnO-dox) it was necessary to evaluate if the oleate-caped magnetite and manganese oxide NPs could be encapsulated together. Thus, SLNs@Fe₃O₄–MnO were observed by TEM and are shown in figures 66A and 66B, acquired at 50 k and 60 k magnification respectively. The particles are spherical, evenly disperse and their size is more similar to the one obtained by DLS (150-200 nm), suggesting a higher structural rigidity. The red arrows and the yellow arrows in both images point to MnO@OA and Fe₃O₄@OA NPs, respectively. Interestingly, the MNPs are efficiently and simultaneously encapsulated into the SLNs, which is a promising result.
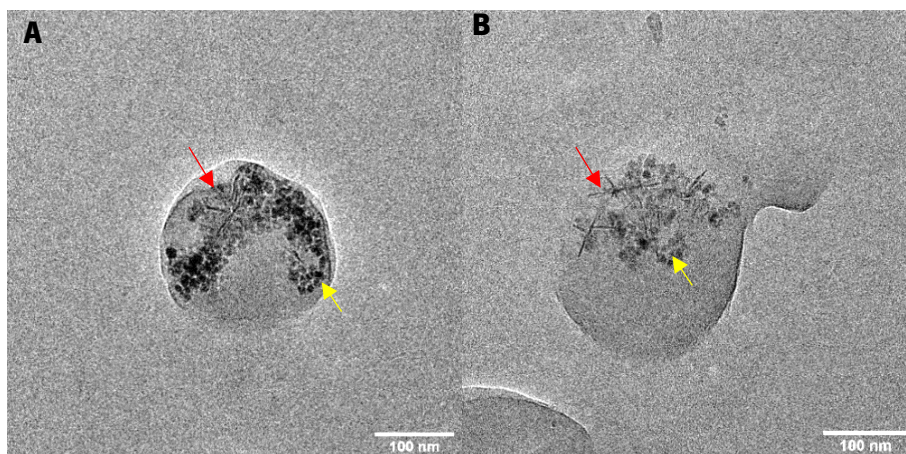
Figure 66 - A,B: TEM micrographs of SLN@Fe₃O₄-MnO, the red arrows point to the MnO@OA NPs and the yellow arrows point to Fe₃O₄@OA NPs.

Finally, the SLNs@Fe$_3$O$_4$-MnO-dox were physico-chemically characterised. Figures 67A and 67B, show the TEM micrographs of these NPs, acquired with 20 k magnification. The SLNs present a spherical shape and some aggregation. This aggregation can be due to the presence of dox, but a stronger hypothesis is that it is caused by drying the samples in vacuum, as it was previously introduced. As in the dox free version of the SLNs, both MNPs were found to be efficiently encapsulated into the SLNs. In both images it is possible to identify the MnO@OA (red arrows) and the Fe$_3$O$_4$@OA (yellow arrows).
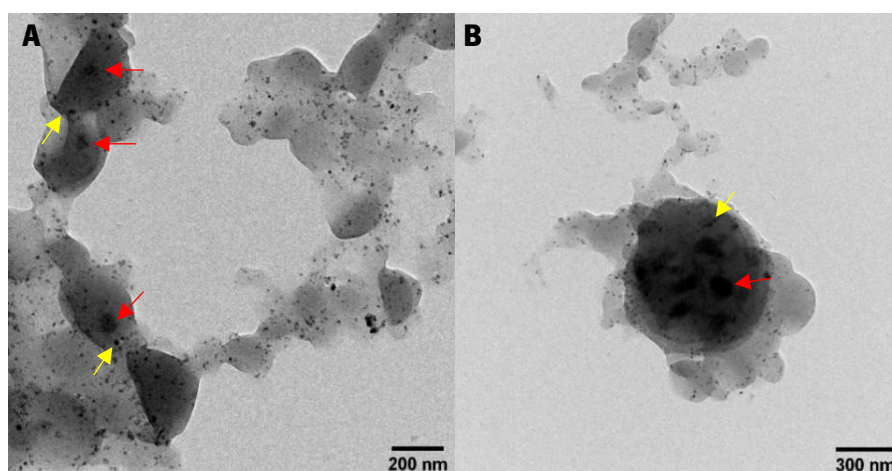
Figure 67 - A,B: TEM micrographs of SLN@Fe₃O₄-MnO-dox, the red arrows point to the MnO@OA NPs and the yellow arrows point to Fe₃O₄@OA NPs.

The optical properties of this particles were studied by fluorescence spectroscopy. Figure 68 shows the fluorescence spectra for the SLNs@Fe$_3$O$_4$-MnO-dox, at an excitation wavelength of 480 nm for the dox and 489 nm for the fluorescent dye, DiO. Since both the excitation wavelengths are very close, their spectra are identical showing three different peaks. The first and less intense peak, at 506 nm corresponds to the fluorescence emission of DiO [217]. The next two peaks, at 557 and 590 nm, correspond to the fluorescence emission of dox, which matches the typical fluorescence spectrum of this

drug [210], [211]. The observed optical behaviour confirms the presence of dox and DiO in the NPs, and the intensity of the peaks is in accordance with the quantities of each compound in the formulation.
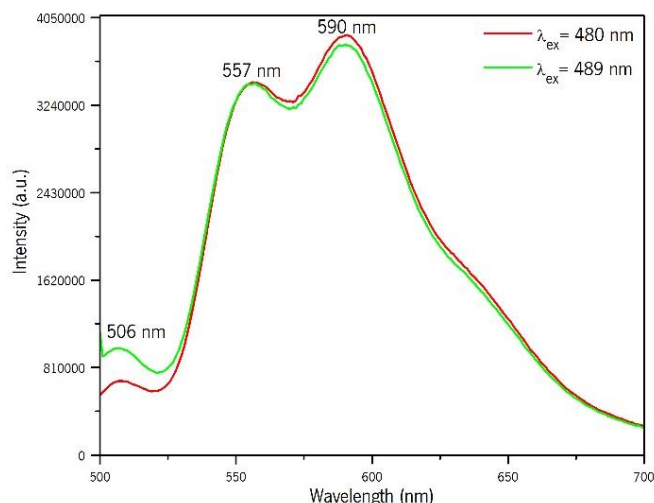
Figure 68 - Fluorescence spectra of SLNs@Fe$_3$O$_4$-MnO-dox at excitation wavelengths of 480 and 489 nm.

The TGA curve for the final SLNs presents two steps of weight loss and it is shown in figure 69. The first and biggest step of weight loss, ①, represents the degradation of the organic components of the SLNs. As stated before, this step of weight loss from 250 to 500 $^{\circ}$C corresponds to the degradation of the surfactant Tween 80, Carnauba wax, OA and doxorubicin [202], [212]–[215]. The second step of weight loss above 750 $^{\circ}$C, ②, may be due to the degradation of magnetite [203]. The inorganic content of SLN@Fe$_3$O$_4$-MnO-dox is approximately 47 %.
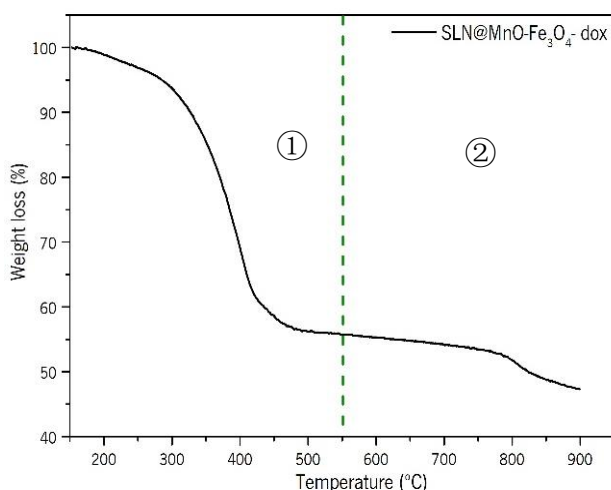
Figure 69 - Thermogravimetric profile of SLNs@Fe$_3$O$_4$-MnO-dox in N$_2$ atmosphere.

The magnetic properties of SLNs containing manganese oxide, magnetite and dox were studied with the SQUID-VSM equipment at 5 and 300K. The field-dependent magnetization curves (figure 70A) and the magnetization curves under 100 Oe (figure 70B) confirm the mixed magnetic behaviour of these particles. As expected, the particles exhibit overimposed paramagnetic and superparamagnetic behaviours, due to the coexistence of paramagnetic MnO@OA and superparamagnetic Fe$_3$O$_4$@OA NPs.

From figure 70A we can observe that the M-H magnetization curve at 5 K shows a ferromagnetic-like behaviour (open magnetic loop) (M_r= 0.08 emu/g; H_c= 0.16 kOe),) that comes from the magnetite NPs, indicating that the nanoparticles are in a magnetically blocked state. At room temperature, these particles are within the superparamagnetic regime, in which the remanent magnetization and the coercivity are closer to 0 (M_r= 0.02 emu/g; H_c= 0.04 kOe). The paramagnetic contribution due to the presence of MnO NPs is appreciated at both 5 and 300K in the M-H curves, being dominant with increasing magnetic field. At 5K, the paramagnetic contribution becomes stronger and dominates the magnetic behaviour [218]. Thus, as in the case of SLNs@MnO the maximum magnetization is approximately ten times greater at 5 K (4 emu/g) than at room temperature (0.4 emu/g), as expected according to the Curie law [218]. The ZFC-FC curves also exhibit a mixed magnetic behaviour. At very low T, the magnetization decay with temperature is indicative of a dominant paramagnetic contribution coming from the paramagnetic MnO NPs, whereas as the temperature increases the typical superparamagnetic behaviour of Fe_3O_4 NPs emerge In fact, the ZFC magnetization curve reveals a blocking temperature at 97 K, above which the SLNs exhibit a superparamagnetic behaviour and below which they are in a blocked magnetic state, in agreeeement with the ferromagnetic-like behaviour observed in the low field region of the field-dependent magnetization curve at 5K (left inset in figure 70). This combined magnetic behaviour can be exploited for biomedical applications, such as MRI diagnostic.
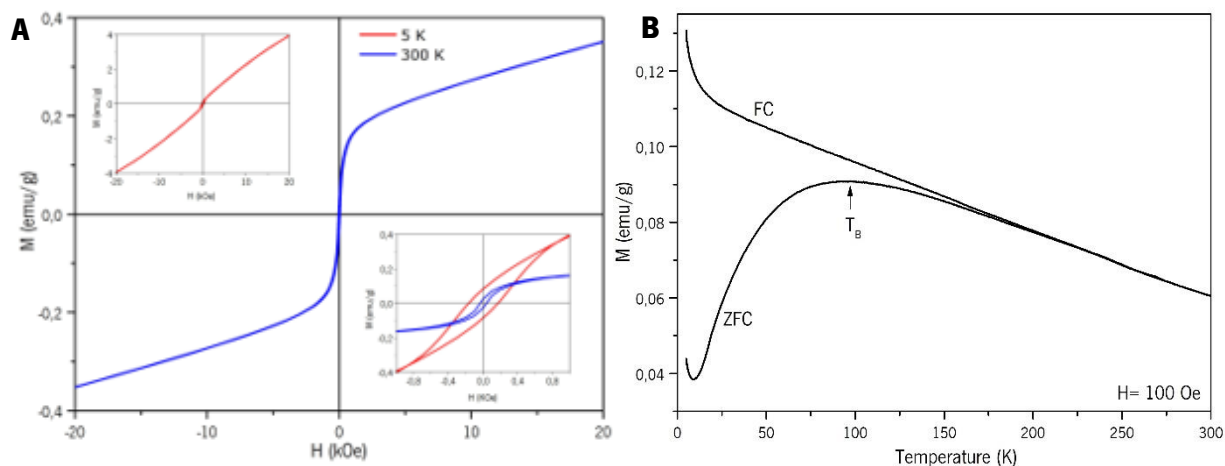
Figure 70 - Field-dependent magnetization curves of SLN@Fe$_3$O$_4$-MnO-dox at 300 K and at 5 K (left inset). The inset on the right shows a close-up of the two curves; B: ZFC-FC magnetization curves at 100 Oe.

The FT-IR spectra of Fe_3O_4@OA, MnO@OA, Tween 80 and Carnauba wax were acquired to ascertain the presence of common functional groups between these components and the SLNs. The spectrum of SLNs@Fe$_3$O$_4$-MnO was also acquired to evaluate if the presence of the dox in the SLNs@Fe$_3$O$_4$-MnO-dox could be observed (figure 71). The band at 560 cm^{-1} in the Fe$_3$O$_4$@OA spectrum corresponds to the symmetric Fe-O bonds stretching in the crystalline lattice of magnetite, and can also be found in the spectrum of the SLNs@Fe$_3$O$_4$-MnO-dox [203]. Around 1407 cm^{-1} a band appears that corresponds to the

CH₃ umbrella mode of the OA, thus the presence of this group is also noticed in the MnO@OA spectrum [203]. In this last spectrum the peak around 425 cm⁻¹ can be assigned to be the Mn-O stretching mode, which does not appear in any other spectra probably due to the small concentration of MnO in the SLNs [219]. Next in the MnO@OA spectrum two peaks at 1457cm⁻¹ and 1710 cm⁻¹ appear and are attributed to the asymmetric (-COO⁻) stretching mode and to the stretching vibration of (C=O) group, respectively. These functional groups are both present in the OA molecule, and the two peaks are also present in the wax and Tween 80 resulting in a more noticeable band in the SLNs [203]. However, the peak at 1457cm⁻¹ can also show a contribution from the bending vibration mode of (-CH₃) groups that are present in the Carnauba wax and OA. The bands at around 2852 and 2922 cm⁻¹ are attributed to the asymmetric and symmetric CH₂ stretch, respectively [203]. These peaks are also present in the wax and Tween 80 with considerable intensity, resulting in their pronounced presence in both SLN formulations. In the Carnauba wax spectrum, the band around 721 cm⁻¹ corresponds to the CH₂ skeleton vibration, that can also be noticed in Tween 80, and consequently in the SLNs spectra [220]. The more distinct peak in the Tween 80 spectra is at 1100 cm⁻¹ and corresponds to the stretching vibration of (C-O) groups, heavily present in Tween 80 chemical structure [220]. Consequently, these groups also appear very pronounced in both SLN formulations. In the Tween 80 and SLNs spectra, there is also a broad peak at around 3500 cm⁻¹ that corresponds to the stretching vibration of (O-H) groups [220]. In the final nanoparticle formulation, containing both MNPs and dox, a new band appears at 1610 cm⁻¹. This band corresponds to the bending vibration mode of (N-H) groups, present in dox [220]. In general, the results obtained by FT-IR are in accordance with what was expected, allowing the visualization of each component of the SLNs, in the final formulation.
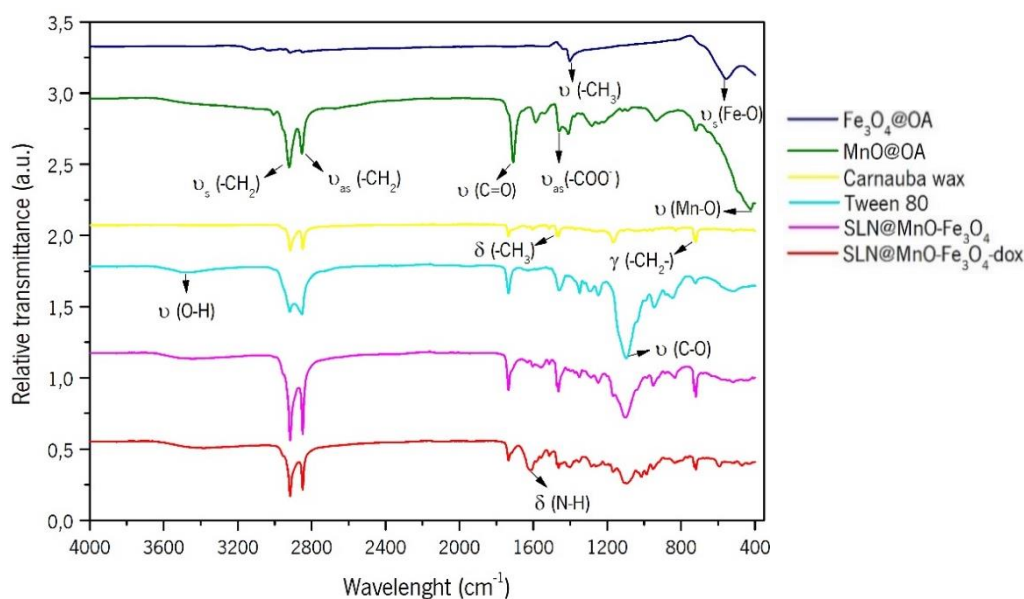
Figure 71 - FT-IR spectra of SLNs@Fe₃O₄-MnO, SLNs@Fe₃O₄-MnO-dox and their magnetic and organic components.

4.3. Functional Characterisation

4.3.1. Magnetic resonance imaging

In order to evaluate the efficiency of the SLNs as contrast agents for MRI applications, both T_1 and T_2 maps for the most relevant particles will be analysed and their relaxivity values discussed. The longitudinal and transverse relaxation times are presented as a function of the concentration of Mn and Fe, respectively. The relaxivity values for all the particles were obtained from the slope of the graphs of relaxation rate ($R_{1/2}=1/T_{1/2}$ s^{-1}) versus ion concentration (mM) (annex 1 and 2).

Figure 72 shows the T_1 and T_2 maps for the samples SLNs@Fe$_3$O$_4$-dox, SLNs@MnO and SLNs@Fe$_3$O$_4$-MnO-dox. The relaxation times can be easily interpreted resorting to the calibration bar present in each map.

First, the T_2 map of the SLNs containing only 5% of iron (SLNs@Fe$_3$O$_4$-dox) was acquired to evaluate the CA efficiency of the encapsulated SPIONs at different concentrations. Figure 72A shows the results obtained for the transverse relaxation weighted map of these particles. The SLNs@Fe$_3$O$_4$-dox achieved a good T_2 enhancement even at low concentrations and start to show some signal saturation around 60-75 µM under the conditions tested. The sample presents shorter relaxation times at higher concentrations, demonstrating its efficiency as a T_2 CA. The r_2 value in water for the SLNs@Fe$_3$O$_4$-dox was 183 mM^{-1} s^{-1}, which is higher than the FDA approved superparamagnetic iron oxide CAs Feridex® (r_2= 93 mM^{-1} s^{-1}) and Resovist® (r_2= 143 mM^{-1} s^{-1}) [221].
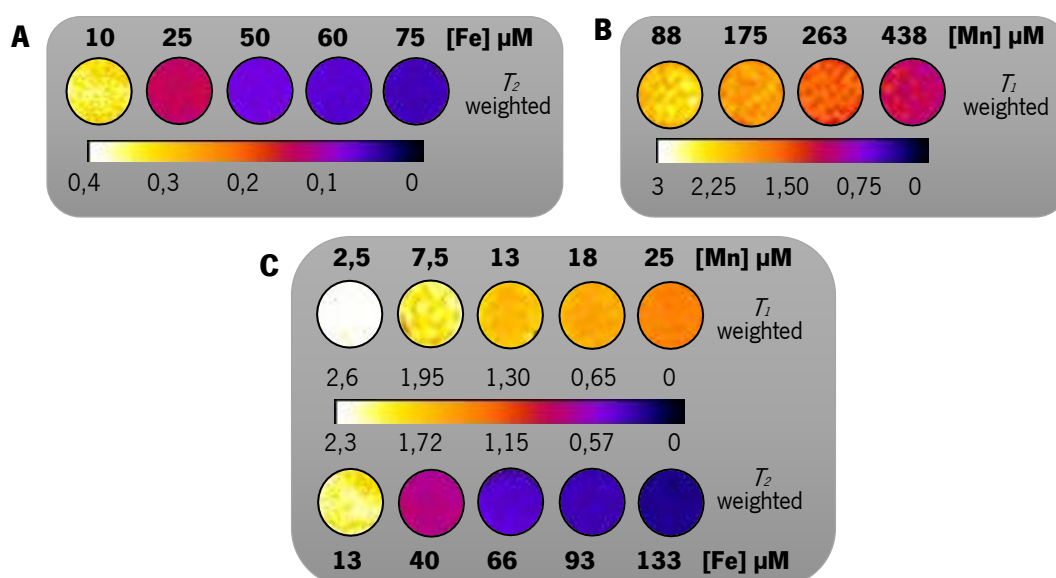
Figure 72 - A: MRI T_2 map of SLNs@Fe$_3$O$_4$-dox; B: MRI T_1 map of SLNs@MnO; C: MRI T_1 and T_2 maps of SLNs@Fe$_3$O$_4$-MnO-dox.

Then, the T_1 map of the SLNs containing manganese oxide (SLNs@MnO) was acquired to evaluate the contrast efficacy of the encapsulated MNPs at different concentrations. Figure 72B shows the

longitudinal relaxation weighted map measured for these particles, at increasingly higher concentrations. The T_1-weighted images show a great difference in contrast between the lower and higher concentrations, demonstrating the good performance of the particles as T_1 contrast enhancers. The r_1 value in water for the sample of SLNs@MnO was 1.25 mM^{-1} s^{-1}, which is close to the manganese-based T_1 CA Teslascan$^{®}$ (r_1= 1.5 mM^{-1} s^{-1}), approved by the FDA [221].

Finally, the T_1 and T_2 maps for the final particles (SLNs@Fe$_3$O$_4$-MnO-dox) were acquired and their relaxivities studied. Since the concentrations used for the SLNs containing only iron showed some saturation at higher concentration values, the range of iron concentrations used for this experiment was lower. Consequently, the range of concentration for Mn was also lower. These SLNs seem to attain a considerably good transverse and longitudinal enhancement even at a lower ranges of concentration, which is a great advantage since less quantity of solution would be needed for administration. The r_1 value obtained for these particles was 13 mM^{-1} s^{-1} which is remarkably higher than Teslascan$^{®}$ and even Magnevist$^{®}$ (r_1= 3.1 mM^{-1} s^{-1}), a gadolinium-based T_1 CA approved by the FDA [221]. The r_2 value obtained was 318 mM^{-1} s^{-1} that is considerably higher than those of Feridex$^{®}$ and Resovist$^{®}$, which is a good indicative of the efficacy of this formulation as CA for MRI. The r_2/r_1 ratio is 24.5 mM^{-1} s^{-1}, an intermediate value that indicates that the formulation in question can accomplish a dual T_1-T_2 reduction. It is to note that the relaxivity values referred for commercial CA solutions are measured at 37 $^{\circ}$C, and as the relaxivity depends on the T (through the diffusion factor), actual values of the compounds presented in here could differ, although the differences are expected to be minimal given the small temperature difference between this temperature and that of the experiment (room temperature). Table 10 shows a summary of the relaxivities and r_2/r_1 ratios obtained for the different SLN formulations.

Table 10 - $r_{1,2}$ and r_2/r_1 ratio for the different SLN formulations.

	r_1 (mM^{-1} s^{-1})	r_2 (mM^{-1} s^{-1})	r_2/r_1 (mM^{-1} s^{-1})
SLNs@Fe$_3$O$_4$-dox	-	183	-
SLNs@MnO	1.3	-	-
SLNs@Fe$_3$O$_4$-MnO-dox	13	318	24.5

Although the physico-chemical characterisation of responsive SLNs, the only formulations with MnO$_2$, did not turn out exactly how it was expected, parallel MRI experiments were still performed to evaluate the responsive ability and CA efficiency of these formulations. The paramagnetic character of Mn ions is determined by the number of unpaired electrons, being that the higher the number of unpaired electrons, higher the paramagnetic character of the Mn ion [63]. Since in MnO$_2$ structure, Mn^{4+} presents only 3 unpaired electrons, it has a weak paramagnetic character. Under certain biologically relevant stimuli,

MnO_2 can be reduced to Mn^{2+} salts with 5 unpaired electrons, becoming highly paramagnetic. This reduction will enhance the T_1 signal in MRI. Hydrogen peroxide (H_2O_2) was used to stimulate the reduction of MnO_2 to Mn^{2+} as represented by the following reaction:

$$Mn^{4+}O_2 + 2\ H_2O_2 \rightarrow Mn^{2+} + 2\ H_2O + 2\ O_2$$
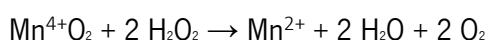
Figure 73 presents the T_1 and T_2 maps for the samples SLNs@MnO_2 and SLNs@Fe_3O_4-MnO_2-dox in water and H_2O_2. The reaction with H_2O_2 should show major differences, particularly in T_1 weighted images. However, to have deeper understanding of the process, differences in T_2 signal were also studied.
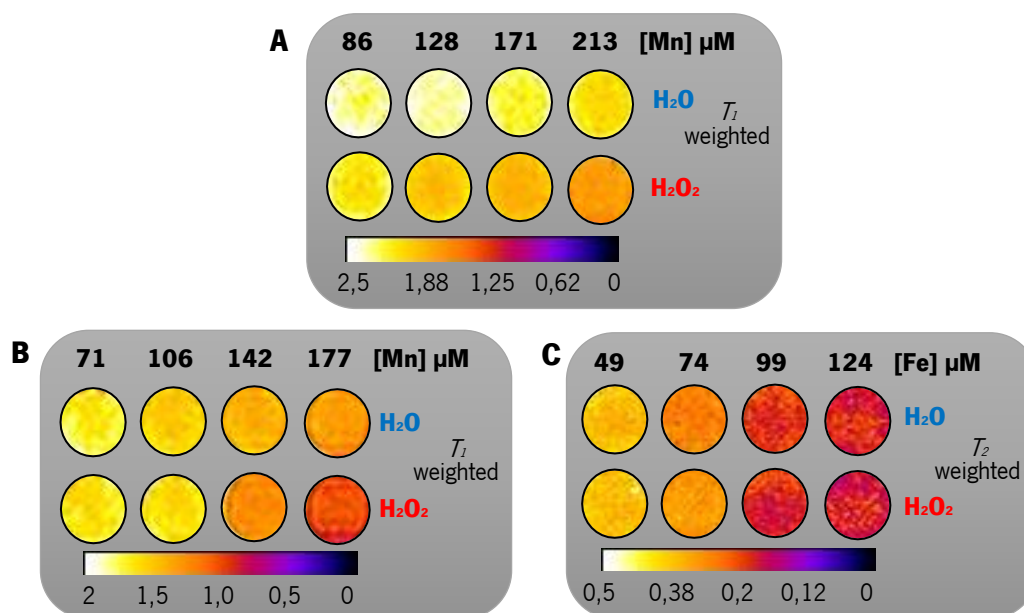
Figure 73 - A: MRI T_1 map of SLNs@MnO_2; B: MRI T_1 map of SLNs@Fe_3O_4-MnO_2-dox.; C: MRI T_2 map of SLNs@Fe_3O_4-MnO_2-dox. All images were acquired in water and in hydrogen peroxide.

As starting point, the T_1 map for the SLNs containing manganese dioxide (SLNs@MnO_2) was acquired to evaluate the contrast efficacy and the O_2 generation ability of the responsive SLNs at different concentrations. Figure 73A presents the longitudinal relaxation weighted map measured for these particles, at increasingly higher Mn concentrations in H_2O and H_2O_2. At higher concentrations the T_1-weighted images present lower relaxation times, suggesting the NPs potential as CAs. Also, the contrast intensity is higher in H_2O_2, which indicates that the SLNs@MnO_2 react with the H_2O_2 producing oxygen. The r_1 value in water for the SLNs@MnO_2 was 0.51 mM^{-1} s^{-1} in H_2O *versus* 0.92 in H_2O_2, confirming the responsive character of the particles. Reported changes in r_1 value upon reduction of MnO_2 to Mn^{2+}, are in the range of 50 to 100 fold. The changes observed in here are much more modest (2 fold) probably due to the encapsulation of MnO_2 NPs inside the wax matrix that prevents its processing by H_2O_2.

Nonetheless, the T_1 and T_2 maps for the SLNs@Fe_3O_4-MnO_2-dox were acquired and are presented in figures 73B and 73C, respectively. The relaxation times are shorter at higher concentrations, for both T_1

and T_2-weighted images, suggesting that these particles have potential as dual contrast agents. The r_1 value in water for the SLNs@Fe$_3$O$_4$-MnO$_2$-dox was 2.2 mM^{-1} s^{-1} in H$_2$O and 5.2 in H$_2$O$_2$, which is a great difference that confirms the responsive character of the NPs. Although no significant responsive behaviour is expected in T_2 signal, the r_2 relaxivities were also studied and showed a slight r_2 difference between H$_2$O (175 mM^{-1} s^{-1}) and H$_2$O$_2$ (207 mM^{-1} s^{-1}). The longitudinal relaxivity values obtained are both higher than the one of Teslascan®, and the transverse relaxivity values are also higher than the ones of Feridex® and Resovist®. The results obtained for these particles are great indicators of the dual CA potential of these SLNs and of their ability to produce oxygen in tumoral environment, however the coefficients of determination obtained for the relaxivity values were not great and more experiments need to be done to validate these results. The r_2/r_1 ratios have intermediate values that confirm the dual CA ability of this sample. Table 11 shows a summary of the relaxivities and r_2/r_1 ratios for the responsive formulations.

Table 11 - $r_{1,2}$ and r_2/r_1 ratio for the responsive SLN formulations in water and hydrogen peroxide.

	r_1 (mM^{-1} s^{-1})		r_2 (mM^{-1} s^{-1})		r_2/r_1 (mM^{-1} s^{-1})	
	H$_2$O	H$_2$O$_2$	H$_2$O	H$_2$O$_2$	H$_2$O	H$_2$O$_2$
SLNs@MnO$_2$	0.5	0.9	-	-	-	-
SLNs@Fe$_3$O$_4$-MnO$_2$-dox	2.2	5.2	175	207	79.5	39.8

4.3.2. Magnetic hyperthermia efficiency

The heating efficiency of SLNs@Fe$_3$O$_4$-MnO-dox NPs was evaluated using the highest field and frequency available (H=20 mT; f= 869 kHz). Figure 74 shows the heating curve for this sample, submitted to the AMF for 1h. Within 500 seconds of AMF induction, the temperature increased more than 3 °C. The SAR value was calculated using the equation (1) present in chapter 1, where the heating capacity of the sample was assumed equal to that of water (4.18 J g^{-1} K^{-1}). The SAR value obtained was of 277 W/g, more than 2 times higher than SAR reported for Feridex® (115 W/g), demonstrating the suitability of SPIONs as heat nanosources and the great heating potential of the final SLN formulation [222].
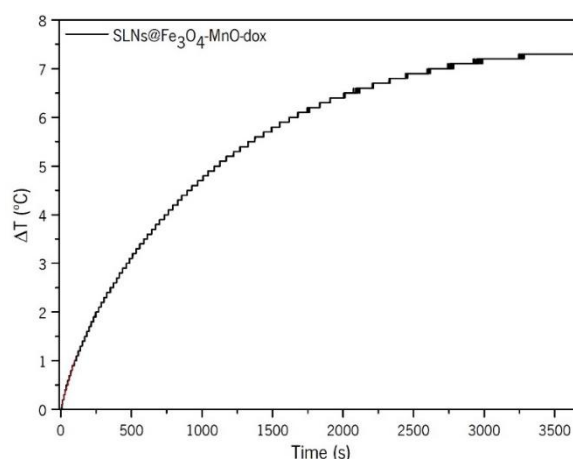
Figure 74 - Heating curve of the final formulation obtained after 1h of AMF induction.

4.3.3. Drug release studies

The presence of MNPs in the SLNs can be profited to add a feature of control over the drug release process. The combination of passive drug release with magnetic hyperthermia will impact the release profile of doxorubicin. Therefore, the passive release of dox from the SLNs@Fe_3O_4-MnO-dox was monitored during 4 hours. Then, the amount of dox released for the same particles under continuous MHT (H=23 mT; f=174.5 kHz) was monitored in the same way.

As shown in figure 75, the release of dox seems to be faster when it is induced by MHT, since the percentage of dox inductively released at the first time point is already higher than in the passive release. From 2 h it is possible to observe significant differences between the two modes of release ($p<0.01$), being that this difference is more significant at 3 h and 4h ($p<0.001$). At 4 h the percentage of drug released for the passive and induced release is about 8 and 14 %, respectively. These results suggest that the application of MHT can efficiently stimulate the release of the encapsulated drug.
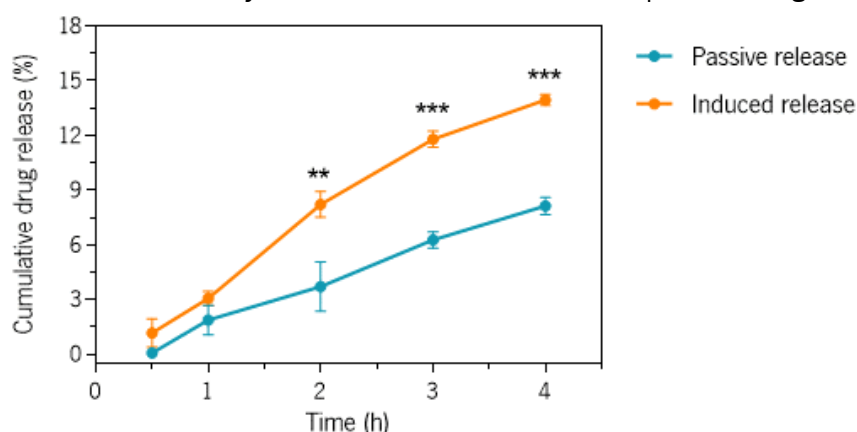
Figure 75 - Comparison of passive versus MHT-induced release of doxorubicin during 4 h. Values represent mean ±SEM. *p<0.05; **p<0.01; ***p<0.001;****p<0.0001.

4.3.4. *In vitro* studies

4.3.4.1. Cytotoxicity studies

The cell viability indicator, AquaBluer™, was used to evaluate the cytotoxicity of different SLN formulations containing only the magnetic core, in a triple negative breast cancer cell line (Hs578T), which is one of the most aggressive cancers. Viable cells metabolize this reagent and turn it from its oxidized form (nonfluorescent, blue) to the reduced form (fluorescent, red). The fluorescence intensity of AquaBluer™ is proportional to number of viable cells in the sample, which allows to quantify the percentage of viable cells. The viability was assessed 48 h after the exposure to the NPs.

The cell viability for different concentrations of each formulation (SLNs@Fe_3O_4, SLNs@MnO, SLNs@MnO_2 and SLNs@Fe_3O_4-MnO) was compared with the non-treated (NT) cells. The treatment with

SLNs@Fe$_3$O$_4$ and SLNs@Fe$_3$O$_4$-MnO did not induce significant cell death in Hs578T cells over metal ion concentrations up to 5 µg/mL. However, at 10 µg/mL the viability decreased significantly for both SLNs@Fe$_3$O$_4$ (p<0.0001) and SLNs@Fe$_3$O$_4$-MnO (p<0.05) (figure 76A and 76B). For the cells treated with SLNs@MnO there was no significant toxicity up to 1.5 µg/mL, whereas from 2 to 10 µg/mL the viability decreased significantly (p<0.05). In addition, this decrease was dose dependent, where 5 and 10 µg/mL showed the highest decrease from the three concentrations (p<0.0001). Furthermore, the difference between the 5 and 10 µg/mL concentrations was still significant (p<0.001), making the 5 µg/mL concentration the less damaging of the two (figure 76C). SLNs@MnO$_2$ showed no significant cell death up to 2 µg/mL, while at 5 and 10 µg/mL of Mn concentration the viability decreased significantly (p<0.0001). Additionally, the difference between these two concentrations was still greatly significant (p<0.0001), making the 10 µg/mL concentration the most toxic of the two (figure 76D).
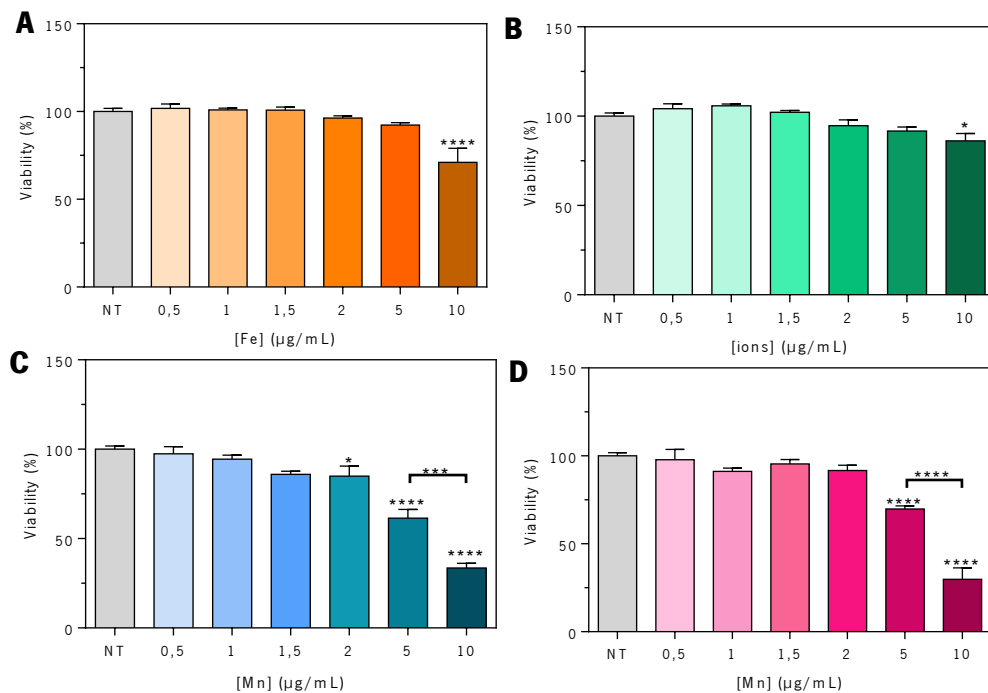
Figure 76 - Cell viability determined 48h after exposure of Hs578T cells to SLNs@Fe$_3$O$_4$ (A), SLNs@Fe$_3$O$_4$-MnO (B), SLNs@MnO (C), SLNs@MnO$_2$ (D) (0.5 to 10 µg/mL). Significance compared to non-treated cells.. Values represent mean ±SEM. *p<0.05; **p<0.01; ***p<0.001;****p<0.0001.

The cytotoxicity between the different SLN formulations at the same concentration was also compared and its presented in figure 77 as a function of the concentration of magnetic content for each formulation. There are no significant differences in cell viability between different SLN formulations, up to 2 µg/mL concentrations. At 5 µg/mL concentrations the viability of cells treated with SLNs containing only manganese was significantly lower (p<0.01) than both SLNs@Fe$_3$O$_4$ and SLNs@Fe$_3$O$_4$-MnO, being that the lower viability was observed for SLNs@MnO$_2$ (p<0.0001). At 10 µg/mL the viability of cells treated with either SLNs@MnO or SLNs@MnO$_2$ was significantly lower than that of cells treated with either

SLNs@Fe₃O₄ or SLNs@Fe₃O₄-MnO (p<0.0001). The viability for the first two samples was about 30 %, and for the latter two ranged from 70 to 85%.
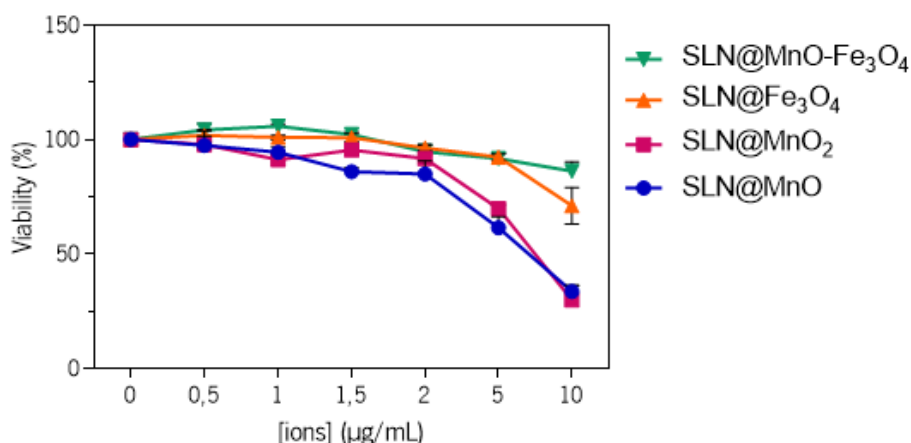
Figure 77 - Cell viability determined 48h after exposure of Hs578T cells to SLNs@Fe₃O₄, SLNs@MnO, SLNs@MnO₂, SLNs@Fe₃O₄-MnO (0.5 to 10 µg/mL). Significance compared between different formulations. Values represent mean ±SEM. *p<0.05; **p<0.01; ***p<0.001;****p<0.0001.

Overall at higher concentrations of ions, SLNs@Fe₃O₄ and SLNs@Fe₃O₄-MnO are less toxic than the SLNs containing only manganese NPs. Mn is clearly more toxic than Fe, which can be because Mn is less shielded, due to a not so efficient encapsulation. These results show that the encapsulated MNPs have no relevant cytotoxicity at concentrations lower than 2 µg/mL of ions, therefore at these concentrations, SLNs are potentially suitable for administration to patients without causing cytotoxicity. To visually asses the morphology of the cells and cell toxicity after incubation with the different SLN formulations, Hs578T cells were treated with the different SLNs at a ion concentration of 1.5 µg/mL and were observed with an optical microscope at 100x magnification. The micrographs are presented in annex 3 and they show no significant morphological changes, except for the SLNs@MnO₂. As before, these can be because of the non-efficient encapsulation of these MNPs.

4.3.4.2. SLNs internalization

In order to evaluate the internalization of SLNs@Fe₃O₄-MnO-dox and consequent doxorubicin release and cellular distribution, Hs570T cells were treated with this formulation for 4h at a concentration of 5 µg/mL regarding dox content (corresponding [Fe]=0,163 µg/mL and [Mn]=0,031 µg/mL – total ion concentration of 0,194 µg/ml).

Figure 78 shows representative confocal microscopy images of non-treated cells and cells treated with SLNs@Fe₃O₄-MnO-dox. The nuclei and the cytoplasm are shown in blue (DAPI) and yellow (α-tubulin), respectively. The fluorescence of the SLNs is seen with green color due to the presence of DiO ($\lambda_{ex/em}$= 489/506 nm) in the formulation. The SLNs are present in the cell cytoplasm, confirming their efficient internalization. Doxorubicin exhibits high fluorescence intensity ($\lambda_{ex/em}$= 480/590 nm), being localised

mainly in the cell nucleus and partially in the cytoplasm. Since the fluorescence of SLNs (green) is only present in the cytoplasm and dox (red) is both present in the cytoplasm (where it co-localizes with SLNs) and nucleus, it is possible to conclude that the SLNs efficiently release dox, which targets the nucleus causing cellular death. Doxorubicin exerts its action through binding to DNA and inhibiting its biosynthesis. As expected, the fluorescence intensity of DAPI is less pronounced in dox-treated cells, confirming the effect of doxorubicin in this main cellular compartment.
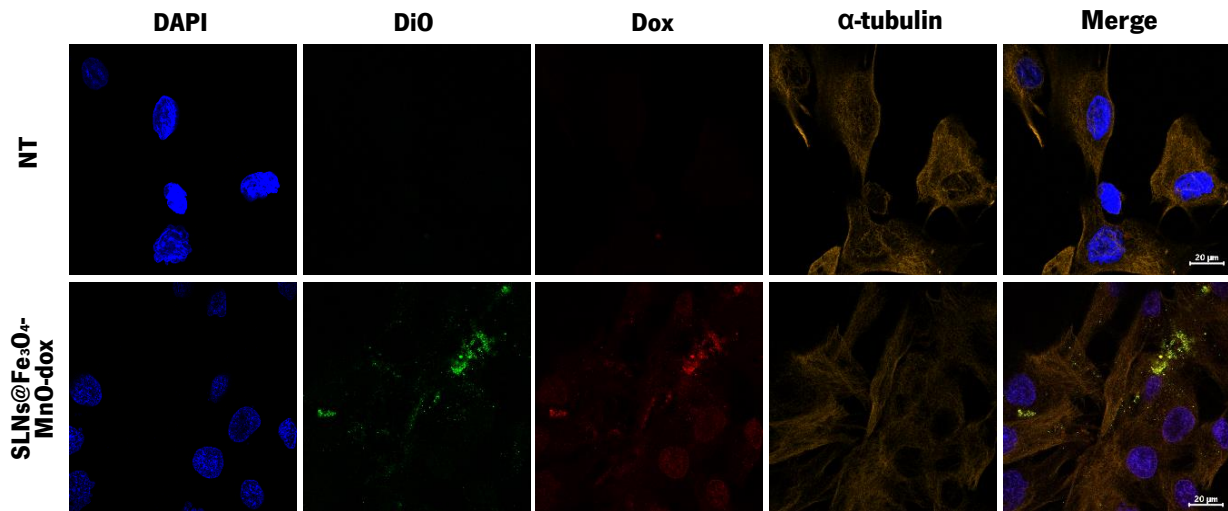
Figure 78 - Confocal micrographs of Hs570T cells non-treated (NT) and after exposure to SLNs@Fe₃O₄-MnO-dox. Scale bar corresponds to 20 μm (see also annex 4).

4.3.4.3. Magnetic hyperthermia

To evaluate the effect of magnetic hyperthermia on malignant triple negative breast cancer cells, a cytotoxicity analysis of free dox, SLNs@dox, SLNs@Fe₃O₄-MnO and SLNs@Fe₃O₄-MnO-dox after exposure to an AMF (H=20 mT; f=224,53 kHz) was performed. Table 12 summarizes the concentrations of every component of each particle and free doxorubicin used to treat the cells in this experiment.

Table 12 - Concentrations of magnetic NPs and dox, used to treat the cells for MHT experiments.

	[dox] (μg/mL)	[Fe] (μg/mL)	[Mn] (μg/mL)
Free dox	2	-	-
SLNs@dox	2	-	-
SLNs@Fe₃O₄-MnO	-	0,044	0,0165
SLNs@Fe₃O₄-MnO-dox	2	0,044	0,0198

First, the differences in viability between free dox and encapsulated dox were evaluated, using doxorubicin at 2 μg/mL. There are no significant differences between the control and cells exposed to MHT in all treatments. There are also no significant differences between the NT cells and cells treated with free doxorubicin. However, NT cells and cells exposed to SLNs@dox present significant differences both in control ($p<0.001$) and in MHT ($p<0.0001$) variables. The differences between free dox treated

cells and SLN@dox treated cells are also significant (p<0.05), indicating that the encapsulation of dox into SLNs enhances its action provoking more cell death for the same concentration of dox.
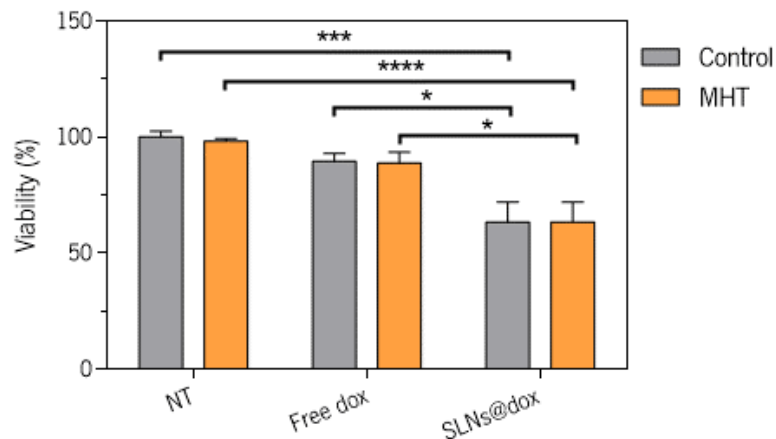
*Figure 79 - Hs578T cells viability after exposure to 2 µg/ml of free doxorubicin dox and SLNs@dox, with (orange) and without MHT (grey). The data represent the mean value $\pm$SEM of triplicate cultures in two different experiments. *p<0.05; **p<0.01; ***p<0.001;****p<0.0001.*

Afterwards, the differences in viability between NT cells and cells treated with the formulations either SLNs@Fe$_3$O$_4$-MnO or SLNs@Fe$_3$O$_4$-MnO ([Fe]=0.044 µg/mL; [Mn]=0.0165 µg/mL) or SLNs@Fe$_3$O$_4$-MnO-dox ([Fe]=0.044 µg/mL; [Mn]=0.0198 µg/mL; [dox]= 2 µg/mL) after exposure to an AMF were evaluated (figure 80). There are no significant differences in viability between NT cells and cells treated with SLNs@Fe$_3$O$_4$-MnO (dox free NPs). Also, for the SLNs@Fe$_3$O$_4$-MnO there are no significant differences between the cells exposed to MHT and the control NT cells. However, mSLNs containing dox induced significant cell death when compared with SLNs containing only magnetic particles, in both control and MHT (p<0.0001). And more importantly, cells treated with SLNs@Fe$_3$O$_4$-MnO-dox showed a significant decrease in viability when exposed to MHT (p<0.01), confirming the potential of these NPs as externally controlled therapeutic agents.
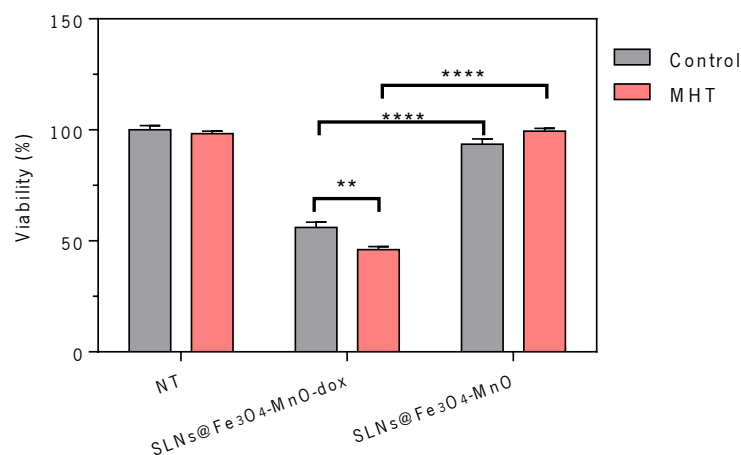
*Figure 80 - Hs578T cells viability after treatment with SLNs@Fe$_3$O$_4$-MnO-dox and SLNs@Fe$_3$O$_4$-MnO, with (pink) and without MHT (grey). The data represent the mean value ±SEM of triplicate cultures in two different experiments. *p<0.05; **p<0.01; ***p<0.001;****p<0.0001.*

As expected, the results confirmed the enhanced therapeutic character of doxorubicin, not only when encapsulated alone, but also when encapsulated together with MNPs while subjected to an AMF.

CHAPTER 5 - CONCLUSIONS AND FUTURE PERSPECTIVES

5.1. Conclusions

In this work, (para)magnetic solid lipid nanocarriers comprising a magnetic core and chemotherapeutic drug, doxorubicin, were developed through a modified melt-emulsification method. This novel and simple method allowed to obtain SLNs with great reproducibility in terms of shape, size and zeta-potential. Superparamagnetic iron oxide nanoparticles and paramagnetic manganese oxide and dioxide nanoparticles were successfully synthetized and encapsulated into the lipidic drug delivery system, yet with limited control over their concentrations. The magnetic lipid vehicle showed to be suitable for the encapsulation of doxorubicin with an encapsulation efficiency above 99%.

A complete physico-chemical characterisation of the SLNs and its constituent magnetic nanoparticles was performed. The magnetic characterisation of the iron oxide and manganese oxide/dioxide NPs confirmed their superparamagnetic and paramagnetic behaviour, respectively. The magnetic properties of the theranostic SLNs revealed their superparamagnetic and paramagnetic mixed behaviour, ideal for the intended biomedical applications.

The presence of (para)magnetic particles in the SLNs formulation enables their use as dual contrast agents in magnetic resonance imaging. SLNs containing both magnetite and manganese oxide produced a dual T_1/T_2 contrast with relaxivities higher than the corresponding commercial CA, which shows their great potential as dual MRI CAs. Both SLNs containing responsive particles of manganese dioxide, exhibited their responsive character when imaged in the presence of hydrogen peroxide. The signal intensity for both T_1 and T_2 was always higher in these conditions. indicating the production of oxygen, useful to combat tumour hypoxia. These particles also presented potential as dual CAs. Nevertheless their physico-chemical properties make them unsuitable for biomedical applications, hence their further development and characterisation was discontinued.

Despite the fact that magnetite nanoparticles were encapsulated into SLNs, the mSLNs showed a great heating efficiency, presenting a value of SAR higher than the one of commercial agents where the MNPs are not encapsulated. This makes the particles suitable for hyperthermia applications, whether for direct therapy through thermal ablation, or as externally controlled triggers to control the drug delivery profile. The drug release by mSLNs was significantly higher when exposed to MHT, proving once again the potential of this NPs as MHT effectors.

Cells treated with mSLNs without drug did not exhibit relevant toxicities, suggesting that the particles are safe for administration in clinically relevant dosages. Also, these lipidic NPs are efficiently internalized by cells, and the release and action of doxorubicin in the nucleus was confirmed. The encapsulation of dox intensified its effect in breast cancer cells. Further studies are required to unveil the mechanism behind this increased efficiency, but studies from the group with mSLNs point towards a faster delivery of doxorubicin to nuclei. The final mSLNs (SLNs@Fe_3O_4-MnO-dox) showed their capability as MHT effectors, since cell viability was significantly decreased when cells treated with these NPs were subjected to a AMF.

Therefore, the main objective of this dissertation was fulfilled, since the presented bionanosystem presents a good performance as a dual MRI contrast agent, externally controlled drug delivery vehicle and MHT effector. The synergistic abilities of the nanocomposite represent a step forward for the treatment of solid malignant tumours, which may realize the dual goals of reduced systemic toxicity and enhanced anti-tumoral efficacy.

5.2.   Future perspectives

The results obtained raise new interesting questions about what could be optimised in the various steps of this work, and also what more could be done to validate the developed system as a new tool in the fight against cancer.

It would be ideal to optimize the synthesis of the SLNs, making it more systematic in a way that the concentration of the encapsulated magnetic content could be accurately reproducible. This could be achieved by using a more stable melting mechanism, since this is a key step on the SLNs synthesis.

Since experiments with encapsulated manganese dioxide NPs corroborated their responsive behaviour, it would be ideal to optimize the physico-chemical properties of the responsive SLNs. A new synthesis method of manganese dioxide NPs should be experimented, so it would be possible to obtain hydrophobic MnO_2 NPs. This way the encapsulation of these particles together with magnetite would be more efficient, and the physico-chemical properties of the obtained SLNs would be more appropriate. It would also be interesting to evaluate the response of MnO_2 NPs to pH changes, since the tumoral environment is an acidic one and MnO_2 has been reported to be very sensitive to pH.

Drug release experiments should be performed at least during 8 h to achieve a more complete drug release profile, and more MHT schemes should be tried to be able to induce significant drug release in

less time. Also, a fitting of the drug release curve with different mathematical models should be done to evaluate the type of release witnessed in each scenario.

Doxorubicin was used as the proof of principle for these experiments, but it would also be interesting to try to encapsulate different chemotherapeutic drugs into the SLNs, even to encapsulate two or more drugs into the same SLNs. Furthermore, studying the MHT effects of the synthetized NPs in different cell lines is very important to validate the formulation.

CHAPTER 6 - BIBLIOGRAPHY

[1]   International Agency for research on Cancer - World Health Organization, "Cancer today," *Global Cancer Observatory*, 2019. [Online]. Available: http://gco.iarc.fr/. [Accessed: 09-Jun-2019].

[2]   A. Grillone *et al.*, "Active Targeting of Sorafenib: Preparation, Characterization, and In Vitro Testing of Drug-Loaded Magnetic Solid Lipid Nanoparticles," *Adv. Healthc. Mater.*, vol. 4, no. 11, pp. 1681–1690, 2015.

[3]   J. Gallo, N. J. Long, and E. O. Aboagye, "Magnetic nanoparticles as contrast agents in the diagnosis and treatment of cancer.," *Chem. Soc. Rev.*, vol. 42, no. 19, pp. 7816–7833, 2013.

[4]   M. Bañobre-López, A. Teijeiro, and J. Rivas, "Magnetic nanoparticle-based hyperthermia for cancer treatment," *Reports Pract. Oncol. Radiother.*, vol. 18, no. 6, pp. 397–400, 2013.

[5]   M. Bañobre-Lopez, L. Garcia-Hevia, F. Cerqueira, F. Rivadulla, and J. Gallo, "Tunable performance of manganese oxide nanostructures as MRI contrast agents," *Chem. - A Eur. J.*, vol. 24, no. 6, p. 1295, 2018.

[6]   J. Gallo, N. Vasimalai, M. T. Fernandez-Arguelles, and M. Bañobre-López, "Green synthesis of multimodal 'OFF-ON' activatable MRI/optical probes," *Dalt. Trans.*, vol. 45, no. 44, pp. 17672–17680, 2016.

[7]   National Cancer Institute, "What Is Cancer?," 2015. [Online]. Available: https://www.cancer.gov/about-cancer/understanding/what-is-cancer. [Accessed: 10-May-2018].

[8]   National Cancer Institute, "Risk Factors for Cancer," 2015. [Online]. Available: https://www.cancer.gov/about-cancer/causes-prevention/risk. [Accessed: 29-Jun-2018].

[9]   PDQ Screening and Prevention Editorial Board, *Cancer Prevention Overview (PDQ®): Patient Version*. 2002.

[10]   International Agency for Research on Cancer - World Health Organization., "Estimated age-standardized incidence rates (World) in 2018, all cancers, both sexes, all ages," *Global Cancer Observatory*, 2018. [Online]. Available: http://gco.iarc.fr/today/online-analysis-map. [Accessed: 31-Jul-2019].

[11]   World Health Organization, "Cancer," Feb-2018. [Online]. Available: http://www.who.int/en/news-room/fact-sheets/detail/cancer. [Accessed: 10-May-2018].

[12]   N. Miranda *et al.*, "Portugal - Doenças Oncológicas em Números." Direção Geral de Saúde, Lisboa, pp. 7–9, 2015.

[13]   P. Boyle and B. Levin, *Mechanisms of carcinogenesis*, vol. 159, no. 2. 2008.

[14]   R. Mehta, "The potential for the use of cell proliferation and oncogene expression as intermediate markers during liver carcinogenesis," *Cancer Lett.*, vol. 93, no. 1, pp. 85–102, 1995.

[15]   C. Sonnenschein and A. Soto, "Carcinogenesis explained within the context of a theory of organisms," *Prog. Biophys. Mol. Biol.*, vol. 122, no. 1, pp. 70–76, Oct. 2016.

[16]   S. Reuter, S. C. Gupta, M. M. Chaturvedi, and B. B. Aggarwal, "Oxidative stress, inflammation, and cancer: How are they linked?," *Free Radic. Biol. Med.*, vol. 49, no. 11, pp. 1603–1616, 2010.

[17] National Cancer Institute, "Treatment for Cancer," 2015. [Online]. Available: https://www.cancer.gov/about-cancer/treatment. [Accessed: 10-May-2018].

[18] C. Rébé and F. Ghiringhelli, "Cytotoxic effects of chemotherapy on cancer and immune cells: how can it be modulated to generate novel therapeutic strategies?," *Futur. Oncol.*, vol. 11, no. 19, pp. 2645–2654, Oct. 2015.

[19] A. Urruticoechea, R. Alemany, J. Balart, A. Villanueva, F. Vinals, and G. Capella, "Recent Advances in Cancer Therapy: An Overview," *Curr. Pharm. Des.*, vol. 16, no. 1, pp. 3–10, Jan. 2010.

[20] S. S. Lucky, K. C. Soo, and Y. Zhang, "Nanoparticles in photodynamic therapy," *Chem. Rev.*, vol. 115, no. 4, pp. 1990–2042, 2015.

[21] J. W. Park, "Liposome-based drug delivery in breast cancer treatment," *Breast Cancer Res.*, vol. 4, no. 3, p. 95, Jun. 2002.

[22] J. Beik *et al.*, "Nanotechnology in hyperthermia cancer therapy: From fundamental principles to advanced applications," *J. Control. Release*, vol. 235, pp. 205–221, 2016.

[23] M. Johannsen, B. Thiesen, P. Wust, and A. Jordan, "Magnetic nanoparticle hyperthermia for prostate cancer," *Int. J. Hyperth.*, vol. 26, no. 8, pp. 790–795, 2010.

[24] M. Johannsen *et al.*, "Clinical hyperthermia of prostate cancer using magnetic nanoparticles: Presentation of a new interstitial technique," *Int. J. Hyperth.*, vol. 21, no. 7, pp. 637–647, 2005.

[25] K. Maier-Hauff *et al.*, "Efficacy and safety of intratumoral thermotherapy using magnetic iron-oxide nanoparticles combined with external beam radiotherapy on patients with recurrent glioblastoma multiforme," *J. Neurooncology*, vol. 103, no. 2, pp. 317–324, 2011.

[26] P. Kaur, M. D. Hurwitz, S. Krishnan, and A. Asea, "Combined hyperthermia and radiotherapy for the treatment of cancer.," *Cancers (Basel).*, vol. 3, no. 4, pp. 3799–823, Sep. 2011.

[27] S. Senapati, A. K. Mahanta, S. Kumar, and P. Maiti, "Controlled drug delivery vehicles for cancer treatment and their performance," *Signal Transduct. Target. Ther.*, vol. 3, no. 1, p. 7, 2018.

[28] E. Drexler, "'There's Plenty of Room at the Bottom' (Richard Feynman, Pasadena, 29 December 1959)," *Metamodern - The Trajectory of Technology*, 2009. [Online]. Available: http://metamodern.com/2009/12/29/theres-plenty-of-room-at-the-bottom"-feynman-1959/. [Accessed: 29-May-2018].

[29] K. E. Drexler and M. Minsky, *Engines Of Creation: The coming Era of Technology*, 1st ed. New York: Anchor books: Doubleday, 1986.

[30] E. Boysen and R. Booker, *Nanotechnology for dummies*, 2nd ed. Indianapolis: Wiley Publishing, Inc., 2005.

[31] G. Gregoriadis, "Drug entrapment in liposomes," *FEBS Lett.*, vol. 36, no. 3, pp. 292–296, 1973.

[32] P. A. Kramer, "Albumin microspheres as vehicles for achieving specificity in drug delivery," *Journal of Pharmaceutical Sciences*, vol. 63, no. 10. pp. 1646–1647, 1974.

[33] V. Wagner, A. Dullaart, A. Bock, and A. Zweck, "The emerging nanomedicine landscape," *Nat. Biotechnol.*, vol. 24, no. 10, pp. 1211–1217, 2006.

[34] Grand View Research, "Controlled Release Drug Delivery Market Analysis Report By Technology (Implants, Transdermal, Microencapsulation, Targeted Delivery), By Release Mechanism, By

Application, And Segment Forecasts, 2018 - 2025," 2018.

[35]   M. Rajabi and S. A. Mousa, "Lipid Nanoparticles and their Application in Nanomedicine," *Curr. Pharm. Biotechnol.*, vol. 17, no. 8, pp. 662–672, May 2016.

[36]   J. R. Kanwar, R. R. Mohan, R. K. Kanwar, K. Roy, and R. Bawa, "Applications of aptamers in nanodelivery systems in cancer, eye and inflammatory diseases.," *Nanomedicine (Lond).*, vol. 5, no. 9, pp. 1435–1445, 2010.

[37]   A. S. Hoffman, "The origins and evolution of 'controlled' drug delivery systems," *J. Control. Release*, vol. 132, no. 3, pp. 153–163, 2008.

[38]   Y. Malam, M. Loizidou, and A. M. Seifalian, "Liposomes and nanoparticles: nanosized vehicles for drug delivery in cancer," *Trends Pharmacol. Sci.*, vol. 30, no. 11, pp. 592–599, Nov. 2009.

[39]   K. ichi Ogawara, K. Un, K. ichi Tanaka, K. Higaki, and T. Kimura, "In vivo anti-tumor effect of PEG liposomal doxorubicin (DOX) in DOX-resistant tumor-bearing mice: Involvement of cytotoxic effect on vascular endothelial cells," *J. Control. Release*, vol. 133, no. 1, pp. 4–10, 2009.

[40]   B. Issa, I. M. Obaidat, B. A. Albiss, and Y. Haik, "Magnetic nanoparticles: Surface effects and properties related to biomedicine applications," *Int. J. Mol. Sci.*, vol. 14, pp. 21266–21305, 2013.

[41]   L. Kafrouni and O. Savadogo, "Recent progress on magnetic nanoparticles for magnetic hyperthermia," *Prog. Biomater.*, vol. 5, no. 3–4, pp. 147–160, 2016.

[42]   L. R. McDowell, *Minerals in animal and human nutrition.*, 2nd ed. Elsevier Science, 2003.

[43]   N. Abbaspour, R. Hurrell, and R. Kelishadi, "Review on iron and its importance for human health," *J. Res. Med. Sci.*, vol. 19, no. 2, pp. 164–174, 2014.

[44]   S. Puig, L. Ramos-Alonso, A. M. Romero, and M. T. Martínez-Pastor, "The elemental role of iron in DNA synthesis and repair," *Metallomics*, vol. 9, no. 11, pp. 1483–1500, 2017.

[45]   WHO, "WHO/CDC expert consultation agrees on best indicators to assess iron deficiency, a major cause of anaemia," *Media center*, 2004. [Online]. Available: https://www.who.int/mediacentre/news/notes/2004/anaemia/en/?fbclid=IwAR0u_RoM1Zuc7 6tkoP2sRd93IjKkW7r42nN3mppcoR9BJrcheP53pTqYQm0. [Accessed: 10-Aug-2019].

[46]   R. Kammari, N. G. Das, and S. K. Das, "Nanoparticulate Systems for Therapeutic and Diagnostic Applications," in *Emerging Nanotechnologies for Diagnostics, Drug Delivery and Medical Devices*, 1st ed., Cambridge: Elsevier, 2017, pp. 105–144.

[47]   A. K. Gupta and M. Gupta, "Synthesis and surface engineering of iron oxide nanoparticles for biomedical applications," *Biomaterials*, vol. 26, no. 18, pp. 3995–4021, Jun. 2005.

[48]   A. H. Lu, E. L. Salabas, and F. Schüth, "Magnetic nanoparticles: Synthesis, protection, functionalization, and application," *Angewandte Chemie - International Edition*, vol. 46, no. 8. pp. 1222–1244, 2007.

[49]   G. F. Goya and M. P. Morales, "Field Dependence of Blocking Temperature in Magnetite Nanoparticles," *J. Metastable Nanocrystalline Mater.*, vol. 20–21, pp. 673–678, 2004.

[50]   A. Jordan *et al.*, "Presentation of a new magnetic field therapy system for the treatment of human solid tumors with magnetic fluid hyperthermia," *J. Magn. Magn. Mater.*, vol. 225, no. 1–2, pp. 118–126, 2001.

[51]   S. M. Moghimi, A. C. Hunter, and J. C. Murray, "Long-circulating and target-specific nanoparticles: theory to practice.," *Pharmacol. Rev.*, vol. 53, no. 2, pp. 283–318, 2001.

[52]   M. Mahmoudi, S. Sant, B. Wang, S. Laurent, and T. Sen, "Superparamagnetic iron oxide nanoparticles (SPIONs): Development, surface modification and applications in chemotherapy," *Adv. Drug Deliv. Rev.*, vol. 63, no. 1–2, pp. 24–46, Jan. 2011.

[53]   K. Wu *et al.*, "Functionalized magnetic iron oxide/alginate core-shell nanoparticles for targeting hyperthermia," *Int. J. Nanomedicine*, vol. 10, p. 3315, May 2015.

[54]   C. Lundquist, C. Loo, I. Meraz, J. Cerda, X. Liu, and R. Serda, "Characterization of Free and Porous Silicon-Encapsulated Superparamagnetic Iron Oxide Nanoparticles as Platforms for the Development of Theranostic Vaccines," *Med. Sci.*, vol. 2, no. 1, pp. 51–69, Feb. 2014.

[55]   R. Wang, Y. Hu, N. Zhao, and F. J. Xu, "Well-Defined Peapod-like Magnetic Nanoparticles and Their Controlled Modification for Effective Imaging Guided Gene Therapy," *ACS Appl. Mater. Interfaces*, vol. 8, no. 18, pp. 11298–11308, 2016.

[56]   J. He, M. Huang, D. Wang, Z. Zhang, and G. Li, "Magnetic separation techniques in sample preparation for biological analysis: A review," *J Pharm Biomed Anal*, vol. 101, pp. 84–101, 2014.

[57]   S. Chandra, S. Nigam, and D. Bahadur, "Combining unique properties of dendrimers and magnetic nanoparticles towards cancer theranostics," *J. Biomed. Nanotechnol.*, vol. 10, no. 1, pp. 32–49, 2014.

[58]   B. S., W. Y., and H. X., "Nanotechnology for enrichment and detection of circulating tumor cells," *Nanomedicine*, vol. 10, no. 12, pp. 1973–1990, 2015.

[59]   J. L. Greger, "Dietary Standards for Manganese: Overlap between Nutritional and Toxicological Studies," *J. Nutr.*, vol. 128, pp. 368S-371S, 1998.

[60]   K. M. Erikson, T. Syversen, J. L. Aschner, and M. Aschner, "Interactions between excessive manganese exposures and dietary iron-deficiency in neurodegeneration," *Environ. Toxicol. Pharmacol.*, vol. 19, no. 3, pp. 415–421, May 2005.

[61]   J. L. Aschner and M. Aschner, "Nutritional aspects of manganese homeostasis," *Mol. Aspects Med.*, vol. 26, pp. 353–362, 2005.

[62]   J. S. Schneider, E. Decamp, A. J. Koser, S. Fritz, T. Syversen, and T. R. Guilarte, "Effects of Chronic Manganese Exposure on Cognitive and Motor Functioning in Non-Human Primates," *Brain Res. Rev.*, vol. 1118, no. 1, pp. 222–231, 2006.

[63]   L. García-Hevia, M. Bañobre-Lopez, and J. Gallo, "Recent progress on manganese-based nanostructures as responsive MRI contrast agents," *Chem. - A Eur. J.*, vol. 24, no. 2, pp. 2–13, 2018.

[64]   G. B. Gerber and A. Le, "Carcinogenicity , mutagenicity and teratogenicity of manganese compounds," *Oncol. Hematol.*, vol. 42, pp. 25–34, 2002.

[65]   A. Takeda, "Manganese action in brain function," *Brain Res. Rev.*, vol. 41, pp. 79–87, 2003.

[66]   J. Huang *et al.*, "HSA coated MnO nanoparticles with prominent MRI contrast for tumor imaging.," *Chem. Commun. (Camb).*, vol. 46, no. 36, pp. 6684–6, Sep. 2010.

[67]   H. Bin Na *et al.*, "Development of a T_1 contrast agent for magnetic resonance imaging using MnO

nanoparticles," *Angew. Chemie - Int. Ed.*, no. 46, pp. 5397–5401, 2007.

[68] J. Gallo, I. S. Alam, I. Lavdas, M. Wylezinska-Arridge, E. O. Aboagye, and N. J. Long, "RGD-targeted MnO nanoparticles as T$_1$ contrast agents for cancer imaging – the effect of PEG length in vivo," *J. Mater. Chem. B*, vol. 2, no. 7, pp. 868–876, Jan. 2014.

[69] C. Tu, E. A. Osborne, and A. Y. Louie, "Synthesis and characterization of a redox- and light-sensitive MRI contrast agent.," *Tetrahedron*, vol. 65, no. 7, p. 1241, Feb. 2009.

[70] M. M. Ali *et al.*, "Synthesis and relaxometric studies of a dendrimer-based pH-responsive MRI contrast agent.," *Chem. - A Eur. J.*, vol. 14, no. 24, pp. 7250–8, Aug. 2008.

[71] W. Zhu *et al.*, "Modulation of Hypoxia in Solid Tumor Microenvironment with MnO$_2$ Nanoparticles to Enhance Photodynamic Therapy," *Adv. Funct. Mater.*, vol. 26, no. 30, pp. 5490–5498, Aug. 2016.

[72] T. Lin, "Oxygen generating manganese dioxide nanoparticles for enhanced photodynamic therapy to bladder cancer by ameliorating hypoxia," *Eur. Urol. Suppl.*, vol. 17, no. 2, p. e664, Mar. 2018.

[73] A. Z. Abbasi *et al.*, "Hybrid manganese dioxide nanoparticles potentiate radiation therapy by modulating tumor hypoxia," *Cancer Res.*, vol. 76, no. 22, pp. 6643–6656, 2016.

[74] P. Prasad *et al.*, "Multifunctional albumin-MnO2nanoparticles modulate solid tumor microenvironment by attenuating hypoxia, acidosis, vascular endothelial growth factor and enhance radiation response," *ACS Nano*, vol. 8, no. 4, pp. 3202–3212, 2014.

[75] A. B. Chin and I. I. Yaacob, "Synthesis and characterization of magnetic iron oxide nanoparticles via w/o microemulsion and Massart's procedure," *J. Mater. Process. Technol.*, vol. 191, no. 1–3, pp. 235–237, 2007.

[76] E. H. Kim, H. S. Lee, B. K. Kwak, and B. K. Kim, "Synthesis of ferrofluid with magnetic nanoparticles by sonochemical method for MRI contrast agent," in *Journal of Magnetism and Magnetic Materials*, 2005, vol. 289, pp. 328–330.

[77] M. Kimata, D. Nakagawa, and M. Hasegawa, "Preparation of monodisperse magnetic particles by hydrolysis of iron alkoxide," *Powder Technol.*, vol. 132, no. 2–3, pp. 112–118, 2003.

[78] S. Basak, D. R. Chen, and P. Biswas, "Electrospray of ionic precursor solutions to synthesize iron oxide nanoparticles: Modified scaling law," *Chem. Eng. Sci.*, vol. 62, no. 4, pp. 1263–1268, 2007.

[79] W. Wu, Q. He, and C. Jiang, "Magnetic iron oxide nanoparticles: synthesis and surface functionalization strategies.," *Nanoscale Res. Lett.*, vol. 3, no. 11, pp. 397–415, Oct. 2008.

[80] S. Laurent *et al.*, "Magnetic Iron Oxide Nanoparticles: Synthesis, Stabilization, Vectorization, Physicochemical Characterizations, and Biological Applications," *Chem. Rev.*, vol. 108, no. 6, pp. 2064–2110, Jun. 2008.

[81] P. Tartaj, M. P. Morales, S. Veintemillas-Verdaguer, T. Gonzalez-Carreño, and C. J. Serna, "Synthesis, Properties and Biomedical Applications of Magnetic Nanoparticles," in *Handbook of magnetic materials*, 191st ed., Amsterdam: Elsevier, 2007, pp. 235–237.

[82] J. Lee, T. Isobe, and M. Senna, "Magnetic properties of ultrafine magnetite particles and their slurries prepared via in-situ precipitation," *Colloids Surfaces Physicochem. Eng. Asp.*, vol. 109, pp. 121–127, Apr. 1996.

[83]   Y. V. Kolenko *et al.*, "High-temperature magnetism as a probe for structural and compositional uniformity in ligand-capped magnetite nanoparticles," *J. Phys. Chem. C*, vol. 118, no. 48, pp. 28322–28329, 2014.

[84]   DRUGBANK,   "Doxorubicin,"   2019.   [Online].   Available: https://www.drugbank.ca/drugs/DB00997. [Accessed: 04-Aug-2019].

[85]   A. C. Alves *et al.*, "Influence of doxorubicin on model cell membrane properties: Insights from in vitro and in silico studies," *Sci. Rep.*, vol. 6343, no. 7, pp. 1–11, 2017.

[86]   A. Kumar, B. Gautam, C. Dubey, and P. K. Tripathi, "A Review: Role of Doxorubicin in Treatment of Cancer," *Int. J. Pharm. Sci. Res.*, vol. 5, no. 10, p. 4105, 2014.

[87]   P. A. J. Speth, Q. G. C. M. van Hoesel, and C. Haanen, "Clinical Pharmacokinetics of Doxorubicin," *Clin. Pharmacokinet.*, vol. 15, no. 1, pp. 15–31, 1988.

[88]   F. Suzuki *et al.*, "Induction of tumor-specific cytotoxicity and apoptosis by doxorubicin," *Anticancer Res.*, vol. 25, no. 2A, pp. 887–894, 2005.

[89]   O. Tacar, P. Sriamornsak, and C. R. Dass, "Doxorubicin: an update on anticancer molecular action, toxicity and novel drug delivery systems," *J. Pharm. Pharmacol.*, vol. 65, no. 2, pp. 157–170, 2013.

[90]   L. Qiu, N. Jing, and Y. Jin, "Preparation and in vitro evaluation of liposomal chloroquine diphosphate loaded by a transmembrane pH-gradient method," *Int. J. Pharm.*, vol. 361, no. 1–2, pp. 56–63, 2008.

[91]   Y. M. Ning *et al.*, "Liposomal doxorubicin in combination with bortezomib for relapsed or refractory multiple myeloma," *Oncology*, vol. 21, no. 12, pp. 1503–1508, 2007.

[92]   V. Sharma, P. Saxena, L. Singh, and P. Singh, "Self emulsifying drug delivery system: a novel approach.," *J. Pharm. Res.*, vol. 5, no. 1, pp. 500–504, 2012.

[93]   M. I. Alam *et al.*, "Strategy for effective brain drug delivery," *Eur. J. Pharm. Sci.*, vol. 40, no. 5, pp. 385–403, 2010.

[94]   T. Bezerra Soares *et al.*, "Lipid nanocarriers loaded with natural compounds: Potential new therapies for age related neurodegenerative diseases?," *Prog. Neurobiol.*, 2018.

[95]   K. Mäder and W. Mehnert, "Solid lipid nanoparticles: production, characterization and applications.," *Adv. Drug Deliv. Rev.*, vol. 47, no. 2–3, pp. 165–96, 2001.

[96]   L. Battaglia *et al.*, "Techniques for the Preparation of Solid Lipid Nano and Microparticles," in *Application of Nanotechnology in Drug Delivery*, 1st ed., InTech, 2014, pp. 51–75.

[97]   M. Üner and G. Yener, "Importance of solid lipid nanoparticles (SLN) in various administration routes and future perspective," *Int. J. Nanomedicine*, vol. 2, no. 3, pp. 289–300, 2007.

[98]   H. L. Wong, R. Bendayan, A. M. Rauth, Y. Li, and X. Y. Wu, "Chemotherapy with anticancer drugs encapsulated in solid lipid nanoparticles," *Adv. Drug Deliv. Rev.*, vol. 59, no. 6, pp. 491–504, 2007.

[99]   S. . Wissing, O. Kayser, and R. . Müller, "Solid lipid nanoparticles for parenteral drug delivery," *Adv. Drug Deliv. Rev.*, vol. 56, no. 9, pp. 1257–1272, 2004.

[100]   J. Pardeike, A. Hommoss, and R. H. Müller, "Lipid nanoparticles (SLN, NLC) in cosmetic and

pharmaceutical dermal products," *International Journal of Pharmaceutics*, vol. 366, no. 1–2. pp. 170–184, 2009.

[101] K. W. Kang *et al.*, "Doxorubicin-loaded solid lipid nanoparticles to overcome multidrug resistance in cancer therapy," *Nanomedicine Nanotechnology, Biol. Med.*, vol. 6, no. 2, pp. 210–213, Apr. 2010.

[102] R. K. Subedi, K. W. Kang, and H. K. Choi, "Preparation and characterization of solid lipid nanoparticles loaded with doxorubicin," *Eur J Pharm Sci*, vol. 37, no. 3–4, pp. 508–513, 2009.

[103] S. V. Mussi, R. C. Silva, M. C. de Oliveira, C. M. Lucci, R. B. de Azevedo, and L. A. M. Ferreira, "New approach to improve encapsulation and antitumor activity of doxorubicin loaded in solid lipid nanoparticles," *Eur. J. Pharm. Sci.*, vol. 48, no. 1–2, pp. 282–290, Jan. 2013.

[104] L. Battaglia *et al.*, "Solid Lipid Nanoparticles for Potential Doxorubicin Delivery in Glioblastoma Treatment: Preliminary In Vitro Studies," *J. Pharm. Sci.*, vol. 103, no. 7, pp. 2157–2165, Jul. 2014.

[105] B. M. Dale, M. A. Brown, and R. C. Semelka, *MRI: Basic Principles and Applications*, 5th ed. Chichester, UK: John Wiley & Sons, Ltd, 2015.

[106] J. Rivas, Y. V. Kolen'ko, and M. Bañobre-López, "Magnetic Nanocolloids," in *Nanocolloids: A Meeting Point for Scientists and Technologists*, M. Sánchez-Domínguez and C. Rodríguez-Abreu, Eds. Elsevier, 2016, pp. 75–120.

[107] H. Yoshioka, P. M. Schlechtweg, and K. Kose, "Magnetic Resonance Imaging," in *Imaging of Arthritis and Metabolic Bone Disease*, B. N. Weissman, Ed. Elsevier, 2009, pp. 34–48.

[108] M. Bañobre-López, Y. Piñeiro, M. A. López-Quintela, and J. Rivas, "Magnetic Nanoparticles for Biomedical Applications," in *Handbook of Nanomaterials Properties*, B. Bhushan, D. Luo, S. R. Schricker, W. Sigmund, and S. Zauscher, Eds. Berlin, Heidelberg: Springer, 2014, pp. 457–493.

[109] H. Bin Na and T. Hyeon, "Nanostructured T1 MRI contrast agents," *J. Mater. Chem.*, vol. 19, no. 35, pp. 6267–6273, 2009.

[110] T. H. Shin *et al.*, "T 1 and T 2 dual-mode MRI contrast agent for enhancing accuracy by engineered nanomaterials," *ACS Nano*, vol. 8, no. 4, pp. 3393–3401, Apr. 2014.

[111] N. A. Keasberry, M. Bañobre-López, C. Wood, G. J. Stasiuk, J. Gallo, and N. J. Long, "Tuning the relaxation rates of dual-mode T_1 / T_2 nanoparticle contrast agents: a study into the ideal system," *Nanoscale*, vol. 7, no. 38, pp. 16119–16128, Sep. 2015.

[112] N. Lee and T. Hyeon, "Designed synthesis of uniformly sized iron oxide nanoparticles for efficient magnetic resonance imaging contrast agents," *Chemical Society Reviews*, vol. 41, no. 7. pp. 2575–2589, 07-Apr-2012.

[113] N. Guldris *et al.*, "Influence of the separation procedure on the properties of magnetic nanoparticles: Gaining in vitro stability and T_1 -T_2 magnetic resonance imaging performance," *J. Colloid Interface Sci.*, vol. 472, pp. 229–236, Jun. 2016.

[114] Y.-K. Peng, S. C. E. Tsang, and P.-T. Chou, "Chemical design of nanoprobes for T 1-weighted magnetic resonance imaging," *Mater. Today*, vol. 19, no. 6, 2015.

[115] A. Neuwelt, N. Sidhu, C. A. A. Hu, G. Mlady, S. C. Eberhardt, and L. O. Sillerud, "Iron-based superparamagnetic nanoparticle contrast agents for MRI of infection and inflammation," *Am. J.*

Roentgenol., vol. 204, no. 3, pp. W302–W313, 2015.

[116] A. H. Kaim *et al.*, "Functional-morphologic MR imaging with ultrasmall superparamagnetic particles of iron oxide in acute and chronic soft-tissue infection: study in rats.," *Radiology*, vol. 227, no. 1, pp. 169–74, Apr. 2003.

[117] J. Chatterjee, Y. Haik, and C.-J. Chen, "Size dependent magnetic properties of iron oxide nanoparticles," *J. Magn. Magn. Mater.*, vol. 257, no. 1, pp. 113–118, 2003.

[118] H. Ersoy and F. J. Rybicki, "Biochemical safety profiles of gadolinium-based extracellular contrast agents and nephrogenic systemic fibrosis," *J. Magn. Reson. Imaging*, vol. 26, no. 5, pp. 1190–1197, Nov. 2007.

[119] H. Fan *et al.*, "A Smart DNAzyme-MnO_2 Nanosystem for Efficient Gene Silencing," *Angew. Chemie Int. Ed.*, vol. 54, no. 16, pp. 4801–4805, Apr. 2015.

[120] S. Lin, H. Cheng, Q. Ouyang, and H. Wei, "Deciphering the quenching mechanism of 2D MnO_2 nanosheets towards Au nanocluster fluorescence to design effective glutathione biosensors," *Anal. Methods*, vol. 8, no. 19, pp. 3935–3940, May 2016.

[121] A. Hervault and N. T. K. Thanh, "Magnetic nanoparticle-based therapeutic agents for thermo-chemotherapy treatment of cancer.," *Nanoscale*, vol. 6, no. 20, pp. 11553–73, Oct. 2014.

[122] O. S. Nielsen, M. Horsman, and J. Overgaard, "A future for hyperthermia in cancer treatment?," *European Journal of Cancer*, vol. 37, no. 13. pp. 1587–1589, 2001.

[123] F. Shubitidze, K. Kekalo, R. Stigliano, and I. Baker, "Magnetic nanoparticles with high specific absorption rate of electromagnetic energy at low field strength for hyperthermia therapy.," *J. Appl. Phys.*, vol. 117, no. 9, p. 094302, Mar. 2015.

[124] K. Maier-Hauff *et al.*, "Intracranial Thermotherapy using Magnetic Nanoparticles Combined with External Beam Radiotherapy: Results of a Feasibility Study on Patients with Glioblastoma Multiforme," *J. Neurooncol.*, vol. 81, no. 1, pp. 53–60, Jan. 2007.

[125] R. Stupp *et al.*, "Radiotherapy plus Concomitant and Adjuvant Temozolomide for Glioblastoma," *N. Engl. J. Med.*, vol. 352, no. 10, pp. 987–996, Mar. 2005.

[126] R. Stupp *et al.*, "Effects of radiotherapy with concomitant and adjuvant temozolomide versus radiotherapy alone on survival in glioblastoma in a randomised phase III study: 5-year analysis of the EORTC-NCIC trial," *Lancet Oncol.*, vol. 10, no. 5, pp. 459–466, May 2009.

[127] Y. Itoh, Y. Yamada, Y. Kazaoka, T. Ishiguchi, and N. Honda, "Combination of chemotherapy and mild hyperthermia enhances the anti-tumor effects of cisplatin and adriamycin in human bladder cancer T24 cells in vitro," *Exp. Ther. Med.*, vol. 1, no. 2, pp. 319–323, 2010.

[128] Malvern Panalytical, "Dynamic Light Scattering: An introduction in 30 minutes." [Online]. Available: https://www.malvernpanalytical.com/en/learn/knowledge-center/technical-notes/TN101104DynamicLightScatteringIntroduction.

[129] D. Arzenšek, R. Podgornik, and D. Kuzman, "Dynamic light scattering and application to proteins in solutions," *Univ. Ljubljana*, no. 4, pp. 1–18, 2010.

[130] Malvern Instruments, "Dynamic light scattering common terms defined," 2011.

[131] M. Kapoor, D. J. Burgess, and S. D. Patil, "Physicochemical characterization techniques for lipid

based delivery systems for siRNA," *Int. J. Pharm.*, vol. 427, no. 1, pp. 35–57, 2012.

[132] M. Gumustas, C. T. Sengel-Turk, A. Gumustas, S. A. Ozkan, and B. Uslu, "Effect of Polymer-Based Nanoparticles on the Assay of Antimicrobial Drug Delivery Systems," in *Multifunctional Systems for Combined Delivery, Biosensing and Diagnostics*, A. M. Grumezescu, Ed. Elsevier, 2017, pp. 67–108.

[133] V. Selvamani, "Stability Studies on Nanomaterials Used in Drugs," in *Micro and Nano Technologies, Characterization and Biology of Nanomaterials for Drug Delivery*, S. S. Mohapatra, S. Ranjan, N. Dasgupta, R. K. Mishra, and S. Thomas, Eds. Elsevier, 2019, pp. 425–444.

[134] E. Joseph and G. Singhvi, "Multifunctional nanocrystals for cancer therapy: a potential nanocarrier," in *Nanomaterials for Drug Delivery and Therapy*, A. M. Grumezescu, Ed. William Andrew Publishing, 2019, pp. 91–116.

[135] The Hebrew University of Jerusalem, "The Zetasizer," *The Interdpartmental Equipment facility*, 2009. [Online]. Available: http://departments.agri.huji.ac.il/zabam/zetasizer.html.

[136] P. J. Worsfold and U. Kingdom, *Spectrophotometry : Overview*, 3rd ed. Elsevier, 2019.

[137] G. P. Holmes-Hampton, W. H. Tong, and T. A. Rouault, "Biochemical and biophysical methods for studying mitochondrial iron metabolism," in *Methods in Enzymology*, 547th ed., A. N. Murphy and D. C. Chan, Eds. Academic Press, 2014, pp. 275–307.

[138] SHIMADZU corporation, "Shimadzu UV-VIS Spectrophotometers."

[139] AAVOS International, "UV-Vis- spectrometry," 2017. [Online]. Available: https://aavos.eu/glossary/uv-vis-spectrometry/. [Accessed: 06-Aug-2019].

[140] A. Jain, C. Blum, and V. Subramaniam, "Fluorescence Lifetime Spectroscopy and Imaging of Visible Fluorescent Proteins," in *Advances in Biomedical Engineering*, P. Verdonck, Ed. Elsevier Science, 2009, pp. 147–176.

[141] R. Kohli, "Methods for Monitoring and Measuring Cleanliness of Surfaces," in *Developments in Surface Contamination and Cleaning: Detection, Characterization, and Analysis of Contaminants*, R. Kohli and K. L. Mittal, Eds. William Andrew Publishing, 2012, pp. 107–178.

[142] C. M. Grasse, "Apparatus," *The Dipole Moment Shift between the Electronic States of Coumarin 102*, 2010. [Online]. Available: http://spa-mxpweb.spa.umn.edu/s10/Projects/S10_Solvations/apparatus.htm. [Accessed: 06-Aug-2019].

[143] P. R. Griffiths, "Introduction to the Theory and Instrumentation for Vibrational Spectroscopy," in *Handbook of Vibrational Spectroscopy*, John Wiley & Sons, Ltd, 2010.

[144] M. R. Derrick, D. Stulik, and J. M. Landry, *Infrared spectroscopy in Conservation Science*. The Getty Conservation Institute, 1999.

[145] M. J. Jafari, "Application of Vibrational Spectroscopy in Organic Electronics," Linköping University, 2017.

[146] M. D. McCluskey, "High-Pressure IR," in *Encyclopedia of Spectroscopy and Spectrometry*, 3rd ed., J. C. Lindon, D. W. Koppenaal, and G. E. Tranter, Eds. Academic Press, 2017, pp. 122–125.

[147] W. D. Perkins, "Fourier transform-infrared spectroscopy: Part l. Instrumentation," *J. Chem. Educ.*, vol. 63, no. 1, pp. A5–A10, 1986.

[148] A. Mezzetti and W. Leibl, "Time-resolved infrared spectroscopy in the study of photosynthetic systems," *Photosynth. Res.*, vol. 131, no. 2, pp. 121–144, 2017.

[149] N. P. Cheremisinoff, "Elemental and Structural Characterization Tests," in *Polymer Characterization*, N. P. Cheremisinoff, Ed. William Andrew Publishing, 1996, pp. 43–81.

[150] Shimadzu, "Shimadzu Inductively Coupled Plasma Atomic Emission Spectroscopy (ICP-AES)," *Environmental solutions*. [Online]. Available: https://www.ssi.shimadzu.com/industry/environmental/icp-aes.html. [Accessed: 30-Aug-2019].

[151] Viaduct, "ICPAES/ICPMS," *Methods*. [Online]. Available: http://www.viaduct-diadrasis.net/methods/6. [Accessed: 30-Aug-2019].

[152] D. R. Smith and M. Nordberg, "General Chemistry, Sampling, Analytical Methods, and Speciation," in *Handbook on the Toxicology of Metals: Fourth Edition*, 4th ed., vol. 1, G. F. Nordberg, B. A. Fowler, and M. Nordberg, Eds. Academic Press, 2015, pp. 15–44.

[153] J. R. Dean, "Inductively Coupled Plasma-Atomic Emission Spectroscopy," in *Practical inductively coupled plasma spectrometry*, D. J. Ando, Ed. John Wiley & Sons, Ltd, 2005, pp. 65–87.

[154] D. S. T. Stephen G. Lipson, Henry Lipson, *Optical Physics*, 3rd ed. Cambridge: Cambridge University Press, 1995.

[155] Nikon corporation, "Inverted Microscope Eclipse TS100." Nikon corporation, Japan, pp. 2–8, 2015.

[156] R. Kasper and B. Huang, "SnapShot: Light microscopy.," *Cell*, vol. 147, no. 5, p. 1198.e1, 2011.

[157] A. Baliyan, H. Imai, and V. Kumar, "Microscopy," in *Data Processing Handbook for Complex Biological Data Sources*, G. Misra, Ed. Academic Press, 2019, pp. 97–117.

[158] C. Zeiss, "Zeiss LSM780, confocal microscope system." Zeiss, Jena, pp. 2–23, 2009.

[159] G. I. Dovbeshko, O. P. Gnatyuk, S. O. Karakhim, T. P. Doroshenko, and V. R. Romanyuk, "Surface enhanced imaging and IR spectroscopy of the biological cells on the nanostructured gold film," *Semicond. Phys. Quantum Electron. Optoelectron.*, vol. 20, no. 2, pp. 159–167, 2017.

[160] C. Y. Tang and Z. Yang, "Transmission Electron Microscopy (TEM)," in *Membrane Characterization*, N. Hilal, A. F. Ismail, T. Matsuura, and D. Oatley-Radcliffe, Eds. Elsevier, 2017, pp. 145–159.

[161] B. J. Inkson, "Scanning electron microscopy (SEM) and transmission electron microscopy (TEM) for materials characterization," in *Materials Characterization Using Nondestructive Evaluation (NDE) Methods*, G. Hübschen, I. Altpeter, R. Tschuncky, and H.-G. Herrmann, Eds. Sheffield: Woodhead Publishing, 2016, pp. 17–42.

[162] D. B. Williams and C. B. Carter, "The Transmission Electron Microscope," in *Transmission Electron Microscopy*, Boston: Springer, 1996, pp. 5–14.

[163] S. J. Pennycook and P. D. Nellist, *Scanning Transmission Electron Microscopy: Imaging and Analysis.*, 1st ed. Springer, 2011.

[164] A. J. Garratt-Reed and D. C. Bell, *Energy Dispersive X-ray Analysis in the Electron Microscope*. CSC Press, 2017.

[165] Mettler Toledo, "TGA/DSC 2." Mettler Toledo, pp. 2–13, 2014.

[166] B. Wunderlich, "Thermal Analysis," in *Encyclopedia of Materials: Science and Technology*, 2nd ed., Pergamon, 2001, pp. 9134–9141.

[167] M. K. Mamun, Abdullah Al Nikousaleh, Mohammad Feldmann, A. Rüppel, V. Sauer, S. Kleinhans, and P. HeimHans, "Lignin Reinforcement in Bioplastic Composites," in *Lignin in Polymer Composites*, O. Faruk and M. Sain, Eds. William Andrew Publishing, 2016, pp. 153–165.

[168] PerkinElmer, "Thermogravimetric Analysis (TGA) A Beginner's Guide." PerkinElmer Inc., Waltham, pp. 4–18, 2015.

[169] S. Foner, "Versatile and sensitive vibrating-sample magnetometer," *Rev. Sci. Instrum.*, vol. 30, no. 7, pp. 548–557, 1959.

[170] A. Niazi, P. Poddar, and A. K. Rastogi, "A precision, low-cost vibrating sample magnetometer," *Curr. Sci.*, vol. 79, no. 1, pp. 99–109, 2000.

[171] K. W. Huang, J. J. Chieh, J. C. Shi, and M. H. Chiang, "Assaying Carcinoembryonic Antigens by Normalized Saturation Magnetization," *Nanoscale Res. Lett.*, vol. 10, no. 1, p. 964, 2015.

[172] P. Marcon and K. Ostanina, "Overview of methods for magnetic susceptibility measurement," in *Progress in Electromagnetics Research Symposium*, 2012, pp. 420–424.

[173] R. L. Fagaly, "Superconducting Quantum Interference Devices (SQUIDs)," in *Wiley Encyclopedia of Electrical and Electronics Engineering*, J. Webster, Ed. Hoboken, NJ, USA: John Wiley & Sons, Inc., 2016, pp. 1–15.

[174] R. L. Fagaly, "Superconducting quantum interference device instruments and applications," in *Review of Scientific Instruments*, 2006, vol. 77.

[175] S. Bedanta, O. Petracic, M. Aderholz, and W. Kleemann, "A sample holder design for high temperature measurements in superconducting quantum interference device magnetometers," *Rev. Sci. Instrum.*, vol. 76, no. 8, pp. 1–3, 2005.

[176] M. Buchner, K. Höfler, B. Henne, V. Ney, and A. Ney, "Tutorial: Basic principles, limits of detection, and pitfalls of highly sensitive SQUID magnetometry for nanomagnetism and spintronics," *J. Appl. Phys.*, vol. 124, no. 16, 2018.

[177] A. A. Bunaciu, E. gabriela Udriştioiu, and H. Y. Aboul-Enein, "X-Ray Diffraction: Instrumentation and Applications," *Crit. Rev. Anal. Chem.*, vol. 45, no. 4, pp. 289–299, 2015.

[178] A. K. Chatterjee, "X-ray Diffraction," in *Handbook of Analytical Techniques in Concrete Science and Technology*, V. S. Ramachandran and J. J. Beaudoin, Eds. William Andrew Publishing, 2001, pp. 275–332.

[179] Universität Stuttgart, "X-Ray Diffractometer," *Intitute of Physical Chemistry - Stubenrauch Group*, 2018. [Online]. Available: http://www.ipc.uni-stuttgart.de/AKStubenrauch/research/equipment/xrd/. [Accessed: 27-Apr-2018].

[180] S. Tadano and B. Giri, "X-ray diffraction as a promising tool to characterize bone nanocomposites," *Sci. Technol. Adv. Mater.*, vol. 12, pp. 1–11, 2011.

[181] J. Lozano-Sánchez, I. Borrás-Linares, A. Sass-Kiss, and A. Segura-Carretero, "Chromatographic Technique: High-Performance Liquid Chromatography (HPLC)," in *Modern Techniques for Food Authentication*, Elsevier, 2018, pp. 459–526.

[182] H. Porto, "HPLC versus UPLC: avaliação de aspetos críticos à transferência e validação de métodos analíticos," University of Coimbra, 2014.

[183] Y. Zeng *et al.*, "Functional probes for cardiovascular molecular imaging," *Quantitative Imaging in Medicine and Surgery*, vol. 8, no. 8. AME Publishing Company, pp. 838–852, 2018.

[184] R. T. and K. Subramaniam, "Laser Cooling System for Magnetic Resonance Imaging Scanner using Normal Controller," *Int. J. Comput. Appl.*, vol. 154, no. 7, pp. 36–40, 2016.

[185] P. Tilakaratna, "How Magnetic Resonance Imaging works explained simply.," *How equiments work*, 2012. [Online]. Available: https://www.howequipmentworks.com/mri_basics/.

[186] J. E. Tanner and E. O. Stejskal, "Restricted self-diffusion of protons in colloidal systems by the pulsed-gradient, spin-echo method," *J. Chem. Phys.*, vol. 49, no. 4, pp. 1768–1777, 1968.

[187] A. D. Elster, "Spin Echo (SE)," *Questions and answers in MRI*, 2019. [Online]. Available: http://mriquestions.com/spin-echo1.html. [Accessed: 19-Aug-2019].

[188] A. D. Elster, "Image contrast," *Questions and answers in MRI*, 2019. [Online]. Available: http://mriquestions.com/image-contrast-trte.html. [Accessed: 19-Aug-2019].

[189] A. D. Elster, "IR: Introduction," *Questions and answers in MRI*, 2019. [Online]. Available: http://mriquestions.com/what-is-ir.html.

[190] M. A. Marino, T. Helbich, P. Baltzer, and K. Pinker-Domenig, "Multiparametric MRI of the breast: A review," *J. Magn. Reson. Imaging*, vol. 47, no. 2, pp. 301–315, Feb. 2018.

[191] M. M. Cruz *et al.*, "Nanoparticles for magnetic hyperthermia," in *Nanostructures for Cancer Therapy*, A. Ficai and A. M. Grumezescu, Eds. Elsevier, 2017, pp. 485–511.

[192] nanoScale Biomagnetics, "DM100 series, Instruments for Magnetic Hyperthermia." nanoScale Biomagnetics, pp. 2–5, 2010.

[193] N. V Jadhav *et al.*, "Synthesis of oleic acid functionalized Fe_3O_4 magnetic nanoparticles and studying their interaction with tumor cells for potential hyperthermia applications.," *Colloids Surf. B. Biointerfaces*, vol. 108, pp. 68–158, Aug. 2013.

[194] R. R. de Almeida *et al.*, "Preliminary Evaluation of Novel Triglyceride-Based Nanocomposites for Biomedical Applications," *J. Braz. Chem. Soc.*, vol. 28, no. 8, pp. 1547–1556, 2017.

[195] H. Chen, J. He, C. Zhang, and H. He, "Self-Assembly of Novel Mesoporous Manganese Oxide Nanostructures and Their Application in Oxidative Decomposition of Formaldehyde," *J. Phys. Chem. C*, vol. 111, no. 49, pp. 18033–18038, Dec. 2007.

[196] Ted Pella Inc., "Substrates, Support Films for Transmission Electron Microscopy Grids," 2019. [Online]. Available: https://www.tedpella.com/Support_Films_html/Support_Films_and_Substrates_Overview.htm. [Accessed: 11-Aug-2019].

[197] MR solutions, "3T MRI," *Preclinical Imaging Systems*, 2019. [Online]. Available: http://www.mrsolutions.com/products/imaging-systems/3t-mri/. [Accessed: 19-Aug-2019].

[198] H. Svilenov and C. Tzachev, "Solid lipid nanoparticles—a promising drug delivery system," in *Nanomedicine*, One Central Press, 2014, pp. 187–213.

[199] L. B. Kiss, J. Söderlund, G. A. Niklasson, and C. G. Granqvist, "New approach to the origin of

lognormal size distributions of nanoparticles," *Nanotechnology*, vol. 10, no. 1, pp. 25–28, Mar. 1999.

[200] D. Chateigner *et al.*, "Crystallography Open Database." [Online]. Available: http://www.crystallography.net/cod/. [Accessed: 18-Sep-2019].

[201] J. R. Correa, D. Canetti, R. Castillo, J. C. Llópiz, and J. Dufour, "Influence of the precipitation pH of magnetite in the oxidation process to maghemite," *Mater. Res. Bull.*, vol. 41, no. 4, pp. 703–713, Apr. 2006.

[202] K. Petcharoen and A. Sirivat, "Synthesis and characterization of magnetite nanoparticles via the chemical co-precipitation method," *Mater. Sci. Eng. B Solid-State Mater. Adv. Technol.*, vol. 177, pp. 421–427, 2012.

[203] K. Yang, H. Peng, Y. Wen, and N. Li, "Re-examination of characteristic FTIR spectrum of secondary layer in bilayer oleic acid-coated Fe_3O_4 nanoparticles," *Appl. Surf. Sci.*, vol. 256, no. 10, pp. 3093–3097, Mar. 2010.

[204] Q. Li, C. W. Kartikowati, S. Horie, T. Ogi, T. Iwaki, and K. Okuyama, "Correlation between particle size/domain structure and magnetic properties of highly crystalline Fe3O4 nanoparticles.," *Sci. Rep.*, vol. 7, no. 1, p. 9894, 2017.

[205] J. M. D. Coey, "Noncollinear spin arrangement in ultrafine ferrimagnetic crystallites," *Phys. Rev. Lett.*, vol. 27, no. 17, pp. 1140–1142, 1971.

[206] Y. Omomo, T. Sasaki, L. Wang, and M. Watanabe, "Redoxable nanosheet crystallites of MnO_2 derived via delamination of a layered manganese oxide," *J. Am. Chem. Soc.*, vol. 125, no. 12, pp. 3568–3575, Mar. 2003.

[207] X. Zhang and W. Yang, "Electrophoretic deposition of a thick film of layered manganese oxide," *Chem. Lett.*, vol. 36, no. 10, pp. 1228–1229, 2007.

[208] M. H. Ghorbani and A. M. Davarpanah, "Synthesis and characterization of MnO_2 nanowires," *Mod. Phys. Lett. B*, vol. 31, no. 02, p. 1750006, Jan. 2017.

[209] R. Grillo *et al.*, "Sub-Micrometer Magnetic Nanocomposites: Insights into the Effect of Magnetic Nanoparticles Interactions on the Optimization of SAR and MRI Performance," *ACS Appl. Mater. Interfaces*, vol. 8, no. 39, pp. 25777–25787, Oct. 2016.

[210] K. K. Karukstis, E. H. Z. Thompson, J. A. Whiles, and R. J. Rosenfeld, "Deciphering the fluorescence signature of daunomycin and doxorubicin," *Biophys. Chem.*, vol. 73, pp. 249–263, 1998.

[211] P. Kumar and S. Agnihotri, "Synthesis of Dox Drug Conjugation and Citric Acid Stabilized Superparamagnetic Iron-Oxide Nanoparticles for Drug Delivery," *Biochem. Physiol. Open Access*, vol. 5, no. 1, pp. 1–6, 2016.

[212] R. S. K. Kishore *et al.*, "Degradation of polysorbates 20 and 80: Studies on thermal autoxidation and hydrolysis," *J. Pharm. Sci.*, vol. 100, no. 2, pp. 721–731, 2011.

[213] J. Milanovic, V. Manojlovic, S. Levic, N. Rajic, V. Nedovic, and B. Bugarski, "Microencapsulation of flavors in carnauba wax," *Sensors*, vol. 10, no. 1, pp. 901–912, Jan. 2010.

[214] J. Luo *et al.*, "Emulsifying ability and cross-linking of silk fibroin microcapsules containing phase change materials," *Sol. Energy Mater. Sol. Cells*, vol. 147, pp. 144–149, Apr. 2016.

[215] A. Lanz-Landázuri, A. Martínez De Ilarduya, M. García-Alvarez, and S. Muñoz-Guerra, "Poly(β,L-malic acid)/Doxorubicin ionic complex: A pH-dependent delivery system," *React. Funct. Polym.*, vol. 81, no. 1, pp. 45–53, 2014.

[216] I. Uddin, P. Poddar, and A. Ahmad, "Extracellular Biosynthesis of Water Dispersible, Protein Capped Mn5O8 Nanoparticles Using the Fungus Fusarium oxysporum and Study of Their Magnetic Behavior," *J. Nanoeng. Nanomanufacturing*, vol. 3, no. 2, pp. 91–97, Mar. 2013.

[217] ThermoFisher, "Fluorescence SpectraViewer - PT," *DiO*. [Online]. Available: https://www.thermofisher.com/pt/en/home/life-science/cell-analysis/labeling-chemistry/fluorescence-spectraviewer.html?SID=srch-svtool&UID=275lip. [Accessed: 29-Sep-2019].

[218] A. Puthirath Balan *et al.*, "Magnetic Properties and Photocatalytic Applications of 2D Sheets of Nonlayered Manganese Telluride by Liquid Exfoliation," *ACS Appl. Nano Mater.*, vol. 1, no. 11, pp. 6427–6434, Nov. 2018.

[219] M. Balamurugan, G. Venkatesan, S. Ramachandran, and S. Saravanan, "Synthesis and Characterization of Manganese Oxide Nanoparticles," in *Synthesis and Fabrication of Nanomaterials*, V. Rajendran, P. Paramasivam, and K. E. Geckeler, Eds. Bloomsbury Publishing India, 2015, pp. 311–314.

[220] E. Pretsch, J. Seibl, and W. Simon, "Tablas combinadas," in *Tablas para la determinación estructural por métodos espectroscópicos*, 3rd ed., A. Fernandéz and R. Álvarez, Eds. Springer - Verlag Ibérica, 1998, pp. 16–50.

[221] M. Rohrer, H. Bauer, J. Mintorovitch, M. Requardt, and H. J. Weinmann, "Comparison of magnetic properties of MRI contrast media solutions at different magnetic field strengths," *Invest. Radiol.*, vol. 40, no. 11, pp. 715–724, Nov. 2005.

[222] V. Nandwana *et al.*, "Theranostic magnetic nanostructures (MNS) for Cancer," *Cancer Treat. Res.*, vol. 166, pp. 51–83, 2015.
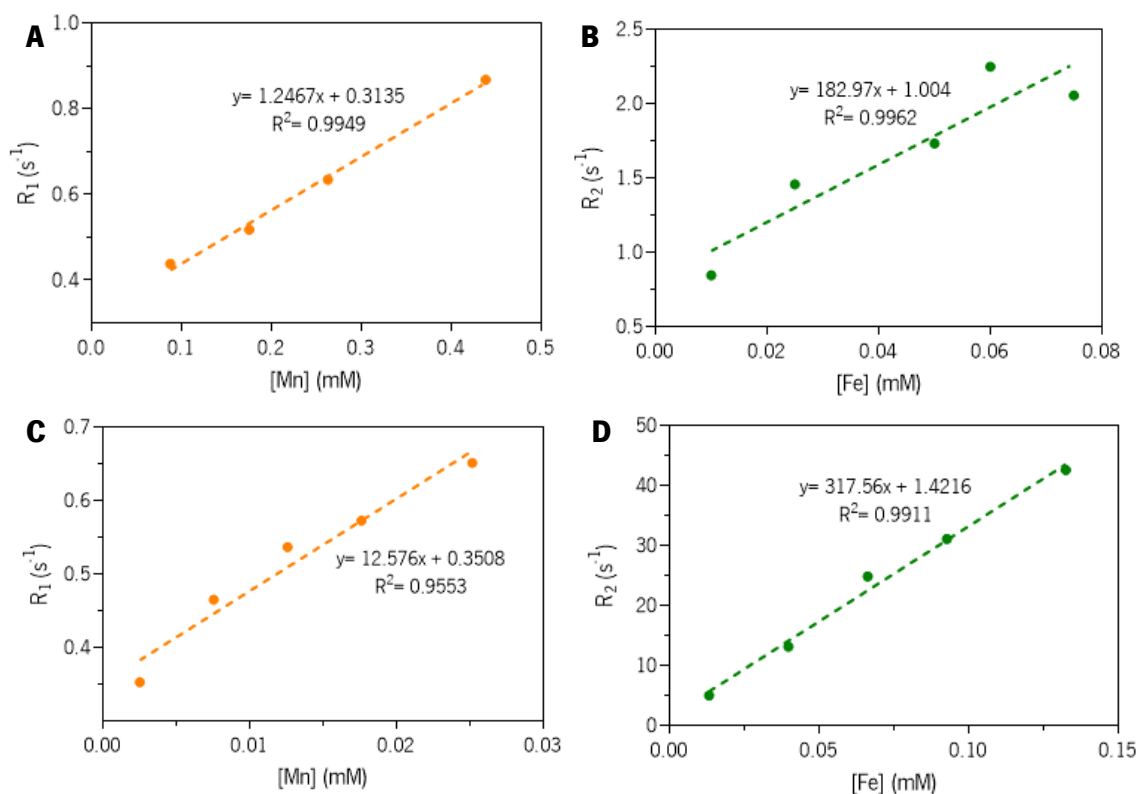
Annex 2 - Relaxation rates versus ion concentrations graphs for SLNs@MnO (A), SLNs@Fe₃O₄ (B) and SLNs@Fe₃O₄-MnO-dox (C) and (D). The slope in each graph represents the longitudinal and transverse relaxations times at a magnetic field of 3T.
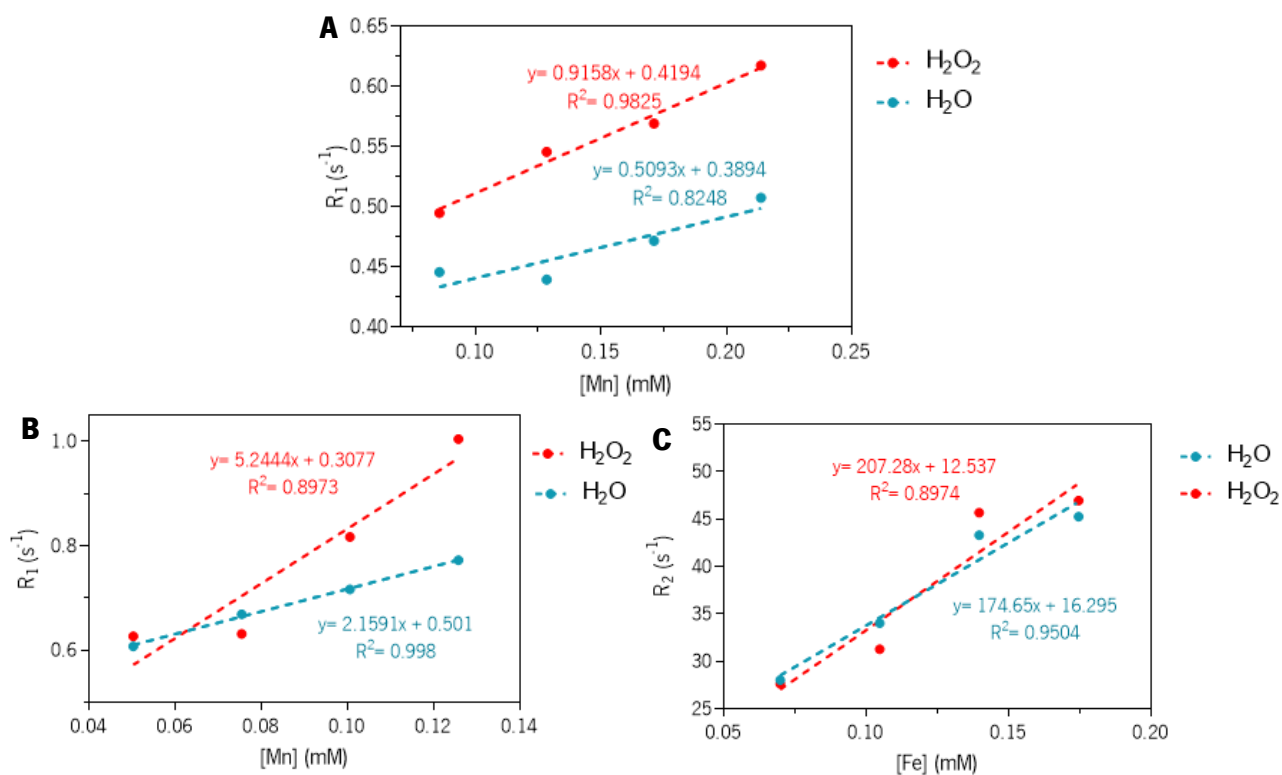
Annex 1 - Relaxation rates versus ion concentrations graphs for SLNs@MnO₃ (A) and SLNs@Fe₃O₄-MnO₃-dox (B) and (C), in water and hydrogen peroxide. The slopes in each graph represents the longitudinal and transverse relaxations times at a magnetic field of 3T.
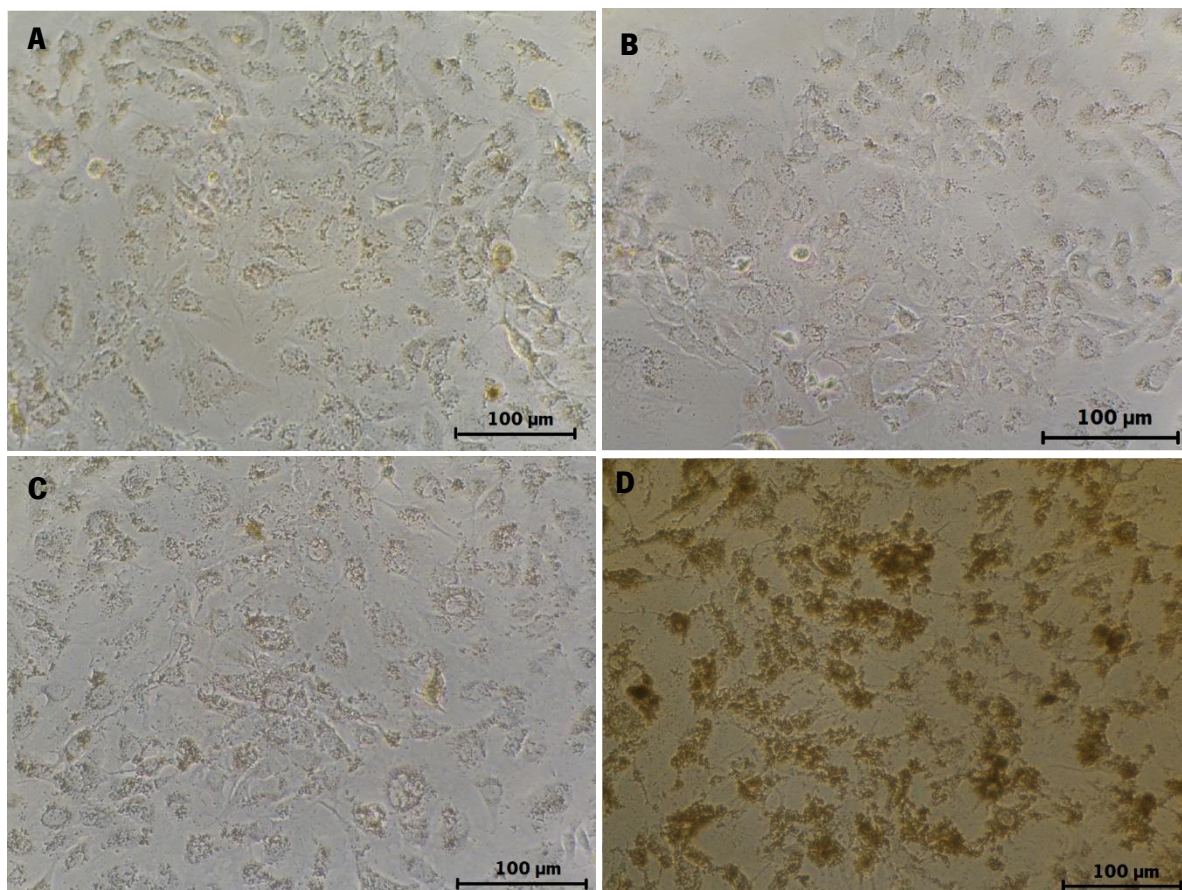
Annex 3 - Micrographs representative of cell viability of Hs578T cells treated with SLNs@Fe₃O₄ (A), SLNs@Fe₃O₄-MnO (B), SLNs@MnO (C), SLNs@MnO₂ (D) at a ion concentration of 1.5 µg/mL (100x magnification).
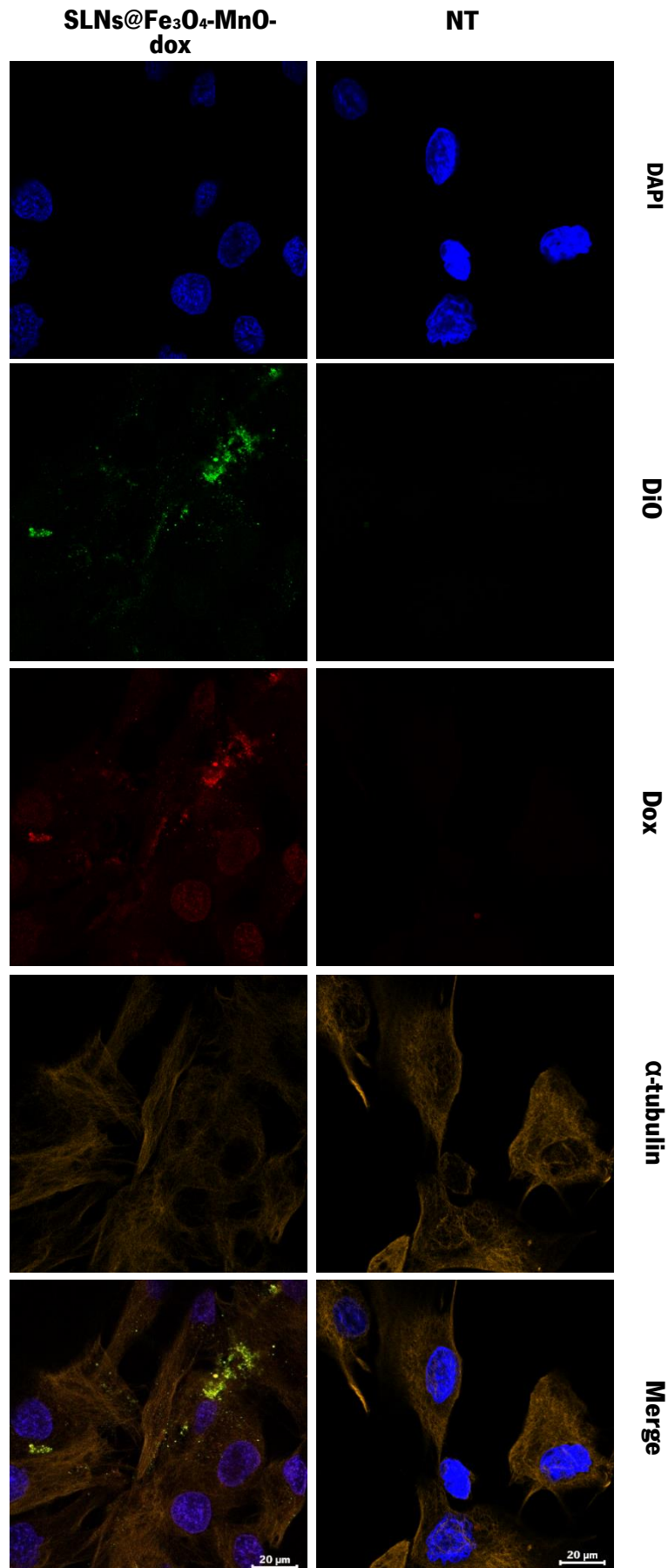
Annex 4 - Confocal micrographs of Hs570T cells non-treated (NT) and after exposure to SLNs@Fe3O4-MnO-dox. Scale bar corresponds to 20 μm.